A.van den Berg

Assessing piglet model suitability for inflicted head injury by shaking trauma in infants

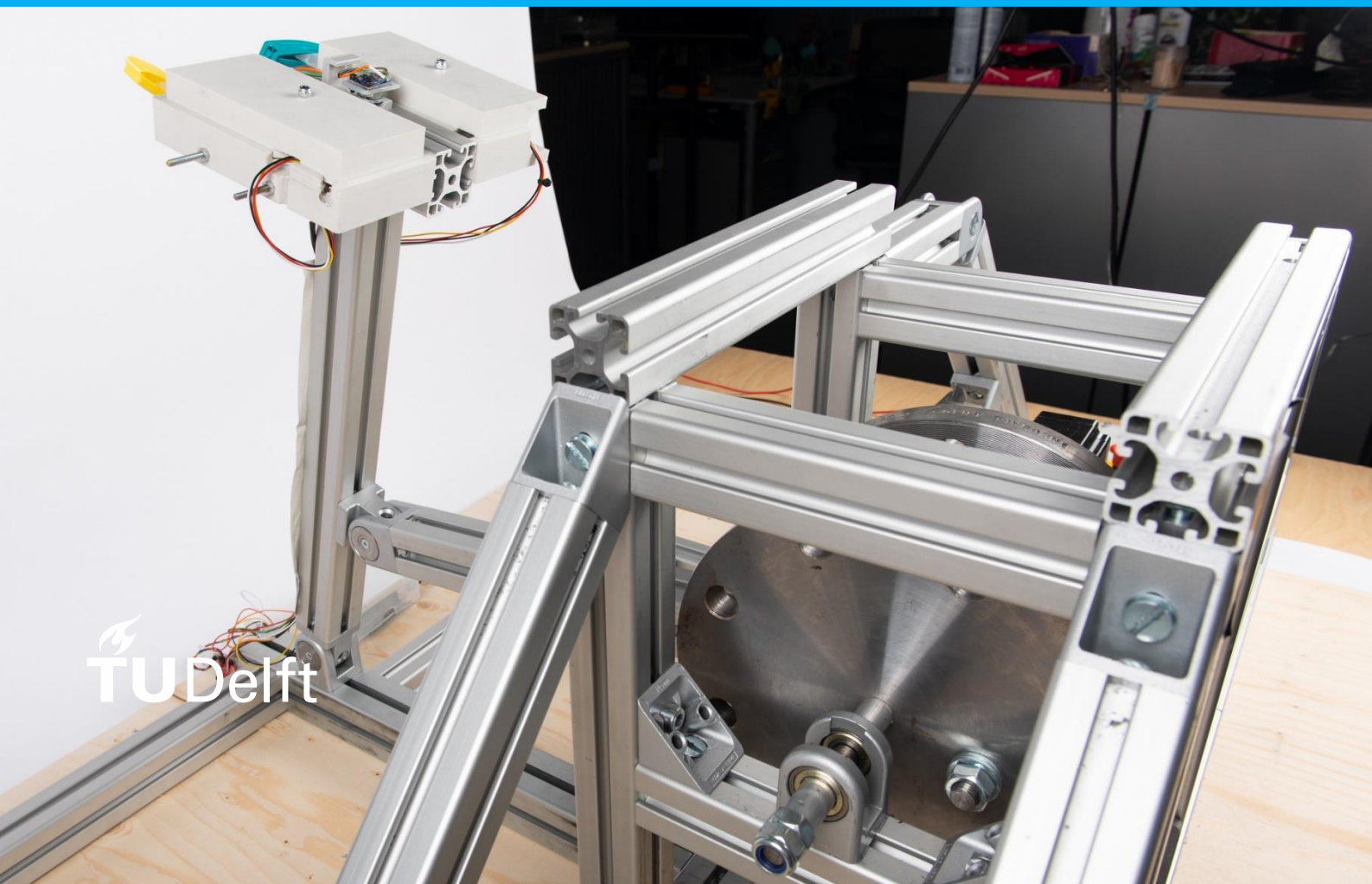

Assessing piglet model suitability for inflicted head injury by shaking trauma in infants

The difference in pressure variations inside the eye between pig and infant eyes of an infant during violent shaking

By

A. Van den Berg

in partial fulfilment of the requirements for the degree of

Master of Science
in Biomedical Engineering

at the Delft University of Technology,
to be defended publicly on Thursday August 29, 2024

Thesis committee:	Dr. Ir. A.J. Loeve,	TU Delft, chair, supervisor
	Ir. K. Hutchinson MSc,	TU Delft, supervisor
	Prof. Dr. J. Dankelman,	TU Delft

TU Delft

Preface

In front of you is the master's thesis "Assessing piglet-model suitability, for inflicted head injury by shaking trauma in infants", which I have written with great pleasure. During my bachelor's study in Movement Sciences, I noticed that I was interested in the mechanical aspects of movement. Besides this interest, I thought it would be challenging to pursue a master's degree at TU Delft and this caught my attention. To orient myself within TU Delft, I completed a minor in Biomedical Engineering during my bachelor's studies. During this minor, I discovered that this area of engineering greatly appealed to me, which led me to start the master's program in Biomedical Engineering. This turned out to be a good choice. I enjoyed studying over the past few years and I have learned a lot.

During my internship, in which I collaborated on the development of a nail clipper for forensic research in partnership with the Forensic Institute and the national police, my interest in forensic research was sparked. In these studies, you truly feel like you are contributing to society. In consultation with Arjo Loeve, I eventually settled on the topic for my graduation project. The combination of a forensic aspect and movement was the perfect mix for me, given my bachelor in Movement Sciences.

During my internship and my master thesis, I gained a lot of experience, particularly in the field of design. I used programs such as SolidWorks and Arduino for the first time, which made it a significant challenge, especially at the beginning. I would like to thank my supervisors, Dr. Ir. Arjo Loeve and Ir. Kim Hutchinson, for their excellent guidance and support during the process. I deliberately chose both supervisors because I knew they would challenge me to take my research to a higher level. This has maximized my learning opportunities, for which I am very grateful. I would also like to thank all my fellow students, as I could not have completed this study without them.

Finally, I want to thank my family and friends for their support throughout my years of study. I would especially like to thank my fiancé, Pieter Bachaus. Over the past few years, he has greatly supported and encouraged me to successfully complete my master degree.

I hope you enjoy reading it.

Anneloes van den Berg
Delft, August 2024

Contents

Abstract

This study investigates eye pressure variations within the eye between pigs and humans during an IHI-ST event, focusing on anatomical differences in orbital cavities. Eight anatomical differences were identified through literature research, with two deemed most relevant for pressure variation. Four orbits were created to combine eye orientation and orbital closure. Subsequently, handcrafted eye models were tested using a shaking simulator.

This research has led to the creation of a test setup capable of simulating the shaking motion of an IHI-ST event. Initial steps have been taken to investigate pressure buildup in the eye during these movements, yielding preliminary results on the effects of anatomical differences between the eyes of pigs and humans.

The results indicate that closed orbits exhibit higher relative eye pressure compared to open orbits. Additionally, higher eye pressures were observed in humans than in pig, in line with the expectations. This indicates that due to the anatomical differences between the eyes of pigs and humans, higher eye pressure occurs during shaking in humans compared to pigs. The results of this study thus suggest a cautious conclusion that pigs may not be suitable for research material in the context of IHI-ST. The study's limitations include the use of simplified eye models, which affect external validity, and the lack of factors such as neck stiffness.

Overall, this research lays the groundwork for future studies on intraocular pressure during shaking events, emphasizing the need for improved experimental designs and more accurate models to enhance understanding and clinical outcomes related to retinal haemorrhage.

1. Introduction

1.1. What is inflicted head injury by shaking trauma?

Inflicted head injury by shaking trauma (IHI-ST) in infants is a common type of neuro-trauma in children under 2 years of age with an incidence rate of 14-40 cases per 100.000 children [1-5]. As a consequence of the incident, 15-23% of these children die, which indicates the importance of research on this topic [2]. Symptoms of IHI-ST are difficult to define but are mostly characterised as a triad consisting of subdural haemorrhage, retinal haemorrhage (RH) and hypoxemic encephalopathy [6]. The possible mechanisms of subdural haemorrhage and hypoxemic encephalopathy are clear. However, the possible mechanisms of RH in IHI-ST are currently unknown and unproved [6]. Case studies have been conducted to investigate the prevalence of RH and the locations of the bleedings. RH appears in IHI-ST in different shapes and types. It can appear in the shape of a dot, a flame or a combination of both [10]. Furthermore, RH in IHI-ST may be bilateral but unilateral ones also exists. Most of the time it appears multi-layered and can cause vision loss [11, 12]. RH is presented in 65-90% of all these case studies [7]. Togioka et al. [8] used 66 articles to identify findings and patterns of RH by IHI-ST in infants. RHs were found in 62.5-100% of these 66 articles and mostly were flame-shaped. In most of the articles they found, RH were found in the posterior pole of the retina.

Levin et al. [9] used 80 retina images from suspected cases of IHI-ST but also some from accidental injury or nontraumatic retinal cases. The researchers Levin et al. [9] divided the eye into four distinct areas, examining the frequency of RH occurrence in each area (see figure 1). The first area (A), is the peripapillary circle centred on the middle of optic nerve with a diameter three times that of the optic disc. Area two (B), is the posterior pole circle, the centre of which lies on a line bisecting the retinal arcades and located on the fovea. Area three (C), is the midperipheral circle, the edges of which run through the vortex veins (yellow dots). Area four (D), consists of the peripheral retina beyond region C. The researchers found significantly more haemorrhages in Area A and B than in C and D (see Figure 1). This indicates that RH occurs more frequently in the vicinity of the optic nerve and the posterior pole. The optic nerve contains the central retinal artery and the central retinal vein, which, when eye pressure increases, can potentially lead to RH because the veins can be damaged as a result of the eye pressure increase. [11, 12].

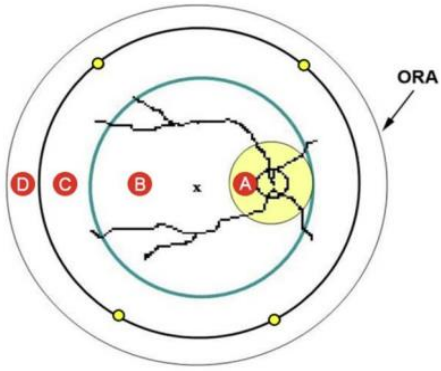

Figure 1: Four areas where RH was found in eighty retinal images. Area A: the peripapillary circle centred on the middle of optic nerve with a diameter three times that of the optic disc. Area B: is the posterior pole circle, the centre of which lies on a line bisecting the retinal arcades and located on the fovea. Area C: the midperipheral circle. Area D: the peripheral retina [9].

About 30 years ago, studies already examined the cause of RH in IHI-ST [13, 14]. Duhaime et al. [13] suspected that RH is caused by increased intracranial pressure and Greenwald et al. [14] suspected that the acceleration-deceleration movements of the head of an infant during violent shaking could result traction in the layers of the retina. Greenwald et al. [14] also discussed that there is a possibility that the pressure on sinus cavernous can also be the cause of bleeding in the eye. The central retinal vein (which exits from the retina) is connected to the sinus cavernous [14]. The direction of the blood flow is dependent on the venous pressure. So, if the venous pressure is high in the sigmoid sinus and thus in the petrosal sinus, the venous pressure of the central retinal veins will also higher, increasing the risk of RH.

Because of the lack of consensus on the cause of RH in IHI-ST in case studies, more types of studies were done to examine the cause of RH in IHI-ST. These studies can be put into four categories: Finite Element Models (FEMs), doll models, clinical models, and animal models. In these four categories, RH in IHI-ST was specifically examined by the researchers of these studies because there are many other causes of RH besides shaking trauma, such as disorders -and abnormalities, falls and birth trauma [15-19]. RH in these non-shaking cases are usually less numerous and less extensive compared to RH in IHI-ST [15, 16].

A systematic review by Van den Berg et al. [38] (not published) was done to investigate the possible mechanical causes of RH in IHI-ST in infants. This showed that there are four possible causes: Orbital shaking injury, occurs when forward inertia from a shaking event causes the eyeball to become displaced from the eye socket, accompanied by a buildup of pressure within the eye, as shown in Figure 2. Pressure on the optic nerve, occurs when shaking events increase intraocular pressure due to fluid buildup or swelling. This increased pressure exerts mechanical stress on the optic nerve, compressing the blood vessels that supply the nerve and spread into the retina. Shearing forces, which means that shearing forces between the layers and the vascularity of the retina cause RH, can disrupt the connections between the

different layers of the retina, leading to tears and damage to the blood vessels. Pressure on the sinus cavernous, which is connected to the central retinal vein and located next to the internal carotid arteries, can lead to RH by increasing venous pressure on the retinal vessels (see Figure 2) [14].

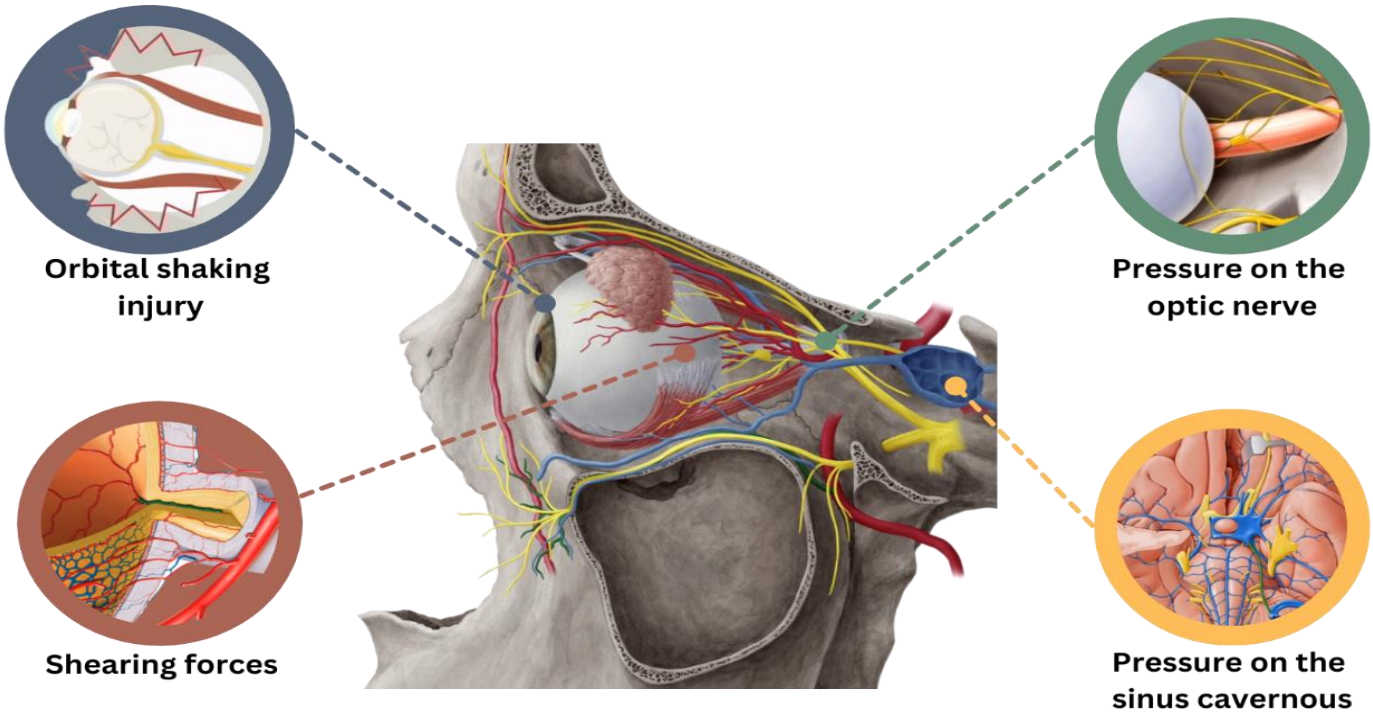

Figure 2: Summary of the four hypotheses found in literature. Orbital shaking injury, Pressure on the optic nerve, Shearing forces, and pressure on the sinus cavernous by the literature study of van den Berg et al. [38] and the study of Greenwald et al. [14]. These hypotheses may indicate the possible mechanical causes of RH in IHI-ST in infants. In blue, the hypotheses about orbital shaking injury are shown. Due to shaking, the forward inertia can be too big which results in a situation where the eyeball is pushed out of the eye socket as can been seen in the figure. In red, the hypotheses about shearing forces are shown. In the figure, the layers and the vascularity of the retina can be seen. In green, the optic nerve is shown. Some studies hypothesize that RH arises from pressure on the optic nerve. In Yellow, the pressure on the cavernous is shown. In the part of the orbital, the sinus cavernous is connected with the central retinal vein and is located next to the internal carotid arterials.

In some animal model studies, pig eyes were selected as a model for infant eyes due to the similarities in anatomy. Of these animal model studies, only three pig model studies have been conducted since 2010 [17-19]. One of the three pig model studies found RH in a small number of animals [17]. However, this study did not test in a representative situation because the load applied in this study was a single, high-velocity rotation of 117-266 rad/s and accelerations of 30.6–101 krad/s ^{2} of the head which is not comparable to the repetitive motion that occurs during shaking. In an IHI-ST event, a much lower velocity, repetitive and back-and-forth motion occurs [17]. However, the findings of the more recent study by Coats et al. [18], which rotated the head repetitive back-and-forth during the experiment with a frequency of 2.19 ± 0.49 Hz, angular velocity of 47.12 ± 13.96 rad/sec and accelerations of 1512 ± 1295 rad/sec 2, did not support the previous research of Coats et al. [17] because they did not find any RH. These results are in agreement with Umstead et al. [19], who also found no RH. However, Umstead et al [19] only used the pig model as a validation to compare with their computer model. They performed an experiment by using animal models to ascertain the required pressure that is needed to provoke RH.

1.2. Relevance and Purpose

It is noteworthy that in case studies of infants with suspected IHI-ST events, RH was found. While in most pig model studies no RH was found. It is suspected that the cause of this might be the anatomical differences between the pig and human eye. For example, the blood vessels in the pig eye are quite different from those in the human eye. The human eye contains a central retinal artery and vein, which are situated in the optic nerve and terminate at the optic disc. In contrast, pigs lack a central retinal artery and vein. Instead, the retinal vessels in pigs are branches of the chorioretinal arteries and veins, which enter at the optic disc [29]. Furthermore, the pig has an open orbit, and the human has a closed orbit [17]. These anatomical differences between the eye and surrounding structures of the pig and infant may affect the observed injury patterns in the studies.

If we understand the implications of these anatomical differences between the human and pig orbit on RH, conclusions may be drawn regarding RH in the context of IHI-ST events involving pigs in future studies. Furthermore, these types of studies may lead to validated infant models and facilitate the validation of experiments that incorporate infant characteristics. Due to the uncertainty regarding the effects of anatomical differences, and consequently the inability to draw clinical conclusions from studies involving pigs, the relevance of this study is significant.

This current study assumes that the absence of RH in pigs is due to lower eye pressure during a shake event compared to humans and hypothesized that the anatomical orbit/eye differences between a pig and an infant indeed result in a difference in eye pressure during shaking. This led to our main question: 'Are pig eyes suitable for conducting experiments to obtain data for IHI-ST in infants?' To address the main question, two sub-questions are posed: 'What are the anatomical differences between pig eyes and human eyes?' And 'which anatomical differences affect the pressure inside the eye between the pig's and the infant's eye during violent shaking?'

1.3. Anatomical aspects of the eye of the human and pig

Aside from the study by Van den Berg et al. [38], a literature search was conducted to investigate the anatomical differences of the eye and its surrounding structures between humans and pigs [17, 27, 29, 32-36]. A table was made with all the anatomical aspects of the eyes and is provided in Appendix B. Anatomical differences refer specifically to the variations in and around the eyes between those of pigs and humans. The conclusions of this literature search showed eight anatomical aspects that differ between pigs and humans which are suspected to influence the RH in IHI-ST. In the current research, the two anatomical aspects, expected to have the most contribution on RH in IHI-ST, will be investigated for the effect on RH during violent shaking. These two differences are further described below.

Orientation of the eye: The optic axes of human eyes are oriented medially at approximately 0° relative to the sagittal axis originating from the lateral geniculate nucleus (Figure 3.A). The optic axes of the eyes of the pig are orientated around 35 degrees relative to the sagittal axis originating from the lateral geniculate nucleus [29] (Figure 3.B). The difference in the orientation of the eye may potentially lead to an increase of eye pressure of the orbit of the human during violent shaking. In repetitive back-and-forth motion of the head, higher pressure may potentially arise in the human eye because it is positioned more towards the front of the head compared to the pig's eye. The human eyes are more directly affected by inertial forces. Since human eyes are more frontally positioned, these forces during a shake event are transmitted more directly to the eye itself, unlike the orientation of the pig's eye.

Closure of the orbit: The human has a bony closure around the eyeball, called a closed orbit. The pig has an open orbit. Instead of the bony structure around the eyeball, a pig has a strong fibrous ligament that is stretched between the frontal bone to the zygomatic bone [17]. The structure of bone around the eye is more rigid around the human eye than that of a fibrous ligament in the pig's eye, which may result in higher pressure in the eye of the human during repetitive back-and-forth motion of the head. The harder structure of the bone, compared to a fibrous ligament, can provide counterpressure, potentially leading to increased pressure buildup in the eye.

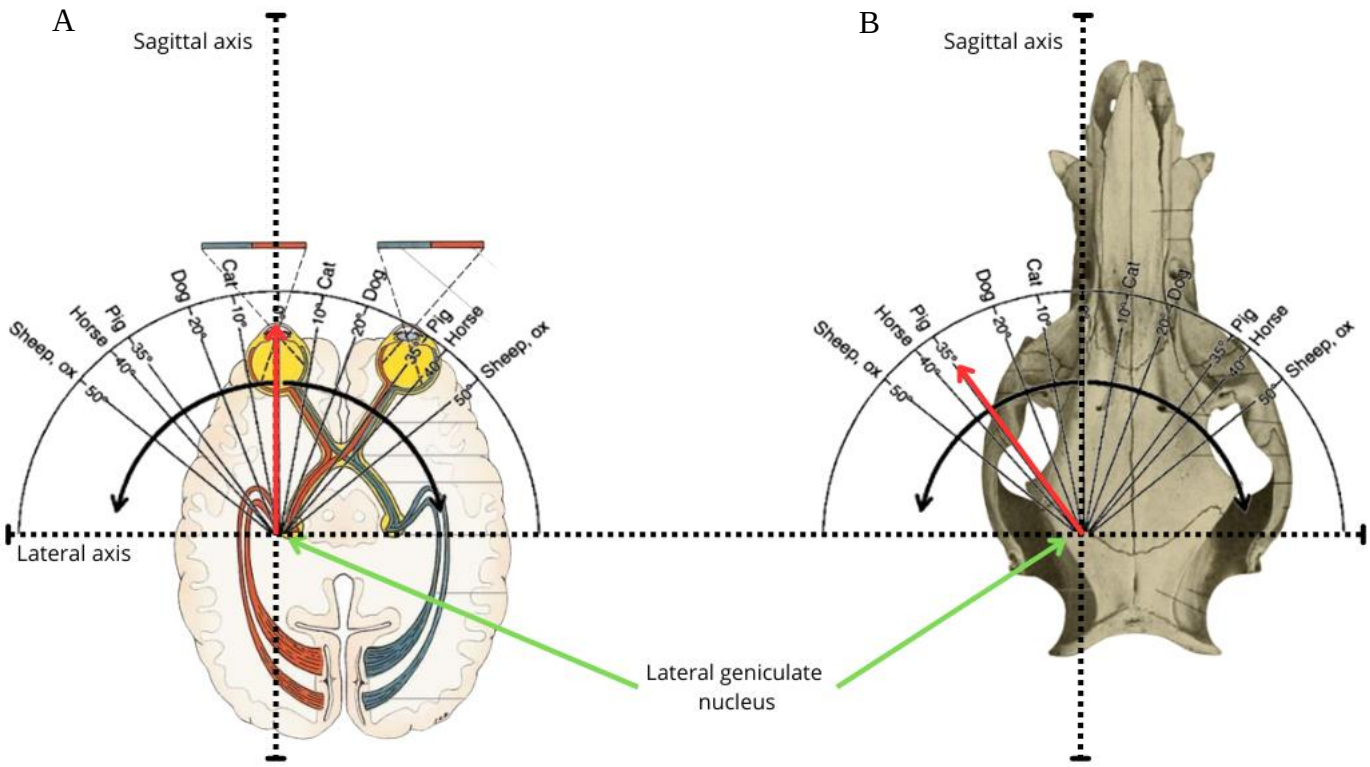

Figure 3: The orientation of the eye of the human (A) and pig (B). The eyes of a human are oriented medially at approximately 0° relative to the sagittal axis originating from the lateral geniculate nucleus (A) . The eyes of a pig are orientated around 35 degrees relative to the sagittal axis originating from the lateral geniculate nucleus (B) [29]. The human eye is positioned more towards the front of the head compared to the pig's eye.

2. Experimental methods & materials

2.1. Experiment setup and materials

In this experiment, two anatomical differences in the eye between infants and pigs were tested for their effect on intraocular pressure during a shake event. These differences were selected based on their feasibility within this research and their potential impact on the intraocular pressure during a shake event (see Appendix B).

To investigate which anatomical difference in the eye causes the pressure difference between the human and pig during violent shaking, an experiment was conducted. The eye models have been simplified compared to an in vivo eye of the human and pig in this study. These eyes models were then placed in an orbit resembling that of a pig and an orbit resembling that of an infant. Subsequently, these eyeballs, in combination with the orbits, were shaken using a shaking simulator. To make the eyeballs, orbits, and shaking movement as representative as possible, design criteria were established (see appendix A).

The goal of this eye model design was to create four models that represent anatomical aspects differing between a pig and human, to assess the effect of these differences on the pressure in the eye. The eyes of a human (infant) were oriented medially around 0° compared to the lateral geniculate body. The eyes of a pig were located lateral compared to the eye of a human and around 35° compared to the lateral geniculate body.

Therefore, we developed four different phantom orbits: infant eye model closed which is fully surrounded by bone and represents the human orbit (Ø.C), infant eye model open which lacks bone around the eye (control group) (Ø.O), pig eye model open which completely lacks bone around the caudolateral side of the eye and with an eye orientation of 35° compared to the lateral geniculate body which represent the pig orbit (35.O) and pig eye model closed in which the eye is fully surrounded by bone and with an eye orientation of 35° compared to the lateral geniculate body (control group)

(35.C). The anatomical aspects compared in this study were the sideways- (pig) or forward-facing (human) orientation of the eye, and an open (human) or closed orbit (pig) (see Figure 4). For technical drawings of the orbit models, see appendix J.

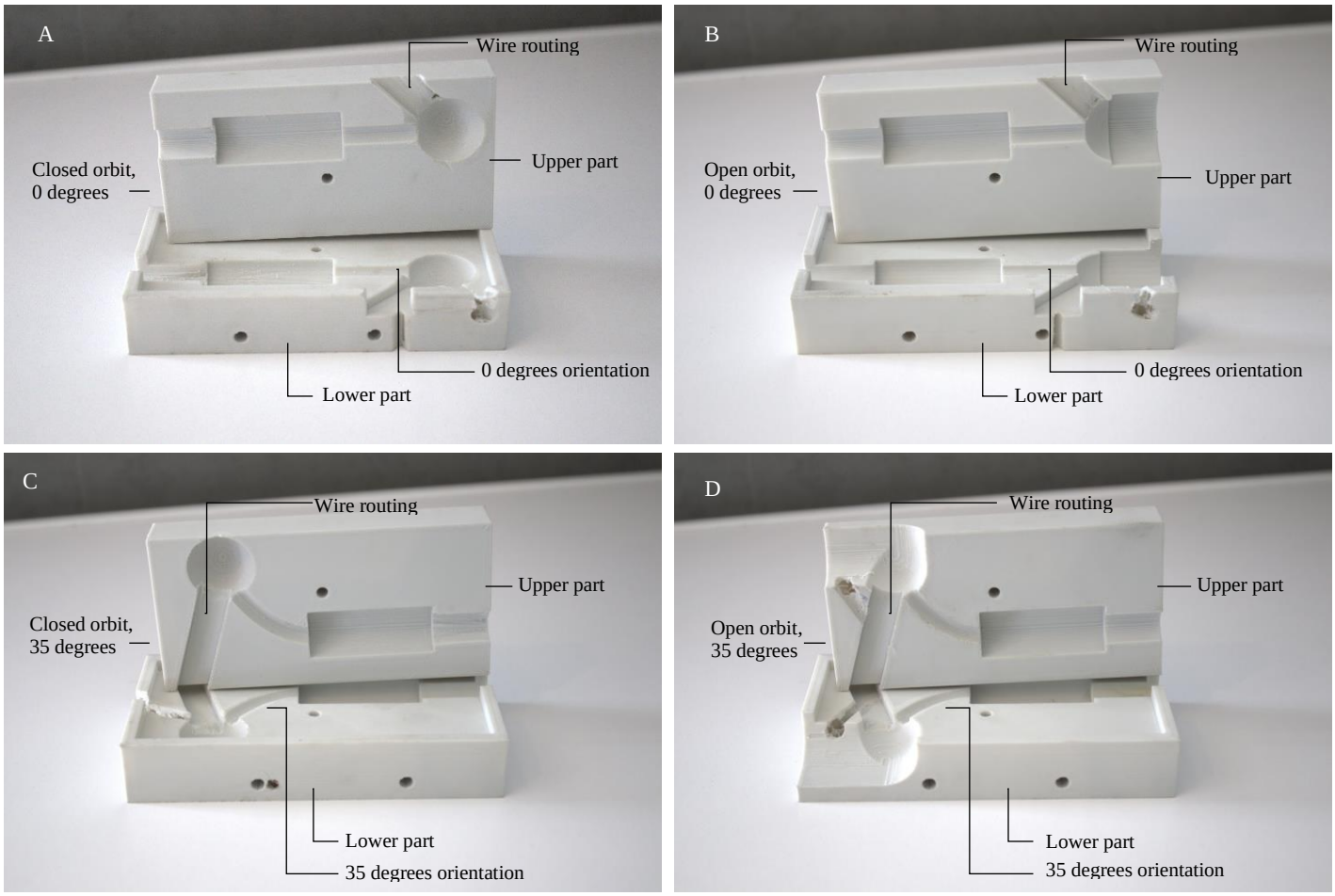

Figure 4: Part A: shows the closed orbit in combination with the 0 degrees orientation (which represents the human orbit). Part B: Shows the open orbit in combination with the 0 degrees orientation (control group). Part C: shows the closed orbit in combination with the 35 degrees orientation (control group). Part D: shows the open orbit in combination with the 35 degrees orientation (which represents the orbit of the pig)

During the experiment, the pressures fluctuations inside the eye in various orbit models during violent shaking were compared. At least two orbit models were required to test the fluctuations in eye pressure during a shake event due to anatomical differences between the eyes of a pig and a human. Appendix D contains the parts and materials used in this study.

The eye models consisted of a ball (representing the eyeball) and tube (representing the artery of the eye) made of silicone, a micro pressure sensor, a custom-made water reservoir, and a pipe fitting (which connects the silicone tube with the custom-made tube) (Figure 6). The ball and the tube were created using silicone filled in a custom-made mould. The mould was 3D-printed using Tough Grey of PLA (Ultimaker). The custom-made mould consisted three parts: the top and bottom of the mould and a metal rod with a holder (see Figure 5 and appendix K for technical drawings).

In the experiment, silicone (Polytek PlatSil Gel-25) (a flexible form of silicone) was used because it was the only material that was neither too thick nor too thin for forming the hollow shape in the eyeball and tube (too thin caused the tube to tear). A ball of PVA (Ultimaker), which dissolves in water, was glued to a rod. The hollow shape of the eyeballs is created by placing a rod and a ball into a mould for casting the silicone. After the silicone has hardened, only the rod is removed from the mould, leaving the ball behind. The ball then dissolves in water, resulting in a hollow eyeball.

The custom-made water reservoir is made from a tube sealed with a sealing clip (see Figure 6). The materials used for the pipe fittings, which connect the ball, tube, and water reservoir, were the Sanivesk Straight Thread Adapter 3/4"M x 1/2"F and Sanivesk Straight Thread 1/2"M x 1/2"M Chrome (Figure 6).

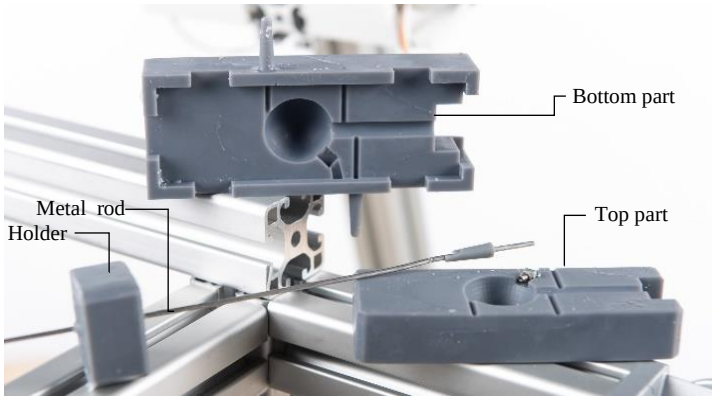

Figure 5: A custom-made mold is shown in this figure. The custom-made mold consists of three parts: the top and bottom of the mold and a metal rod with a holder. The hollow shape of the eyeballs is formed by removing the rod after filling the mold with silicon.

The Honeywell micro pressure sensors from Sparkfun (MPRLS0025PA00001A) were used in this study because they are compact and can fit within the eye. The sensors were connected to a motherboard, which made it impossible to fill the mould. Therefore, before placing the Honeywell micro pressure sensors in the filled mould, the sensors were extracted by heating during the installation process to detach the motherboard from the sensors. Additionally, this would add extra weight to the eye, which would influence the results.

The eye models did contain slight differences due to the moulding process, including variations in wall thickness and the placement of a pressure sensor afterward. Furthermore, because of the heating process, recalibration according to the datasheets of the sensors was needed [20]. As a result of that, the first 10 seconds of every session of the experiment were also used to calibrate the sensors (See paragraph 2.2: Experimental protocol).

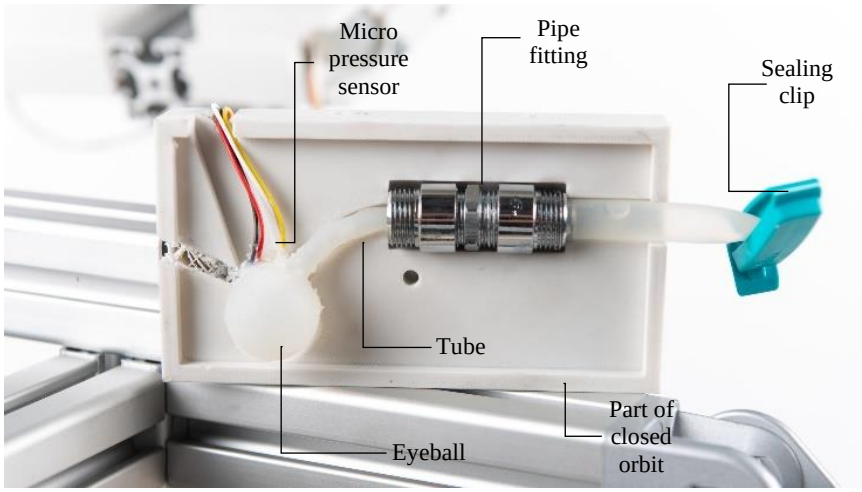

Figure 6: This figure shows the created eyeball in combination with part of the closed orbit. The eyeball, along with the tube, is connected to the micro pressure sensor of Honeywell. The tube from the eyeball is connected to a pipe fitting, which in turn is connected to a tube sealed with a sealing clip.

The shake simulator is a custom-made shaking device (Figure 7.A). The shake simulator was driven by an electro stepper motor Nema 23 (57HS115A44008) and is connected to a Planetary Gearbox (EG23-G5-D8) with a gear ratio of 5:1. Furthermore, a micro step driver (TB660) was connected to the motor to control the speed and direction. The dip-switch settings of the micro step driver is configured as: 'ON, Off, ON; Off, Off, Off' which results in 3.5 Ampere and 400 pulse/resolution (2 micro steps). The motor was connected to an Arduino (see appendix G for the connection diagram of the set up). One arm of the shake simulator was connected to two blind flanges used as flying wheel (Figure 7.B). One blind flange was connected to the motor shaft and the second blind flange was connected to a stationary shaft. The other arm was connected to the custom-made orbits. The experimental setup with the shake simulator that was used during the experiment is shown in Figure 7 (See appendix L for technical drawings).

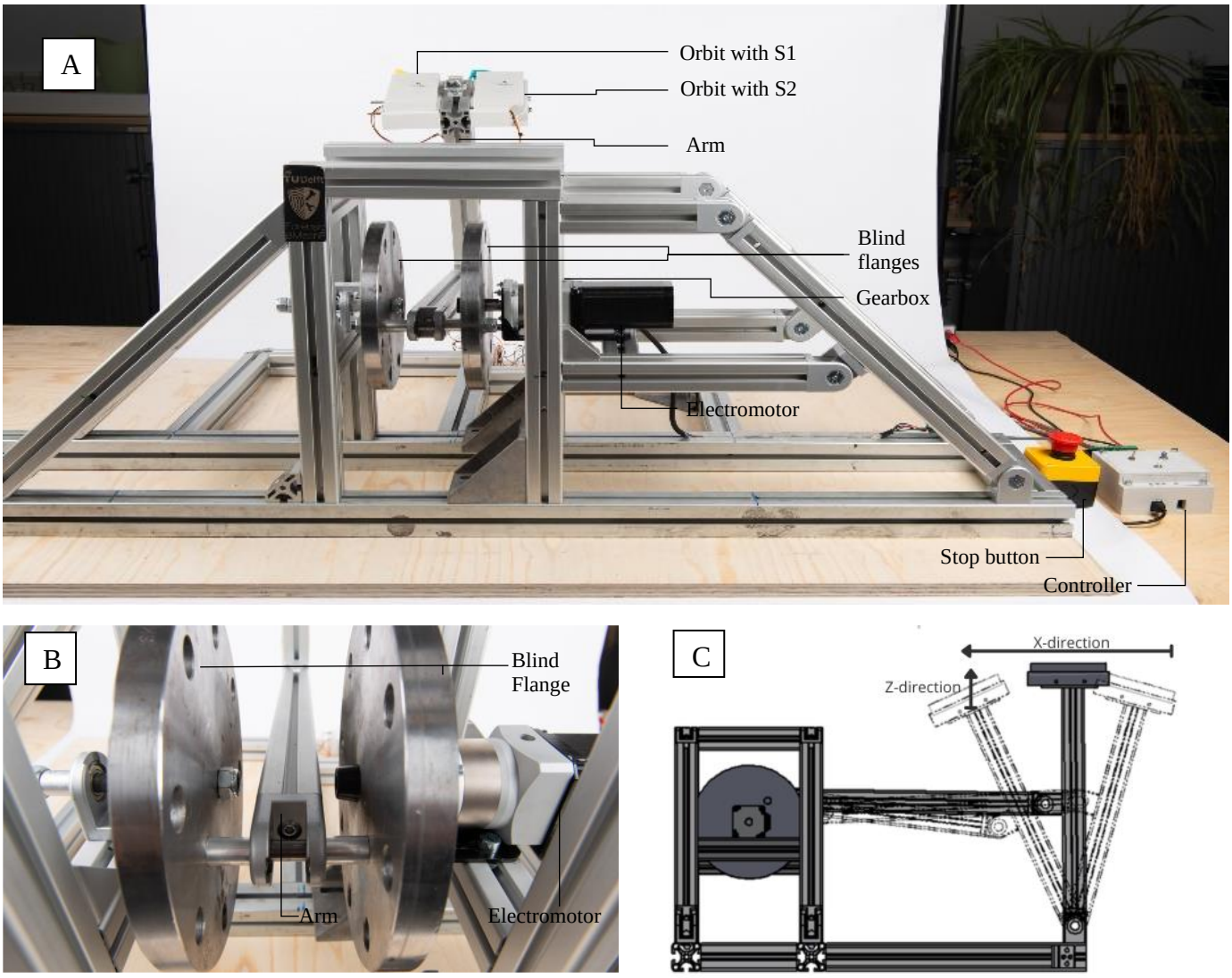

Figure 7: Part A: The experimental setup within the two blind flanges, two orbits, electromotor and gearbox, controller and stop button. The figure shows the two flanges in combination with the arm of the shake simulator. Part B: Shows the zoom-in version of the experimental setup. The blind flanges are shown in combination with the arm and the electromotor. Part C: this figure illustrates the side view of the experimental setup and shows how the movement of the shake simulator occurs. Additionally, it displays the x- and z-directions of the accelerometer.

An accelerometer (GY-61 DXL 335) was used during the experiment to measure the acceleration from the arm of the shake simulator in X and Z direction. The X-direction represents the horizontal movement, such as side-to-side acceleration of the eye model. The X-direction is therefore the tangential direction. The Z-direction represents the vertical movement, such as up-and-down motion of the eye model and is therefore the radial direction (See Figure 7.C). The accelerometer was placed at the top of the arm of the shake simulator (See Figure 8). The accelerometer is already calibrated according to datasheet of the accelerometer.

During the experiments, the shake simulator was positioned in a secure location. This location is an empty space from which the arm of the shake simulator can be controlled at 1 meter distance. Two orbits were placed on the arm of the shake simulator and each orbit contained a micro pressure sensor. Sensor 1 was located on the left and sensor 2 was located on the right when viewed from the front of the shaking simulator in every session (See Figure 8). An emergency stop button was always within reach of the researcher for immediate access for safety reasons.

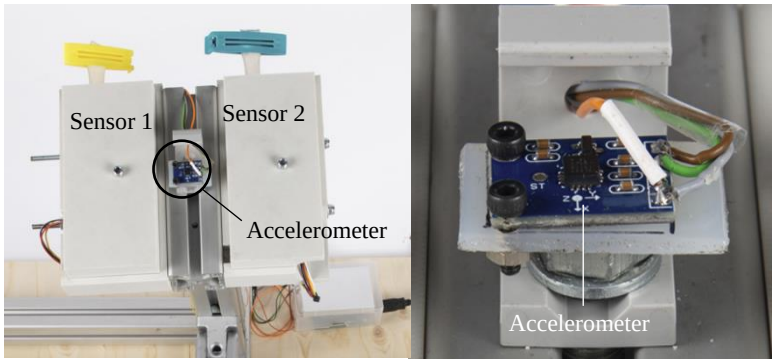

Figure 8: The figure on the left shows two orbits. The left orbit is sensor 1 and the right orbit is sensor 2. In the middle of both orbits is the accelerometer connected. The right figure shows the zoom in version of the accelerometer.

A custom-made controller was used to control the motor. The controller offered an manual mode and a automatic mode (See appendix E for Arduino script). The automatic mode was used in the current study to ensure that the eye pressure was measured at a consistent speed and acceleration. Figure 10 shows a step-by-step procedure for the automatic mode. The manual mode was used for preliminary research. The manual mode can be controlled manually by adjusting the potentiometer, while the automatic mode follows a pre-programmed sequence (see experimental protocol and Appendix D for this pre-established program). When the switch is on the right side, the manual mode is on, and the red light is on. To start the manual mode, the button in the middle of the controller needed to be pressed and the potentiometer needed to be switched. This was done for safety reasons, as it ensures that the motor cannot be started without pressing the button. The second red LED is on when the motor is rotating. Figure 9 shows a step-by-step procedure for the manual mode.

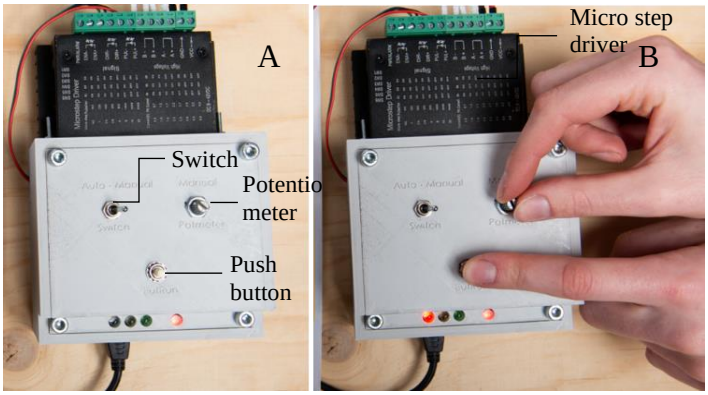

Figure 9: The custom-made controller of the shake simulator connected with the micro step driver. In part A, the switch is set to manual mode. When the manual mode is on, the orange LED turns on. In part B, the push button is pressed simultaneously with the potentiometer. This is done for safety reasons. Once this is done, the red LED lights up, indicating that the motor is starting to rotate.

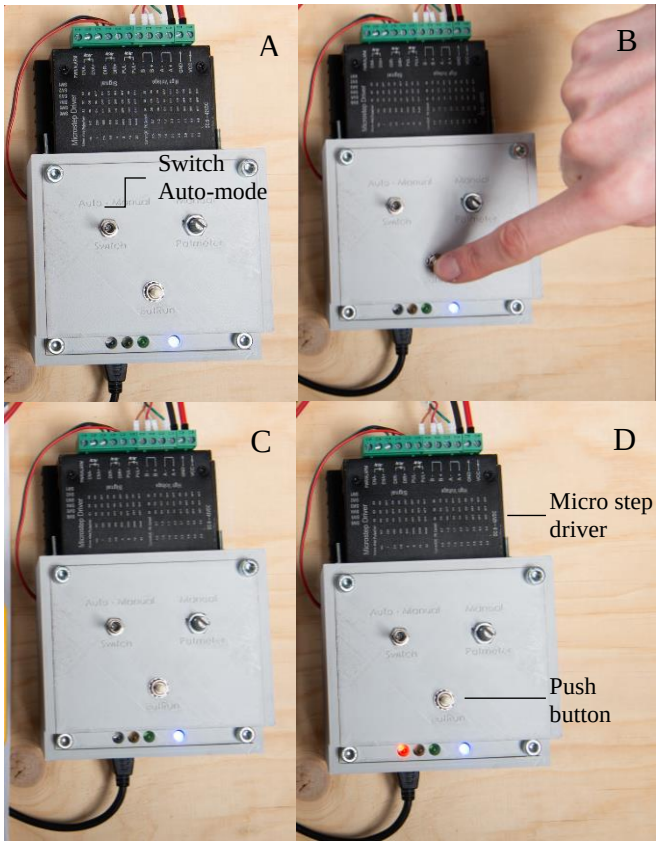

Figure 10: The custom-made controller of the shake simulator connected with the micro step driver. If the switch is to the left, the auto mode is on. In this figure, the auto mode is on. The LED light then turns blue (A). When the push button is pressed (B), the motor starts rotating (C). The LED lights will then change from green to orange (C), which is not fully visible in the figure. Once the motor reaches its maximum speed, the LED turns red (D).

2.2. *Experimental protocol*

The experiment consisted of twelve sessions involving combinations of orbit models. Due to the eye models not being completely identical, there was a switch of eye models per orbit during the experiment. Additionally, the eye models were randomly placed inside the phantom orbit and interchanged between different orbits. During the experiment, the eye models are placed in the orbits and these orbits are then attached to the arm of the shake simulator. This is conducted in a Latin square design (see Table 1). Each session is performed five times (trials).

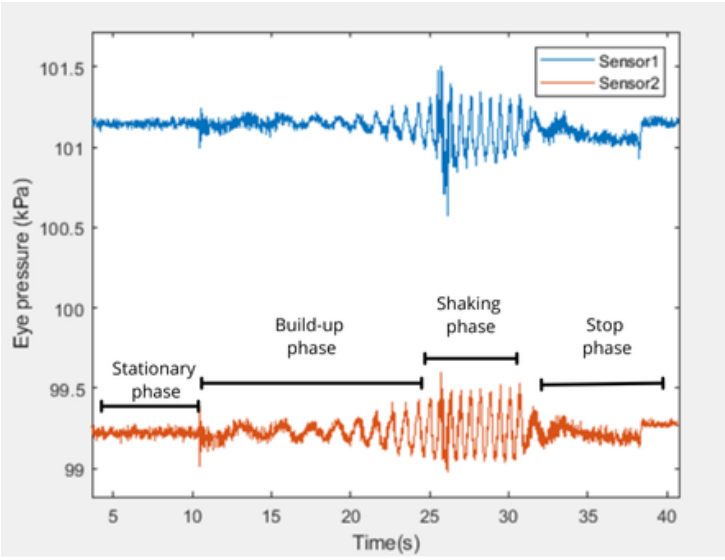

Figure 11: The figure shows the overall average measurement of 35.O - 35.C. The first 10 seconds were used to calibrate the data (stationary phase). Subsequently, the shake simulator accelerated over the next 15 seconds (build-up phase) to reach the speed at which measurements were taken (shaking phase). At the 25-second mark, data measurement begins, and after these 5 seconds, the device decelerates until it eventually comes to a stop (stop phase).

Each trial of the shake experiment lasted 40 seconds, within which there were 5 seconds during which the shaking device kept a constant speed (**shaking phase**) (Figure 11). The 10 seconds were called **the stationary phase** because the motor not running in this part and the arm of the shake simulator is not moving. **The stationary phase** was used as calibration. This calibration was used to calibrate when both eyeballs were filled with water and compensate for a zero bias. After these 10 seconds, the motor started running and building up the speed in 15 seconds (**build-up phase**). During the 5 seconds of a constant speed, the data was compared **(shaking phase)**. This was following the requirements of RB.2 of appendix A. After these 5 seconds, the motor slowed down and stopped within 3 seconds **(stop phase)**.

Table 1: Experimental protocol; Each session consists of two different orbit models and two different eye models. EM.1.18; Eye Model 1 with micro pressure sensor address 18. EM.2.28 with micro pressure sensor address 28, Ø.O; Infant eye model (open), Ø.C; Infant eye model (closed), 35.O; Pig eye model (35 degrees & open), 35.C; Pig eye model (35 degrees &closed)

	Ø.O (1)	**Ø.C (2)**	**35.O (3)**	**35.C (4)**
Session 1	EM.1.18	EM.2.28		
Session 2			EM.1.18	EM.2.28
Session 3	EM.1.18		EM.2.28	
Session 4	EM.1.18			EM.2.28
Session 5		EM.2.28	EM.1.18	
Session 6		EM.2.28		EM.1.18
Session 7	EM.2.28	EM.1.18		
Session 8			EM.2.28	EM.1.18
Session 9	EM.2.28		EM.1.18	
Session 10	EM.2.28			EM.1.18
Session 11		EM.1.18	EM.2.28	
Session 12		EM.1.18		EM.2.28

2.3. Data acquisition

The data of the accelerometer and the Honeywell micro pressure sensor of all five trials from twelve sessions including calibrations were recorded with an Arduino (See appendix F). The data was sampled with sample frequency of 70 Hz to capture the small pressure variations during violent shaking [20].

The data of the accelerometer was used to check whether the frequency of the shake simulator was consistent during each session and between all sessions. Furthermore, the recorded X and Z direction during the shake event was used to compare the accelerations were used to compare the shaking fierceness with the data from Schiks et al. [1] and according to RB.1 and RB.7.

3. Method: Data analysis

3.1. Data filtering

After visualization the data of the unfiltered signals of the accelerometer and micro pressure sensor data in MathWorks MATLAB, a high-frequent noise was noted (See appendix H for script). The data from trials 25 (Ø.O - Ø.C), 32 (35.C - 35.O), and 35 (35.C - 35.O) were erroneous measurements due to technical errors, as these data were mechanically implausible. Therefore, these data were excluded from the analysis. Welch's power spectral density analysis of the data showed that high power noise peaks were present at frequencies above the frequency bandwidth of the accelerometer data and the micro pressure sensor data (see Figure 12, Figure 13 and Figure 14). The measured frequency observed by visually analysing the shaking simulator was around 3 Hz during the shake event. Therefore, frequencies above this measured frequency were expected to be noise and were filtered out. A Butterworth second-order low-pass zero-phase digital filter with a cutoff frequency of 6 Hz was applied to smooth the accelerometer signals and a Butterworth second-order low-pass zero-phase digital filter with a cutoff frequency of 3 Hz in the flat period (when the shaking simulator did not move) and 6 Hz in the static period was applied. Thereby enabling the algorithm to calculate in the static period was applied to smooth the micro pressure sensor signals.

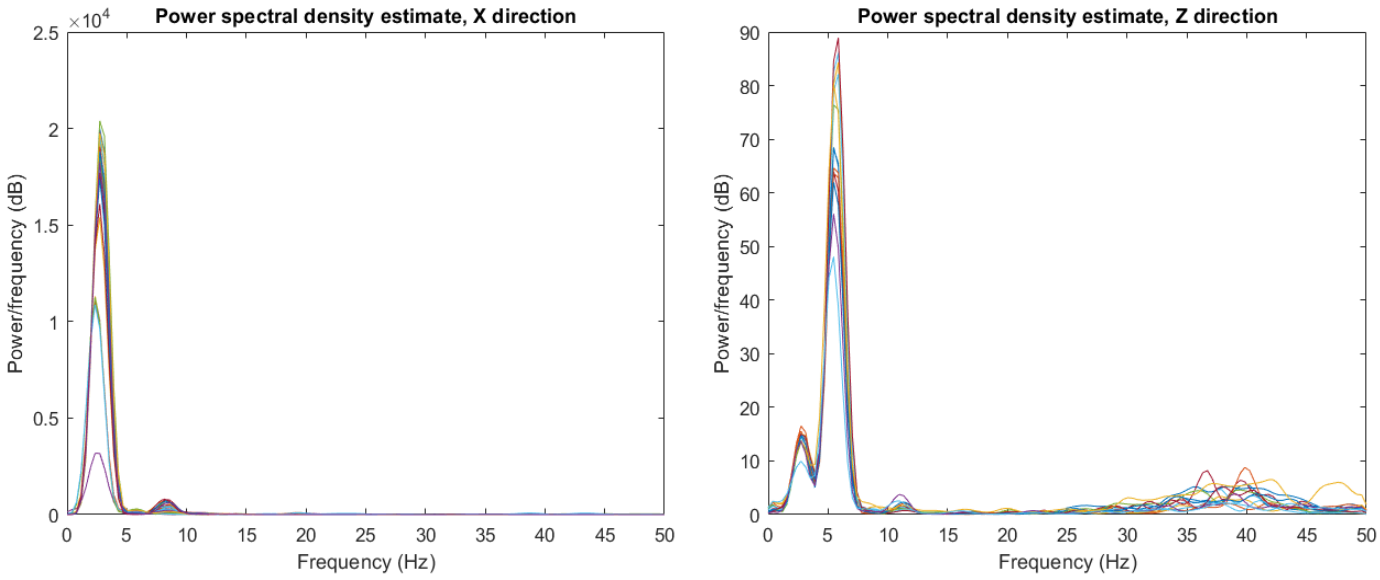

Figure 12: Both figures present the power spectral density (PSD) estimates of the signals of the accelerator. A Welch's power spectral density analysis was conducted on the acceleration data from the x-direction and z-direction. On the left side, the PSD of the x-direction is displayed. This figure shows that the measured frequency is approximately around 3 Hz, which corresponds to the frequency observed after visually analyzing the shake simulator. The high noise around 8 Hz was filtered out. On the right side, the PSD of the z-direction is shown, which initially exhibits more noise in the signal. The measured signal was around 3 Hz, with everything outside this range being filtered out.

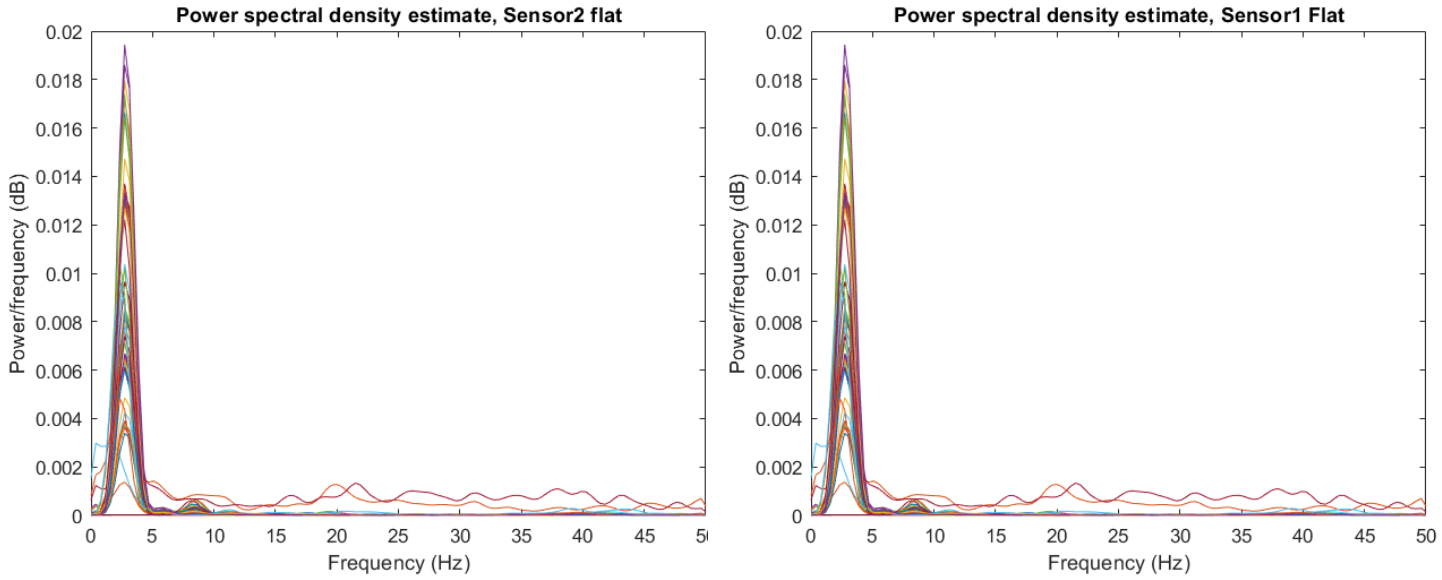

Figure 13: Both figures present the power spectral density (PSD) estimates of the signals of the sensors in the static period. A Welch's power spectral density analysis was conducted on the sensor data from the first ten seconds of the shaking part of the session. On the left side, the PSD of sensor 1 is displayed, and on the right, the PSD of sensor 2. This figure shows that the measured signal contains noise but with low power.

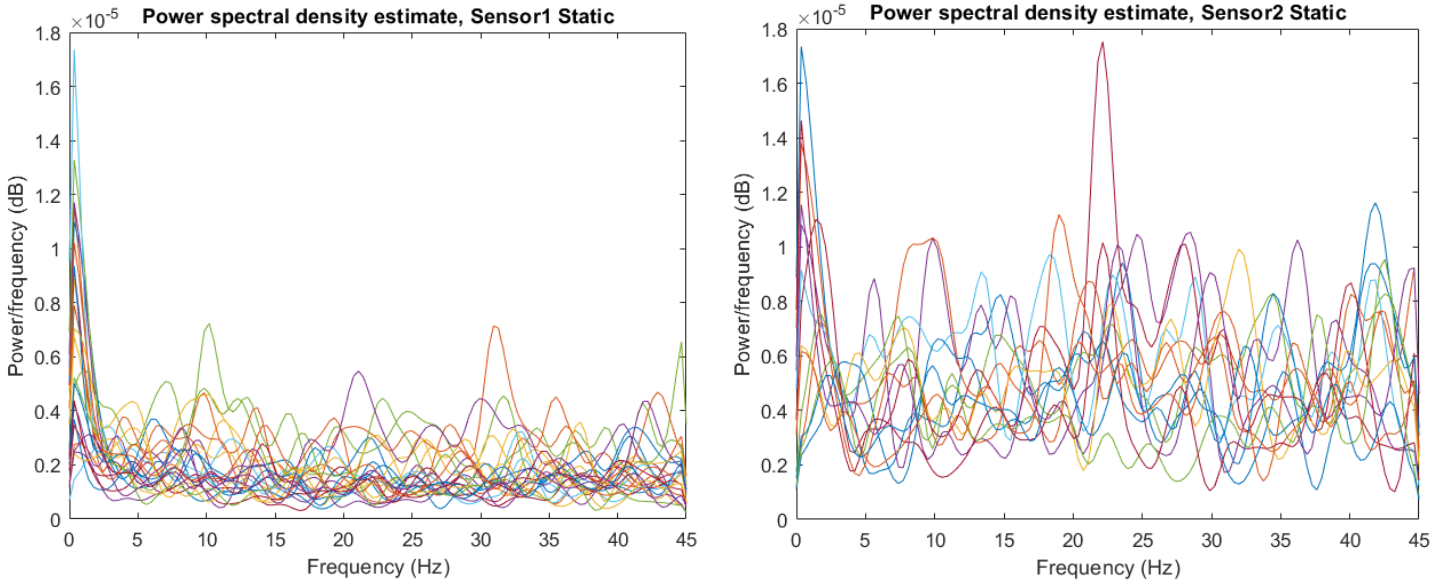

Figure 14: Both figures present the power spectral density (PSD) estimates of the signals of the sensors in the flat period. A Welch's power spectral density analysis was conducted on the sensor data in the five seconds of the shaking part of the session. On the left side, the PSD of sensor 1 is displayed. This figure shows that the measured frequency is approximately around 3 Hz, which corresponds to the frequency observed after visually analyzing the shake simulator. The high noise around 8 Hz is filtered out. On the right side, the PSD of sensor 2 is shown, which initially exhibits more noise in the signal. The measured signal is around 3 Hz, with everything outside this range being filtered out.

3.2. Calculations

3.2.1. Accelerations

The accelerometer measured the accelerations in the x- and z-direction of the eye models during a shake event (aorbit-max (m/s^2)). After filtering the data, the baseline phase is subtracted from the signals to compensate for the gravity. Subsequently, a resultant was calculated per session from the data of the x- and z-directions. This resultant vector was determined by this formula: $|a| = \sqrt{(a_x^2 + a_Z^2)}$. a_x means the accelerations in the x-direction, a_z means the acceleration in the z-directions. This results in an acceleration factor (aR) (See Figure 15).

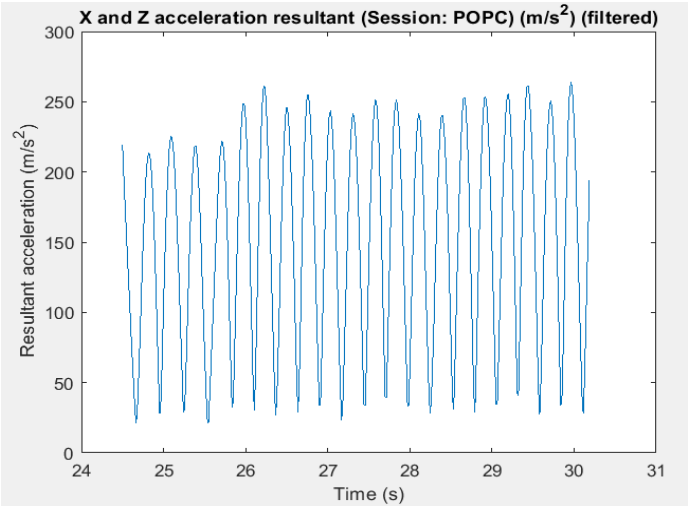

Figure 15: The resultant vector (aR) of the x- and z-direction combined. This figure shows an example of the resultant of session POPC.

3.2.2. Eye pressure data

After filtering the data, the baseline phase (Pb) is first subtracted from the shaking phase (Ps) to compensate for the atmospheric pressure (Pbs). Subsequently, all maximum (ΔPbs-A) and minimum (ΔPbs-B) values of the shaking phase are obtained from the signal. These maximum and minimum values represent the amplitude between Ps and the peaks of the shaking phase. These values are referred as ΔPbs (ΔPbs-A, ΔPbs-B) (see Figure 16).

Each shake movement of the shake event was not performed with equal intensity and frequency because mechanical variability in the shake simulator could cause slight differences in the intensity and frequency of the shake. As a result, we have unequal reference values. Due to the presence of unequal reference values in this study, the first step is to correct the accelerations. The average pressure difference per session is divided by the average resultant of the x- and z-directions (aR) per session.

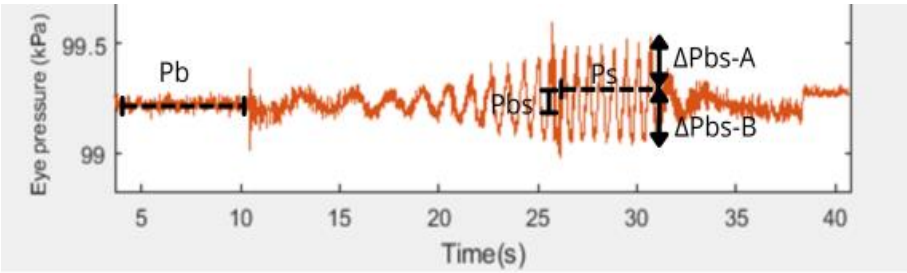

Figure 16: This figure presents the average signal from 5 trials of a randomly selected sensor. The first 10 seconds of the shaking motion are referred to as the pressure baseline (Pb). The signal between seconds 25 and 30 is referred to as the pressure signal (Ps). The difference between Pb and Ps is denoted as Pbs. The final maximum and minimum values of the Ps signal are referred to as ΔPbs-A, ΔPbs-B.

It is assumed that the eyeballs did not gradually deflate during the experiment, which could cause differences in intraocular pressure that may affect the results of the current study.

3.3. Statistics

IBM SPSS 26 was used for the statistical analysis. To test whether the data is normally distributed, the Shapiro-Wilk normality test was performed. The Shapiro-Wilk normality test showed that that Ø.O, Ø.C, 35.O, 35.C for both sensors are not normally distributed ($p < 0.001$). As a result of the non-normality, the non-parametric Friedman's ANOVA (χ^2) test was chosen for the analysis. To understand whether there was a difference in orbit between a human and a pig, as well as in sensor variables during the experiment. Furthermore, the Post hoc analysis with Wilcoxon signed-rank tests was conducted with a Bonferroni correction applied because this post hoc analysis provided further insights into which differences in orbit cause increased pressure in the eye. By adjusting for multiple comparisons, the Bonferroni correction helped mitigate the risk of Type I errors (see Appendix I for the complete analysis).

4. Results

4.1. Eye pressure data

The detailed findings for each orbital configuration and their corresponding average relative eye pressure variations are shown in Table 2 and Table 3. These tables indicate that certain orbital configurations consistently result in higher or lower relative eye pressure, reflecting the influence of the orientation and closure of the orbit on intraocular pressure.

Table 2: The mean relative pressure variation between the orbits divided by the resultant for sensor 1.

ΔPbs/aR sensor 1	**Ø**	**35**
Open	1.66e-04 kPa	6.30e-04 kPa
Closed	1.55e-03 kPa	6.97e-04 kPa

Table 3: The mean relative pressure variation between the orbits divided by the resultant for sensor 2.

ΔPbs/aR sensor 2	**Ø**	**35**
Open	3.60e-04 kPa	1.11e-03 kPa
Closed	4.34e-04 kPa	3.91e-04 kPa

Figure 17 shows the distribution of the measurements from this current study in boxplots for each orbit combination per sensor. This figure shows that the spread of Ø.C1 and 35.O2 is large compared to the other orbit combinations, indicating greater variability in relative eye pressure for these configurations.

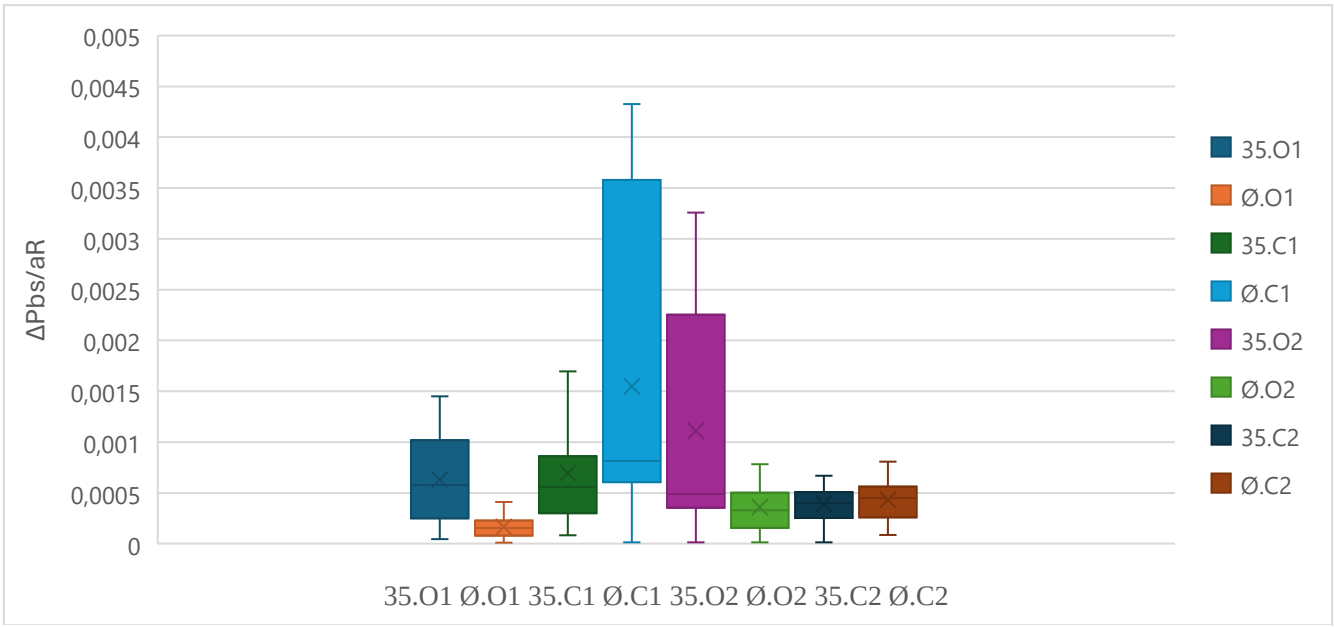

Figure 17: This figure shows the distribution of the data from this study in box plots for each orbit combination.

4.2. Statistics

According to the results, there are significant differences in the average relative eye pressure between the open and closed orbit conditions at 0 and 35 degrees. The Friedman's ANOVA (χ^2) test shows that there was a statistically significant difference between Ø.O, Ø.C, 35.O, and 35.C in both sensors (see appendix I).

Table 4 and Table 5 presents the statistical analysis of Wilcoxon Signed Ranks Test of the current study, where the median values represent the relative eye pressure. Post hoc analysis using the Wilcoxon signed-rank test showed significant differences in eye pressure between the following combinations for sensor 1: Ø.O - Ø.C, Ø.O - 35.C, Ø.O - 35.O, Ø.C - 35.C, and Ø.C - 35.O. For sensor 2, significant differences were found between the combinations Ø.O - Ø.C, Ø.O - 35.O, Ø.C - 35.O, and 35.O - 35.C. Based on these results in tables 5 and 6, it appears that the closed orbit more frequently has a higher relative eye pressure than the open orbit. The only exception is the combination of the open orbit with 35 degrees in sensor 2, where this combination potentially results in an equal relative eye pressure compared to the closed orbit. Furthermore, the Ø.O consistently shows a lower relative eye pressure than the other three orbits across all combinations. This is also evident in the comparison between Ø.O - 35.O, where 35.O exhibits higher relative eye pressure than Ø.O. In the combination of Ø.C - 35.O of orbits which represents the most closely resemble of the actual orbits of the human and pig, shows Ø.C a higher relative eye pressure than 35.O in Sensor 1 and an equal relative eye pressure in sensor 2, which may result from the combination of the closed orbit and 0 degrees. See Appendix I for a full overview of the statistical analysis of the current study.

Table 4: The statistical analysis of the study variables for sensor 1. The Wilcoxon signed- rank is performed. The red color and bold font show the significant and the highest median of the relative eye pressure per orbit combination The underline shows the orbit combination of the most closely resemble the actual orbits of the human and pig.

ΔPbs sensor 1	**Median**	**Median**	**Z-score**	**Sig.**
Ø.O - Ø.C	Ø.O (median = 1,55e-04 kPa)	**Ø.C (median = 8,15e-04 kPa)**	-6.00	**P < 0.001**
35.O - 35.C	35.O (median = , 5,58e-04 kPa)	35.C (median = 5,56e-04 kPa)	-0.52	P = 0.96
Ø.O - 35.O	Ø.O (median = 1,55 e-04 kPa)	**35.O (median = 5,58e-04 kPa)**	-6.53	**P < 0.001**
Ø.C - 35.C	**Ø.C (median = 8,15e-04 kPa)**	35.C (median = 5,56e-04 kPa)	-3.11	**P = 0.002**
Ø.C - 35.O	**Ø.C (median = 8,15e-04 kPa)**	35.O (median = 5,58e-04 kPa)	-4.70	**P < 0.001**
Ø.O - 35.C	Ø.O (median = 1,55e-04 kPa)	**35.C (median = 5,58e-04 kPa)**	-6.67	**P < 0.001**

Table 5: The statistical analysis of the study variables for sensor 2. The Wilcoxon signed- rank is performed. The red color and bold font show the significant and the highest median of the relative eye pressure per orbit combination The underline shows the orbit combination of the most closely resemble the actual orbits of the human and pig.

ΔPbs sensor 2	**Median**	**Median**	**Z-score**	**Sig.**
Ø.O - Ø.C	Ø.O (median = 3,28e-04 kPa)	**Ø.C (median = 4,50e-04 kPa)**	3.15	**P = 0.002**
35.O - 35.C	**35.O (median = 4,90e-04 kPa)**	35.C (median = 4,00e-04 kPa)	-3.77	**P < 0.001**
Ø.O - 35.O	Ø.O (median = 3,28e-04 kPa)	**35.O (median = 4,90e-04 kPa)**	-3.59	**P < 0.001**
Ø.C - 35.C	Ø.C (median = 4,50e-04 kPa)	35.C (median = 4,00e-04 kPa)	-0.90	P = 0.37
Ø.C - 35.O	Ø.C (median = 4,50e-04 kPa)	**35.O (median = 4,90e-04 kPa)**	-3.54	**P < 0.001**
Ø.O - 35.C	Ø.O (median = 3,28e-04 kPa)	35.C (median = 4,00e-04 kPa)	-1.36	P = 0.17

4.3. Shaking pattern of the shake simulator

The data from the shake simulator is also used to verify whether the accelerations correspond to real shaking. The acceleration pattern of the shake simulator mimicked the shaking motion of violent shaking because it is comparable to the acceleration pattern of the data from Schiks et al. [1] (see Figure 18). In this figure, the x-, y-, and z-directions of the accelerations can be seen. According to the study by Schiks et al. [1], the mean center of gravity (COG) acceleration was 155 m/s² in the x-direction, and the maximum COG acceleration was 276 m/s² in the x-direction. The current study showed that the maximum acceleration of the eye model during the shake event was 264 m/s² in the x-direction which corresponds with the results of Schiks et al. [1]. Additionally, it also meets the pre-established requirement RB.5.

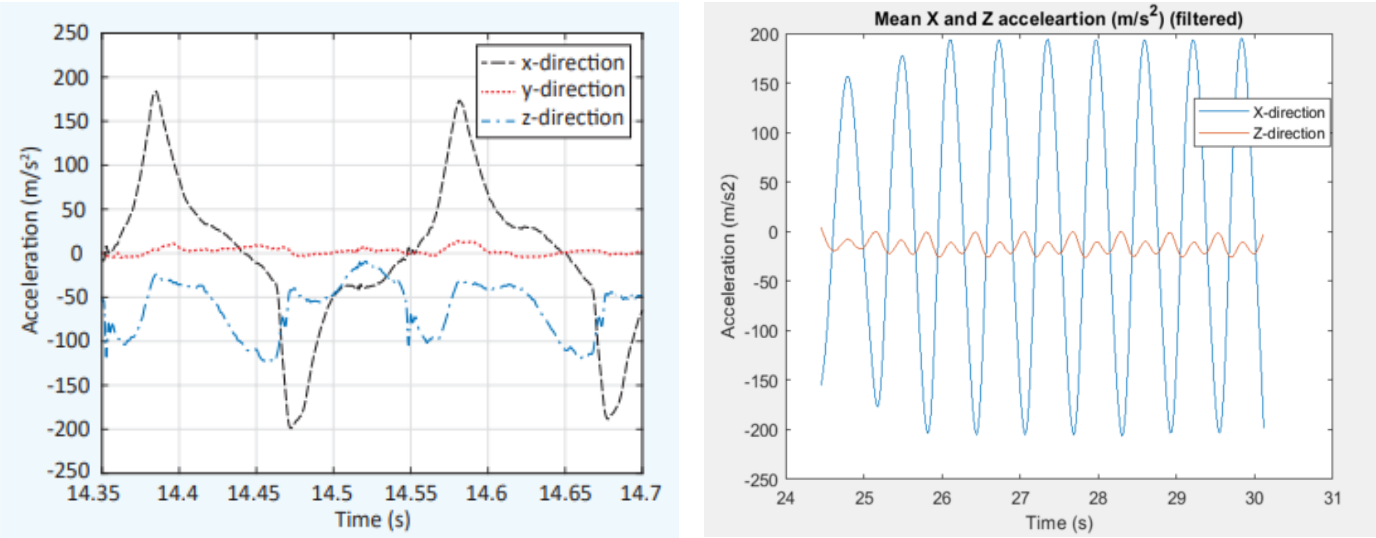

Figure 18: The left figure shows one typical vertex accelerations of the dummy's head during violent shaking in the experiment conducted by Schiks et al. [1]. In this figure, the x-, y-, and z-directions of the accelerations are shown. The mean centre of gravity (COG) acceleration is approximately 155 m/s², with a maximum COG acceleration of 276 m/s². The right figure illustrates the accelerations of the combination of 35.O - 35.C during violent shaking in this experiment. In this figure, the x- and z-directions are displayed as the y-direction was not measured. The maximum acceleration recorded is 264 m/s² in the x-direction.

5. Discussion and limitations

5.1. Discussion

This study aimed to investigate whether differences in pressure variations within the eye occur between pigs and humans during an IHI-ST event and whether these could be caused by the anatomical differences between the orbital cavities. Through a literature search, eight anatomical differences between pigs and humans potentially influencing RH in IHI-ST were identified. The two potentially relevant anatomical differences which are the orientation of the eye, and the closure of the orbit are expected to have the most significant impact on RH, were examined in the current study.

To investigate whether these anatomical differences contribute to an increase in intraocular pressure, four orbits were created that combined eye orientation and orbital closure. Handcrafted eye models were then placed within these orbits, and a shaking simulator was used to apply the shake motion.

The findings of the current study indicate that the relative eye pressure is higher in closed orbits compared to open orbits at 0 degrees. This suggests that the enclosed nature of the closed orbits contributes to an increase in intraocular pressure when the orientation of the eye does not play a role. This may be due to the restricted space, limiting fluid distribution and causing pressure buildup. At 35 degrees, the relative eye pressure is equal between the open and closed orbits, indicating that the angle may play a role in eye pressure during a shake event.

For closed orbits, the relative eye pressure was higher at 0 degrees than at 35 degrees. This may be since the humans' eye (with an orientation of 0 degrees) are more frontally positioned, meaning that forces during a shake event are transmitted more directly to the eye itself, unlike the orientation of 35 degrees of the pig's eye. However, in open orbits,

the relative eye pressure was higher at 35 degrees than at 0 degrees. This could be explained by the fact that at a 35-degree orientation, the eye may be less protected by the surrounding structures of the orbit, allowing forces to be transmitted more directly to the eye itself. In open orbits, where there is no complete enclosure to support the eye, the 35 degrees orientation can lead to greater displacement or deformation of the eye, resulting in higher relative eye pressure.

The closed orbit in combination with the 0 degrees orientation (which represents the human orbit) shows a higher relative eye pressure than the open orbit in combination with the 35 degrees orientation (which represents the piglet orbit) in sensor 1 and sensor 2, an equal relative eye pressure. Additionally, almost eight closed orbits exhibit higher relative eye pressure. This can be explained by the fact that the structure of the closed orbit may exert additional pressure on the eye when the eye impacts the orbit, resulting in higher relative eye pressure. These results indicate that the effect of orbital closure is greater than the effect of the difference in eye orientation.

Previous studies by Umstead et al. [19] and Coats et al. [18] found no evidence of RH in pigs during shake events, suggesting that the pig's orbital structure might limit eye pressure build-up during a shake event. This aligns with our findings, as the pig orbit configuration at 35 degrees (35.O) in our study shows lower relative eye pressure than the infant model (Ø.C), supporting the notion that pigs experience lower eye pressures during shake events compared to infants. This is also consistent with the initial hypothesis of the current study. The results of this current study thus indicate that pressure buildup in the eye during a shake event is higher in an infant than in a pig. This difference in pressure buildup is due to the anatomical differences in the eye between humans and pigs, with the difference in orbital closure playing a significant role in eye pressure buildup.

5.2. Validity

The validity of the findings is a critical concern and presents limitations for the study. The external validity, or the extent to which the findings can be generalized to other populations or settings, is constrained by using artificial, highly simplified human and pig eye models. The anatomical differences between these models and human eyes limit the applicability of the findings to clinical settings involving human infants.

Construct validity, which refers to the degree to which the study accurately measures the theoretical constructs it intends to measure, is challenged by the differences in eye models and orbits used. While efforts were made to align these models with human and pig anatomy, practical constraints limited their exact replication. Furthermore, because the eyeballs were cast in a mold, the wall thickness of the eyeballs and tubes may vary, making the eyeballs potentially non-identical. Additionally, the silicone material used does not perfectly replicate the biomechanical properties of real eye tissue, and the complexity of fluid dynamics, ocular structure, and interactions with surrounding soft tissue (such as the muscles around the eye) are simplified in this study.

These validity factors limit the accuracy and applicability of the current study's findings, underscoring the need for further research with more precise models.

5.3. Limitations

A plausible explanation for the divergent findings between sensors in this current study could be the presence of other anatomical differences between the pig's and human's orbits. Furthermore, both eyeballs are surrounded by muscles that protect and rotate the eyes which was not included in this study. The eye models and orbits used in this study do not precisely replicate those of humans and pigs. Due to practical constraints, meeting all initial requirements for comparing human and pig eyes and orbits was impractical.

The influence of neck stiffness was not examined in this study. Future research should include the measured accelerations in the current study and compare them to those measured in the pig experiments, hypothesizing that the differences in relative eye pressure may be attributed to the lower accelerations observed in surrogate experiments.

The measurements were also not conducted at varying speeds, limiting the study's ability to account for speed-related variations in pressure readings. Future studies should incorporate measurements at different speeds to comprehensively analyse the impact of speed on observed pressure differences.

Another limitation was that the wall thickness of the two eye models differs due to the manual process casting the silicone into the mold. Thicker walls may result in a reduced ability to deform under pressure, while thinner walls might be more susceptible to deformation. This variability can lead to inconsistent relative eye pressure readings between different eye models. A follow-up study could focus on standardizing the production of the eye models to minimize variations in wall thickness. For example, using automated manufacturing methods could ensure a more consistent wall thickness. Additionally, the follow-up study could investigate how different wall thicknesses affect the eye's ability to deform under pressure.

In this study, the eye pressure difference results were divided by the mean resultant of the x- and z-accelerations to compensate for possible variations in acceleration. The choice in the current study was made to use the mean resultant. However, in a follow-up study, each eye pressure peak should be divided by the corresponding acceleration peak instead of the mean. This approach will allow for a more detailed examination of the effects of accelerations.

Even though this relative eye pressure data had already been compensated for the acceleration resultant, this inconsistency of the data raises concerns regarding data reliability. A possible cause for this might be that the eyeballs deflated during the experiment. It is expected that the eye models deflate at a consistent rate over time. Therefore, the relative eye pressure at the beginning of the experiment may be higher than at the end because the pressure in the eyeballs decreases.

6. Conclusions

The aim of this study was to gain a deeper understanding of the effect of anatomical differences between pigs and humans on eye pressure during a shake event. The main research question was: Are pig eyes suitable for conducting experiments to obtain data for IHI-ST in infants? With sub-questions: What are the anatomical differences between pig eyes and human eyes? And which anatomical differences affect the pressure inside the eye between the pig's and the infant's eye during violent shaking?

Based on the literature search, the two anatomical aspects expected to have the most significant impact on RH in IHI-ST are orbital closure and eye orientation. The results of the current study show significant eye pressure differences between various orbit combinations. The infant model produces higher relative pressure than the pig model which may indicate that due to the anatomical differences between the eyes of pigs and humans, higher eye pressure occurs during shaking in humans compared to pigs. The results of this study thus suggest a cautious conclusion that the eyes of pigs may not be suitable for research material in the context of IHI-ST.

By addressing the limitations and following the recommendations, future research can improve the reliability and relevance of the findings, leading to a better understanding of eye mechanics during shaking events. This study has taken the first steps toward investigating the effect of anatomical differences between the eyes of humans and pigs on eye pressure during a shake event. Furthermore, a shake simulator was developed for the current study, which can be used in future research on IHI-ST. This setup and the study's findings lay the groundwork for future research.

In summary, while this study offers valuable insights into how anatomical differences impact eye pressure during shaking, future research should improve develop more accurate eye models and design experiments that account for anatomical and physiological complexities of the eye.

Bibliography

1. Schiks, L.A.H.D., J.; Loeve, A.J. , Inflicted Head Injury by Shaking Trauma in Infants : Part I: the potential effect of spatiotemporal variation of the rotation center

on injury mechanisms. 2021, TU Delft.
2. Sieswerda-Hoogendoorn, T., et al., Educational paper: Abusive Head Trauma part I. Clinical aspects. Eur J Pediatr, 2012. 171(3): p. 415-23.
3. Eisele, J.A., et al., Nonfatal traumatic brain injury-related hospitalization in very young children-15 states, 1999. J Head Trauma Rehabil, 2006. 21(6): p. 537-43.
4. Ellingson, K.D., J.M. Leventhal, and H.B. Weiss, Using hospital discharge data to track inflicted traumatic brain injury. Am J Prev Med, 2008. 34(4 Suppl): p. S157-62.
5. Barlow, K.M., et al., Late neurologic and cognitive sequelae of inflicted traumatic brain injury in infancy. Pediatrics, 2005. 116(2): p. e174-85.
6. Case, M.E., Inflicted traumatic brain injury in infants and young children. Brain Pathol, 2008. 18(4): p. 571-82.
7. Squier, W., The "Shaken Baby" syndrome: pathology and mechanisms. Acta Neuropathol, 2011. 122(5): p. 519-42.
8. Togioka, B.M., et al., Retinal hemorrhages and shaken baby syndrome: an evidence-based review. J Emerg Med, 2009. 37(1): p. 98-106.
9. Levin, A.V., et al., Retinal hemorrhage in abusive head trauma: finding a common language. Trans Am Ophthalmol Soc, 2014. 112: p. 1-10.
10. Pierre-Kahn, V., et al., Ophthalmologic findings in suspected child abuse victims with subdural hematomas. Ophthalmology, 2003. 110(9): p. 1718-23.
11. Nadarasa, J., et al., Update on injury mechanisms in abusive head trauma--shaken baby syndrome. Pediatr Radiol, 2014. 44 Suppl 4: p. S565-70.
12. Kanukollu, V.M. and S.S. Ahmad, Retinal Hemorrhage, in StatPearls. 2022, StatPearls Publishing

Copyright © 2022, StatPearls Publishing LLC.: Treasure Island (FL).
13. Duhaime, A.C., et al., The shaken baby syndrome. A clinical, pathological, and biomechanical study. J Neurosurg, 1987. 66(3): p. 409-15.
14. Greenwald, M.J., et al., Traumatic retinoschisis in battered babies. Ophthalmology, 1986. 93(5): p. 618-25.
15. Mattheij, M., et al., Retinal haemorrhages in a university hospital: not always abusive head injury. Acta Neurol Belg, 2017. 117(2): p. 515-522.
16. Hansen, J.B., et al., Retinal Hemorrhages: Abusive Head Trauma or Not? Pediatr Emerg Care, 2018. 34(9): p. 665-670.
17. Coats, B., et al., Ocular hemorrhages in neonatal porcine eyes from single, rapid rotational events. Invest Ophthalmol Vis Sci, 2010. 51(9): p. 4792-7.
18. Coats, B., et al., Cyclic Head Rotations Produce Modest Brain Injury in Infant Piglets. J Neurotrauma, 2017. 34(1): p. 235-247.
19. Umstead, C., et al., Modeling Hypertension as a Contributor to Retinal Hemorrhaging from Abusive Head Trauma. J Healthc Eng, 2020. 2020: p. 4714927.
20. inc., H.I., MPR Series. 2022: 830 East Arapaho Road. Richardson, TX 75081.
21. van Zandwijk, J.P., et al., Modeling of inflicted head injury by shaking trauma in children: what can we learn? : Part II: A systematic review of mathematical and physical models. Forensic Sci Med Pathol, 2019. 15(3): p. 423-436.
22. K. de Jager, M.v.R., P. Lesire, H. Guillemot, C. Pastor, B. Schnottable, G. Tejera, J. Lepretre, ASSESSING NEW CHILD DUMMIES AND CRITERIA FOR CHILD OCCUPANT PROTECTION IN

FRONTAL IMPACT. EEVC WG12 & WG18 2023: p. 05-0157.
23. Delft, T. Dined. 2020; Available from: https://dined.io.tudelft.nl/en/profiler/introduction.
24. Song, H.H., et al., Exploring the Vitreoretinal Interface: A Key Instigator of Unique Retinal Hemorrhage Patterns in Pediatric Head Trauma. Korean J Ophthalmol, 2022. 36(3): p. 253-263.
25. v, R.P.M., Nabeel & Joseph, Jayaraj & Shah, Malay & Sivaprakasam, Mohanasankar, Measurement of Arterial Young's Elastic Modulus

using ARTSENS Pen. 2018: p. 1-6.

26. Kyllar, M., et al., A porcine model: surgical anatomy of the orbit for maxillofacial surgery. Lab Anim, 2016. 50(2): p. 125-36.
27. Cirovic, S., et al., Mechanistic hypothesis for eye injury in infant shaking : An experimental and computational study. Forensic Sci Med Pathol, 2005. 1(1): p. 53-9.
28. Muni, R.H., et al., Hand-held spectral domain optical coherence tomography finding in shaken-baby syndrome. Retina, 2010. 30(4 Suppl): p. S45-50.
29. Getty, R., Sisson and Grossman's the Anatomy of the Domestic Animals. 5th ed. 1975: Saunders, Philadelphia.
30. Thieme, Atlas of Anatomy, head and Neuroanatomy. 2010.
31. Rho, J.Y., R.B. Ashman, and C.H. Turner, Young's modulus of trabecular and cortical bone material: ultrasonic and microtensile measurements. J Biomech, 1993. 26(2): p. 111-9.
32. Sanchez, I., et al., The parameters of the porcine eyeball. Graefes Arch Clin Exp Ophthalmol, 2011. 249(4): p. 475-82.
33. Meshida, K., et al., Cetacean Orbital Muscles: Anatomy and Function of the Circular Layers. Anat Rec (Hoboken), 2020. 303(7): p. 1792-1811.
34. Zezula-Szpyra, A. and W. Grzegorzewski, Morphology of the dorsal nasal, frontal and facial veins in adult gilts. Folia Morphol (Warsz), 2000. 59(3): p. 179-91.
35. Middleton, S., Porcine ophthalmology. Vet Clin North Am Food Anim Pract, 2010. 26(3): p. 557-72.
36. Power, E.D., et al., Computer modeling of airbag-induced ocular injury in pilots wearing night vision goggles. Aviat Space Environ Med, 2002. 73(10): p. 1000-6.
37. C., R., CRC Handbook of Chemistry and Physics. Weast, Ed. 62 Edition ed. 1981: CRC Press, Boca Raton, FL.
38. Van den Berg, A., The mechanisms of retinal haemorrhage in inflicted head injury by shaking trauma in infants. 2023, TU Delft.

Appendix A

R: Design criteria

The goal of this eye model design is to create four models that represent anatomical aspects differing between a pig and human, to assess the effect of these differences on the pressure in the eye. The anatomical aspects compared in this study are the sideways- (pig) or forward-facing (human) orientation of the eye, and an open (human) or closed orbit (pig).

RA: General criteria

RA.1 *Modular:* The system should be easily made in multiple versions and/or parts for testing.
RA.2 *Safe*: The use of the system should be safe.
RA.3 *Durability*: All parts of the design should be reusable for multiple times to perform the same function every single time.
RA.4 *Production costs:* Low production and material costs are preferred.

RB: The shake simulator:

RB.1 *The shaking frequency:* Repeated rotations with a fixed frequency should be used in this study. The shaking frequencies produced by the shaking simulator should be the same frequencies as attained during shaking experiments. According to Schiks et al. [1] shaking events typically had frequencies between 2.8-6.2 Hz. The shaking frequency should manage the maximum frequency. Thus, the shaking frequency should be 6 Hz.
RB.2 *The shaking duration:* The duration per shake produced by the shaking simulator should be the same duration as attained during shaking experiments. According to van Zandwijk et al. [21] shaking events lasted 3-5 seconds.
RB.3 *Loading cycles*: During the shaking duration, there should be multiple loading cycles.
RB.4 *Repetitive***:** All the kinematics of the shaking simulator should be repetitive.
RB.5 *Head centre-of-gravity (cog) acceleration:* The cog acceleration should be the same cog acceleration as attained during shaking experiments. According to Schiks et al. [1] the mean cog acceleration is 155 m/s^2 of the x-direction.
RB.6 *Angular velocity:* The angular velocity should be the same angular velocity as attained during shaking experiments. According to Schiks et al. [1] the mean angular velocity is 43 rad/s.
RB.7 *Movement*: The simulator should perform a combination of a translational and rotational movement, comparable to a shaking event. Furthermore, the eye model should perform a sagittal rotation during the experiment. The magnitude of the movement of the COG of the head is according to Schiks et al. [1] circa 300 mm horizontal and 25 mm vertical (see Figure 19).
RB.8 *Attachment*: At least two standard eye models should be able to be attachable to the shake simulator. Furthermore, the eye models should be able to be fastened in such a way that they do not get stuck during rotation.
RB.9 *Monitor of movements:* Movements produced by the shaking simulator should be measured during the experiment.

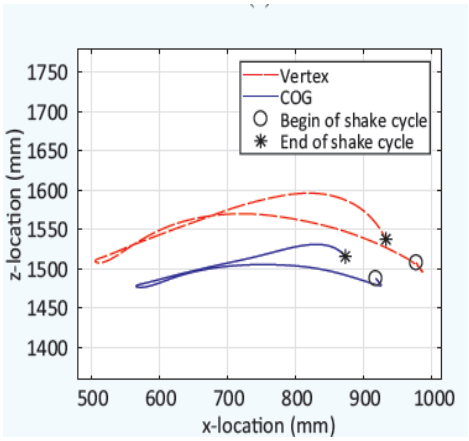

Figure 19: One of the shaking pattern variations encountered during the study of Schiks et al. [1]. Coordinates are expressed in the inertial reference frame.

RB.10 *Strength*: The weight of the eye model should not slow down the frequency of the shaking simulator. The weight of the eye model expected to be the same as the weight of the neck and head of a Q0 dummy and that is 1.1 kg [22].
RB.11 *Arm length*: The arm length of the shake simulator should be like the forearm length of an adult and the armpit height to the neck height together. According to Dined [23], the mean forearm length is 290 mm. The length between the armpit height and the neck of an infant is circa 100 mm. Thus, the total arm length of the shake simulator should be circa 390 mm.

RC: The standard eye model:

RC.1 *Eyeball***:** The shape of the eyeball should be a spherical shape with a diameter of 24 mm and a wall thickness of the eye of 0.8 mm, comparable to the infant's eye. The length of arteries should be ± 28 mm [24].
RC.2 *Representative structure for the function of arteries:* there should be a fluid supply and drainage to the eyeball from the fluid reservoir.
RB.3 *Representative structure for the function of arteries*: The eye model should be able to bring under physiological pressure inside the eyeball.

RB.4 *Representative structure for the function of arteries*: The mean young's modulus of artery wall is 262.8 ± 99 kPa [25].
RB.5 *Reservoir*: The eye model should consist of a fluid reservoir. Both pig and human consist of a reservoir (sinus cavernous) which receives blood from the vein of the retina [26].
RB.6 *Representative structure for the muscles around the eye:* eye model should be able to keep the eyeball in the eye socket. The representative structure for the muscles should be the same as the structure of the muscles of an infant. Cirovic et al. [27] assumed that the tetanic isometric force is 1 N.
RB.7 *Material parameters***:** The material parameters of the eye model needed to be comparable with a real eyeball of an infant. According to Song et al. [24] is the young's modulus of the retina 20 kPa and the Poisson's ratio of the retina 0.49. Furthermore, the material should be moulded and flexible because it should be able to be laid in different shapes during the experiments.
RB.8 *Measure the pressure*: During the shaking experiments, pressure should be measured inside the eyeball. Around the connection point between the eyeball and the artery, the optic disc is located, and this is where most bleeding is found in IHI-ST [28].
RB.9 *Attachment***:** The eye model should be able to be attached to the shaking simulator.

RD: Test modules:
Below the design criteria of the test modules that will be used to test the different anatomical aspects of the eye between a pig and human and to answer the mean question. The test module "eye orientation" is required to test the differences between stress inside the eye between the orientation of the eye of a pig and human. The test module "orbit" is required to test the differences in stress inside the eye between a closed and open orbit during shaking.

RD.A: Test module: "eye orientation":
RD.A2 *Orientation*: The eyes of a human are located medially around 0°. The eyes of a pig are located lateral around 35°. Thus, the visual axes of the pig compared to the human is 35° outwards. Besides that, the location of the reservoir is the same in human and pig anatomy [29]. The reservoir should be used as a 0 degrees point. One eye model should deviate 0 degrees from the reservoir. One eye model should deviate 35 degrees from the reservoir.
RD.A3 *Attachment***:** The test module "eye orientation" should be attached to the eye model and the test module "orbit".

RD.B: Test module: "orbit":
RD.B1 *Orbital height and width***:** The mean orbital height of a pig is 5.3 cm and mean orbital width is 3.41 cm [26]. The mean orbital height is 4 cm and mean orbital width is 3.5 cm of a human (not infant) [30]. One component should simulate the anatomical aspects of a pig and one for human.
RD.B2 *Orbit orientation:* The pig lacks bones at its caudolateral aspect in that way the orbit of a pig is open [26]. Thus, one orbit should lack of bone at the caudolateral side. One orbit should be comparable with a closed orbit.
RD.B3 *Material parameters*: The material should be strong and stiff, which is comparable to the hardness of a bone. The Young's modulus of cortical bone is around 18.6 GPa [31].
RD.B4 *Attachment***:** The test module "orbit" should be attached to the eye model and the test module "eye orientation".
RD.B5 *(De)mountable***:** The orbit should be (de)mountable and during that, it should not damage the eye model.

Appendix B

Overview of the anatomical aspects of the eye

To investigate the anatomical differences of the eye and surrounding structures of the human and pig a table was made with all the anatomical aspects of the eyes. The section “anatomical aspects of the eye” describes all the anatomical aspects of the eye of the pig and human. The sections “Pig” and “Human” describes whether the species contains the anatomical aspect and in what way. The section “Potentially relevant differences” specifies which differences in the anatomical aspect could be the most potentially relevant differences for RH in a pig and human eye during violent shaking. The section “Contribution to RH” describes whether the differences in anatomy expected to contribute to RH in IHI-ST. The section “Hypotheses” describes in what way it could contribute to RH. The section “Feasibility” is divided by three colours. The green colour indicates that there is a reason to expect an effect on RH and it is feasible to test the in this study. The orange colour indicates that there is a reason to expect an effect on RH, but it is not feasible to test this in this study. The reason for this is also described. The red colour indicates that there is no reason to expect an effect on RH. In addition to all these aspects, there are more anatomical aspects in the eye. However, this study was able to conclude from literature what the most striking differences were between pigs and humans and whether they would have an expected difference for RH in IHI-ST.

Anatomical aspects of the eye	Pig	Human	Potentially relevant differences	Contribution to RH	Hypotheses	Feasibility
Blood drainage of the retina	Posterior ciliary vein that enters the eyeball at the periphery of the optic disc [32]	Central retinal vein inside the optic nerve	The posterior ciliary vein enters the optic nerve at the optic disc and is not inside the optic nerve and differs in this way from the human.	Expected	More pressure is put on the nerve during shaking. Because the posterior ciliary vein is not inside the optic nerve, there will be less pressure on the vein during shaking. This may prevent bleeding in a pig's retina.	Measuring blood flow in a physical model is too complex or should be very simplified
Blood supply of the retina	Chorioretinal artery that enters the eyeball at the periphery of the optic disc [32]	Central retinal artery	More pressure is put on the nerve during shaking, but the chorioretinal artery enters the optic nerve at the optic disc and is not inside the optic nerve and differs in this way from the human.	Expected	More pressure is put on the nerve during shaking. Because the chorioretinal artery is not inside the optic nerve, there will be less pressure on the artery during shaking. This may prevent bleeding in a pig's retina.	Measuring blood flow in a physical model is too complex or should be very simplified

Extraocular muscles	Six muscles + an extra cone shaped muscle that surround the optic nerve and the blood vessels: m. retractor bulbi [32, 33]	Six muscles around the eye	M. Retractor Bulbi surround the optic nerve and the blood vessels of the pig.	Expected	M. Retractor bulbi surround the blood vessels which may protect them during shaking. This may prevent RH in pigs.	
Extraocular muscles	Six muscles + an extra cone shaped muscle that surround the optic nerve and the blood vessels: M. Retractor Bulbi [32, 33]	Six muscles around the eye	M. Retractor Bulbi of the pig tends to retract the eyeball in the orbit	Expected	The forward inertia in the pig may be less than in humans due to the retraction of the M. Retractor Bulbi during shaking	
Position of the eye	The eyes are orientated 35 degrees outward compared to human [29].	At the front of the face	The position of the eyes of pigs and humans	Expected	A decrease in force being applied along the optic nerve during sagittal head rotation and increase in force along the optic nerve during coronal head rotation in the eyes of the pig. This may prevent RH in pigs.	
Closure of the orbit	Open orbit, a strong fibrous ligament from the frontal bone to the zygomatic bone (lacks bones at its caudolateral aspect) [17]	Closed orbit (eyeball surrounded with bones) [17]	The strong fibrous ligament compared to the bone at the caudolateral side of the pig.	Expected	The stiffness of a ligament is less than a bone. This may have a dampening effect on the eye during shaking and in that way prevents RH in pigs.	
Sinus cavernous	Situated at the base of the brain and protected by surrounded bone. Receives blood from the retina [34]	Situated at the base of the brain and protected by surrounded bone. Receives blood from the retina	No relevant differences. Both are located on the same positions, and both perform the same function	Expected	No reason to expect an effect on RH	
Strong attachment points between the vitreous and retina	Situated at the vitreous base [17]	Situated at the vitreous base, optic nerve head, macula, and along major retinal vessels [17]	The difference in the place and the amount of attachment points between pigs and humans	Expected	More attachment points in humans can give more tension in the retina. However, these increase in tension arises after the blood vessels are ruptured. In that way, it is a result of the bleeding instead of the cause of the bleeding.	Because it is not expected to be the main cause of the difference in RH between a pig and a human, it will not be tested in this study

Eye lids	Three eye lids. The third eye lid of the pig protect and moisten the eye while maintaining vision. It is connected to the M. Retractor Bulbi [27]	Two eye lids [27]	Th third eye lid of the pig and its connection with the M. Retractor Bulbi.	Only minor effect expected	The third eye lid of the pig could give a minor effect on RH in a pig because the third eye lid can hold the eyeball in place during shaking. However, the strength of the M. Retractor Bulbi may have a greater role	
Macula	No, but there is an area with a high density of cones, area central in the back which is comparable to the macula of the human [17]	Yes, at the central in the back [17]	No relevant differences. Both are located on the same positions, and both perform the same function	Not expected	No reason to expect an effect on RH	
Annulus of Zinn, the tendinous origin of the extraocular muscles	No, muscles are direct attached to the bone (orbit) [17]	Yes, a fibrous ring that surround the optic canal and part of the superior orbital fissure at the orbital apex and connects the muscles with the orbit [17]	Annulus of Zinn, the fibrous ring in the human's orbit	Not expected	The annulus of Zinn, could protect the optic canal and in the that way the central retinal vein and artery	
Annulus of Zinn, the tendinous origin of the extraocular muscles	No, extraocular muscles are direct attached to the bone (orbit) [17]	Yes, a fibrous ring that surround the optic canal and part of the superior orbital fissure at the orbital apex and connects the extraocular muscles with the orbit [17]	The extraocular muscles are direct attached to the bone inside the orbit of a pig	Only minor effect expected	The attachment of the muscles to the bone could be more rigid than the ligaments between the muscles and the bone in the human	

Cornea	Yes, transparent in the front of the eyeball but two times thicker than a human	Yes, transparent in the front of the eyeball	The cornea of a pig is two times thicker	Only minor effect expected	The thicker cornea can give more negative pressure on the eye during shaking. However, this effect is minor compared to other differences in anatomical aspects between human and pig.	
Fovea	No, but inside the macula exists a region that is more sensitive to colour and high acuity vision, like the fovea of humans [35]	Yes, inside the macula and is responsible for central vision	No fovea inside the macula of the eye of the pig.	Not expected	The only function of the fovea is high-acuity vision. In that way the vision of a human is better but no reason to expect an effect on RH	
Ophthalmic vein	Yes, arises from the small branches of the facial and supraorbital veins [35]	Yes, arises from the small branches of the facial and supraorbital veins	No relevant differences. Both are located on the same positions, and both perform the same function	Not expected	No reason to expect an effect on RH	
Optic nerve	Yes, but oval. Located from the back of the eyeball (retina) to the brain [35]	Yes, located from the back of the eyeball (retina) to the brain	No relevant differences. Both are located on the same positions, and both perform the same function	Not expected	No reason to expect an effect on RH	
Layers of the retina	10 layers [35]	10 layers	No relevant differences. Both are located on the same positions, and both perform the same function	Not expected	No reason to expect an effect on RH	

Fat tissue properties	Data not available in literature	Data adult [36]. No infant data available	Stiffer fat tissue: high impact effects on the retina. Less stiff fat tissue allows more deformation and more traction on the retina.	Only minor effect expected	Th differences in RH between a pig and a human may be due to differences in fat properties.	More data is needed from pigs and infants, but this is not feasible in this study
Intraocular pressure	Adult pig: 10 to 21 mmHg [35], young pig: not available in literature	Adults: 12-21 mmHg, Infants: 10 to 15 mmHg	Even though data from young pigs is not available, no relevant differences are expected because the data from adults is similar	Not expected	No reason to expect an effect on RH	
Blood pressure	Adult pig: 86-123 mmHg [35], young pig: not available in literature	Adults: 80-120 mmHg, Infant 41-64 mmHg	Even though data from young pigs is not available, no relevant differences are expected because the data from adults is similar	Not expected	No reason to expect an effect on RH	
Tissue properties (retina) e.g., retinal detachment	Data available in Table 1 [35]	Data adult [36]. No infant data available	Stiffer material (e.g., blood vessels and retina): high impact effects on the retina. Less stiff material allows more deformation and more traction on the retina.	Only minor effect expected	Th differences in RH between a pig and a human may be due to differences in properties.	More data is needed from young pigs and infants, but this is not feasible in this study

Appendix C

Concepts: Designing

Concepts: Shake simulator

Two different concepts can mimic the motion of a shake event of an infant. Being able to simulate a shaking motion as closely as possible is important because the eye model should be connected to the shake simulator. The eye model should be able to experience the comparable speeds and distances to test the difference in pressure in the eyes.

Concept 1: The locomotive

The locomotive is a concept that moves the same way as the wheels of a locomotive. The driving wheel is connected to a crank and a connecting rod. When the driving wheel completes a full rotation, the connected crank moves back and forth. In this concept, the connected crank is connected to two plates and a rod which moves back and forth by rotating the driving wheel. The driving wheel is connected to an electromotor (See Figure 20).

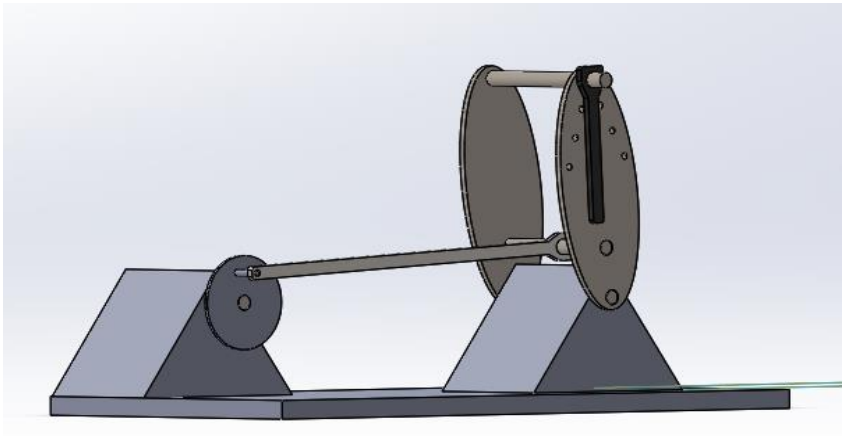

Figure 20: The SolidWorks version of the concept: locomotive. The wheel is connected to a crank and rod. The crank is connected to the oval plates. When the wheel is driving, the crank moves back and forth. The upper rod is connected to a "spring" which slower the movement if pins are connected to the plate.

The frequency of the shake simulator is one of the design criteria (RB.1). The shake simulator should rotate with a frequency of 6 Hz (360 rotation per minute). An electromotor should be used to rotate the shake simulator with a frequency of 6 Hz. The electromotor is connected to a wheel which is connected to a crank and a connecting rod. The connecting the rod is connected to the arms of the shake simulator. The arms of the shake simulator are plates with varied sizes of holes. The holes are connected to rods which ensures that the arms are strong enough for the speeds at which they will move. Furthermore, the upper rod is connected to a "spring" that cases the slower movement of the upper rod (see Figure 20). The slower movement indicates the stiffness of an infant's neck which is one of the design criteria (RB.12). The holes located with different length which provided a variable neck stiffness. The advantages of the locomotive are that it can be assembled quite inexpensively. An electric motor costs around one hundred euros. A micro controller is located at the TU Delft. Furthermore, the rotating gear ensures smooth movement.

Concept 2: the pneumatic cylinder

The pneumatic cylinder is a concept that induces linear movement. It is pre-moved by a compressor attached to a horizontal beam, which is directly connected to the ground. Here, the linear movement of this beam will mimic the rocking motion of a child. Due to the variable nature of the rocking movements, the stroke length of the pneumatic cylinder must be considered. The minimum stroke length is 100 mm, and the maximum stroke length is 300 mm. The advantage of this concept is that it is easier to implement. However, the drawback is that the pneumatic cylinder needs to be connected to a compressor, and this may not be feasible in every location. Additionally, it results in a jerky movement, failing to meet the specified requirements. Moreover, it is also quite expensive.

Concept: standard eyeball and eye modules

Several steps were taken to create two eye models and four different orbits of the eye:

Eye models:

Eye: The eyes of the eye model should be connected to the tubes (See Figure 21). If the tubes and the eyeball are connected afterwards, it may break during the experiment and lots of energy can be lost inside the connection point instead of the eyeball itself. Because of this, it should consist of one part and thus be moulded. The material that is used for this purpose is 25 % silicone without hardener. It can be created in various densities, allowing the eyeball to have a different density than the tube which is required to meet the requirement RB.7. However, combining two types of silicone with different densities is not feasible within this eye model. The eye model is too small to accommodate the use of two different silicones. The air in the mould needs to escape to prevent the formation of air bubbles. This necessitates another compromise on the different densities. Therefore, it was decided to use the 25% silicone. See appendix K for the drawing of the mould of the eye model.

*Tube*s: A hollow form is cast to create tubes that are similar in thickness to a vein. The hollow shape is formed by inserting a rod that can be removed after filling the mould with silicon. To closely resemble the veins of the eye, an attempt was made to use two tubes, as described in the requirements. Unfortunately, this proved unfeasible as the required thickness of the veins could not be achieved. Consequently, a decision had to be made to opt for a single large tube instead of two narrow ones. To make the tubes as comparable as possible to a vein, a compromise had to be made. The same material (silicon 25%) used for the eyes was also used to cast the tubes (See Figure 21).

Micro pressure sensor: The pressure sensor must be accurate enough to measure the smallest variations in pressure. Furthermore, the micro pressure sensor should not be too heavy, as this could impact the pressure in the eye during shaking and potentially yield inaccurate readings. Additionally, the pressure sensor must not be too large, as it might not fit within the confines of the eye. In this context, the Honeywell micro pressure sensors come closest to meeting the requirements [20]. The sensor is compact, measuring only 5 mm x 5 mm, making it suitable for placement within the eye. Additionally, it can measure pressure within a range of 6 to 250 kPa. Furthermore, it can detect pressure differentials in liquids because it is waterproof.

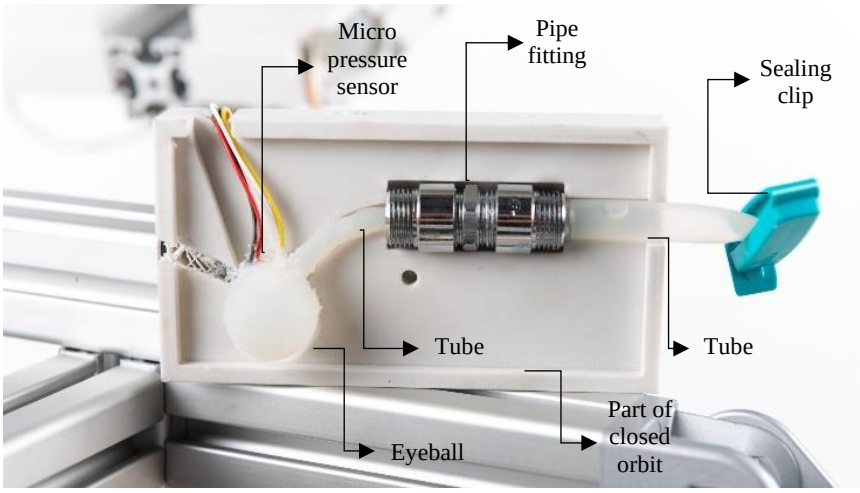

Figure 21: The eye model connected to one part of the orbit. On the left side, the eyeball is connected to the micro pressure sensor and connected to a tube. The left tube and right tube relate to a Sanivesk Straight Thread Adapter. The eye model is sealed with a sealing clip on the right sight.

Reservoir: The reservoir is made of a silicon tube with a length of 26,5 mm, an inner diameter of 8 mm, and a thickness of 2 mm. The reservoir is attached to the custom-made eyeball with Sanivesk Straight Thread Adapter 3/4"Mx1/2"F and Sanivesk Straight Thread 1/2"Mx1/2"M Chrome. The end of the custom-made reservoir is sealed with a sealing clip (see Figure 21).

Water pressure inside the eyeball: To ensure that the water pressure in both eyes is equal, the eyeballs are made the same and both sealing at 12 mm with the sealing clip (see figure 20). The eyeballs are filled with 12 ml of water using a syringe.

Orbit:

The goal of this eye model design is to create four models that represent anatomical aspects differing between a pig and human, to assess the effect of these differences on the pressure in the eye. The anatomical aspects compared in this study are the sideways- (pig) or forward-facing (human) orientation of the eye, and an open (human) or closed orbit (pig) (See Figure 22). The optic axes of human eyes are oriented medially at approximately 0° relative to the sagittal axis originating from the lateral geniculate nucleus. The optic axes of the eyes of the pig are orientated around 35 degrees relative to the sagittal axis originating from the lateral geniculate nucleus [29]. Therefore, we development of four different phantom orbits: infant eye model open which there lacks bone around the eye (Ø.O), infant eye model closed which the eye is fully surrounded by bone (Ø.C), pig eye model open which there lacks bone around the caudolateral side of the eye (35.O), and pig eye model closed which the eye is fully surrounded by bone (35.C).

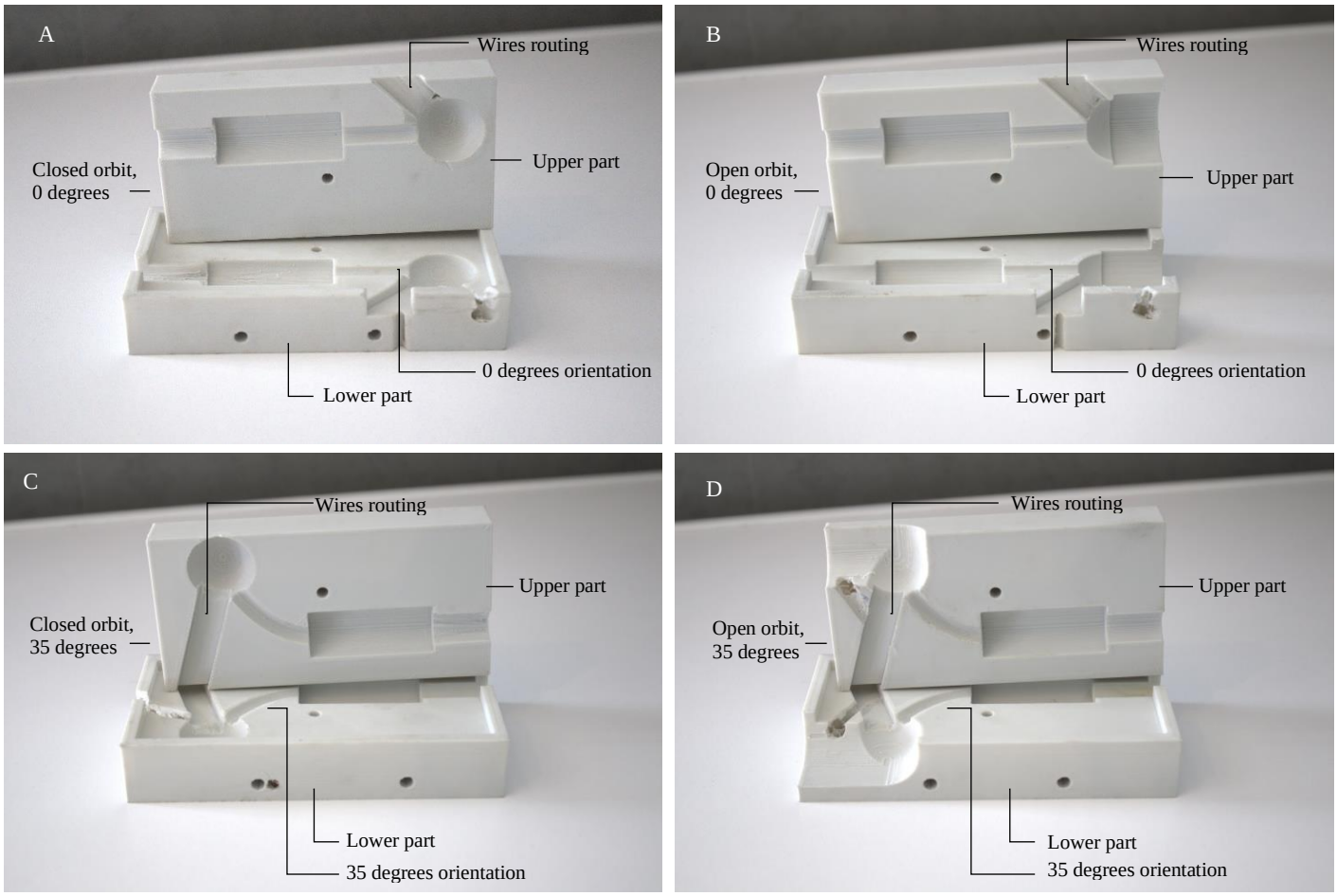

Figure 22: Part A: shows the closed orbit in combination with the 0 degrees orientation (which represents the human orbit). Part B: Shows the open orbit in combination with the 0 degrees orientation (control group). Part C: shows the closed orbit in combination with the 35 degrees orientation (control group). Part D: shows the open orbit in combination with the 35 degrees orientation (which represents the orbit of the pig)

Conceptualization: The Shake simulator

The locomotive shake simulator: Due to the advantages of the locomotive shake simulator, it was chosen to further develop this idea. Additionally, there is already an electric motor available at the TU Delft, which allows for cost savings in this regard. Before determining whether the electromotor is suitable for the Shake simulator, it is important to calculate the minimum required power to move the shake simulator, to calculate the acceleration of the eye model and to calculate the torque. The concept of the shake simulator is first elaborated in SolidWorks to gather this data. The wheel size of the wheel connected to electromotor is important to calculate. The total length of the plate is 390 mm, the same size as mentioned in RB.11. The total shake movement from the rod where the eye model should be connected is 300 mm as mentioned in RB.11. The connected rod is connected at one/third of the plate and the distance of the movement is in that way 100 mm. The connection point of the wheel should be the same diameter as the distance of the movement at one/third, 100 mm.

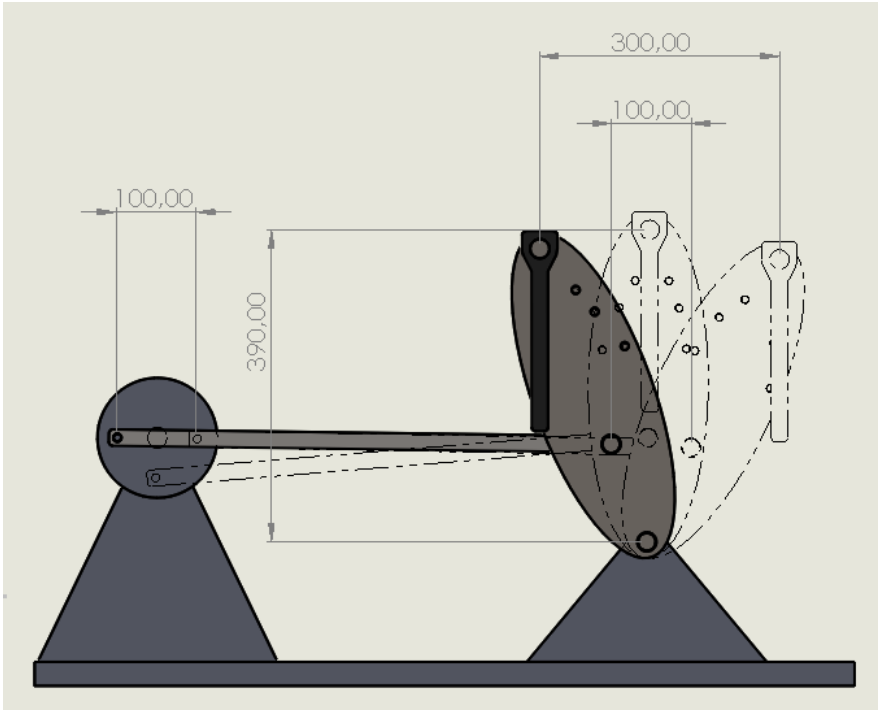

Figure 23: The conceptualization of the shake simulator.

In a static position (the middle position of Figure 23) the connected rod should connect to the wheel at the top or the bottom. In the left position the connected rod should be connected to the wheel at the left side and in the right position at the right side. Furthermore, at the left and right position the connected rod should be horizontal otherwise the vertical distance differs during a full circle.

The required power of the shake simulator

A schematic overview of the required power and acceleration is shown in Figure 24 and Figure 25 and Equations below:

$$M=F\times d$$

$F(PE)$ = Gravitational force of the plates, rods, and the eye model

$F(PE)$= 5 kg×9.81 m/s2=49.05 N

M = 49.05 N×0.26 m

Power (ideal) = (Torque×RPM)/9554

Power (ideal)=(13×360)9554=0.5 kW

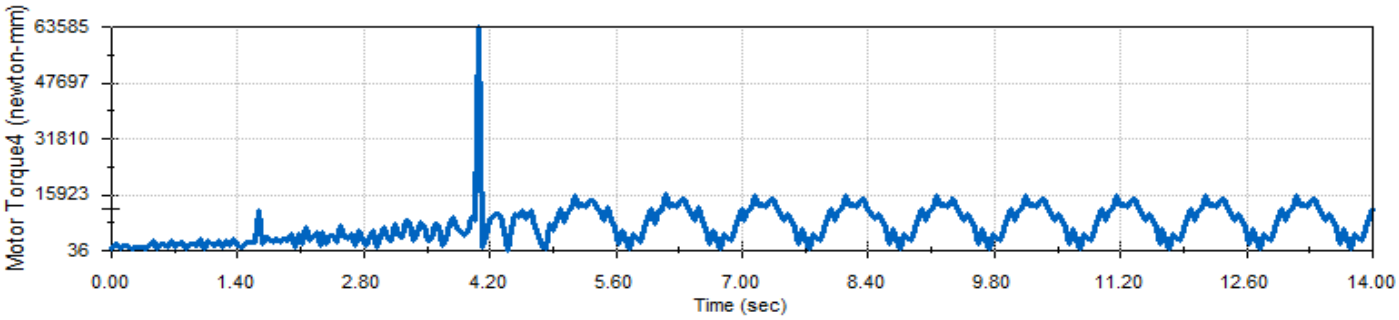

Figure 24: Stall motor torque in N/mm of the motor used for the shake simulator in SolidWorks. After 4.2 seconds the maximum torque is around 15.923 n mm.

Acceleration of the eye model

The initial and final speed divided by the time interval is given as follows:

Angular velocity=Revolutions per second×2πtime interval

Given that there are six revolutions per second.

Angular velocity=6 revolutions/second×2π
Angular velocity=12π radians/second

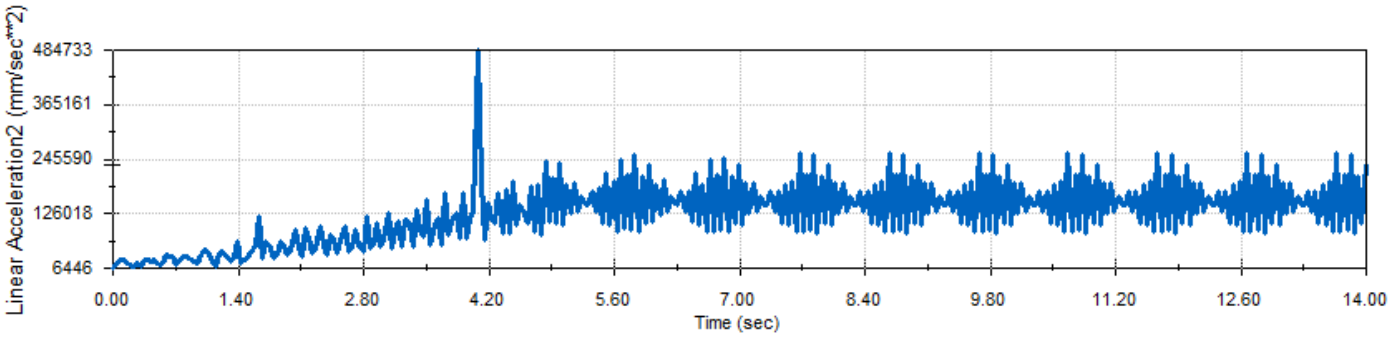

Figure 25: Linear acceleration of the arm of the shake simulator according to SolidWorks.

Improving the manufacturing of the shake simulator

Due to the significant forces exerted on the shake simulator, 3D printing of the plates is not feasible. The materials typically used for 3D printing are not strong enough. However, the products from Item are suitable for this purpose. As a result, a new setup has been created utilizing Item products (see Figure 26). Additionally, Item bearings have been employed to provide extra reinforcement to the model. By increasing the weight of the wheel, it is utilized as a flywheel. Incorporating this into the concept reduces the maximum torque.

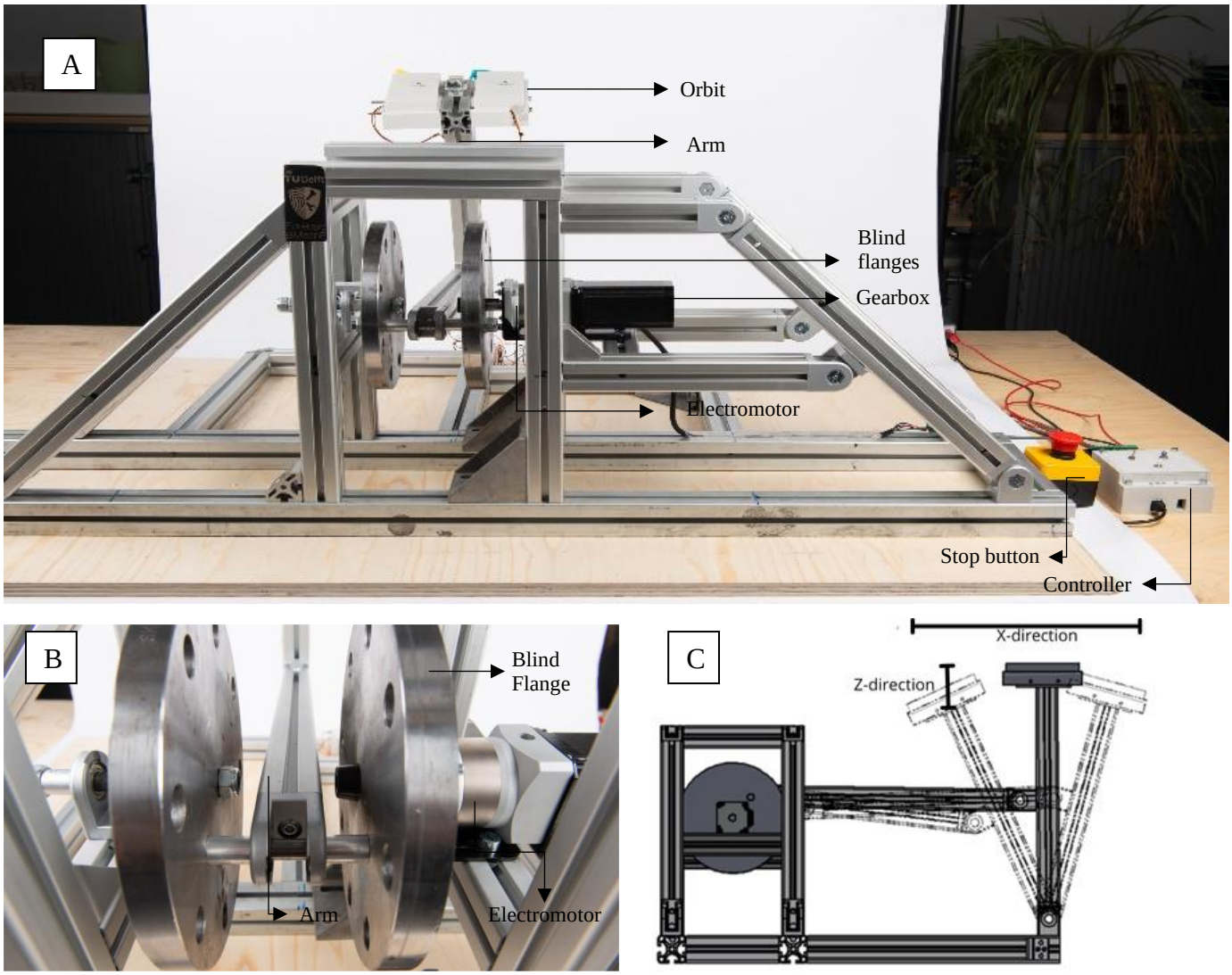

Figure 26: A: The experimental setup within the two blind flanges, two orbits, electromotor and gearbox, controller and stop button. The figure shows the two flanges in combination with the arm of the shake simulator. Part B: Shows the zoom-in version of the experimental setup. The blind flanges are shown in combination with the arm and the electromotor. Part C: this figure illustrates the side view of the experimental setup and shows how the movement of the shake simulator occurs. Additionally, it displays the x- and z-directions of the accelerometer.

Figure 26 shows the final version of the custom-made shake simulator. The modifications in this latest version of the shake simulator result in a reduction of the maximum torque. The maximum stall torque of the motor is now, on average, 9000 Nmm (See Figure 24). Additionally, the Stepper motor Nema 23; 57HS115A44008 (which is available at the TU Delft) does not meet the required specifications. This motor consists of a holding torque of 3.5 Nm and 1500 RPM. Therefore, a Planetary Gearbox with a gear ratio of 5:1 ratio has been chosen to achieve the necessary torque. However, this may compromise the required frequency of 6 Hz.

Appendix D

Materials used during the experiment

Table 6: The materials used for the experimental setup.

Part/Material	Part/material type	Part/Material brand	Manufacturer location	Specifications	Amount
Shake simulator	Custom-made in-house	-	-	Appendix C	1
Gearbox	Planetary Gearbox with a gear ratio of 5:1, EG23-G5-D8	Stepper online	-	15 arc-min backlash	1
Electromotor	Stepper motor Nema23; 57HS115A44008	Jingbo Motor Store	China	3.5 Nm., 115mm 4A as diameter 8.0mm, 1.8 degrees	1
Micro Step Driver	TB660	Bh-Eleven	Ouyzgia	2 Micro Step Pulse/rev, 3.5 A	1
Blind Flange	Blind Flange, ND16, DN100,	Wildkamp	-	Diameter 180 mm, 220 x 20 mm, steel.	2
Infant eye model open	Custom-made in-house	-	-	Appendix C	1
Infant eye model closed	Custom-made in-house	-	-	Appendix C	1
Pig eye model open	Custom-made in-house	-	-	Appendix C	1
Pig eye model closed	Custom-made in-house	-	-	Appendix C	1
Micro Pressure Sensor	MPRLS0025PA00001A	Honeywell, Sparkfun	United States	6 to 250 kPa, I2C, address 0x18 and I2C, address 0x28	2
Pipe fitting	Straight Thread Adapter and Straight Thread	Sanivesk,Gamma	Netherlands	3/4"M x 1/2"F, 1/2"M x 1/2"M Chrome	2
Sealing clip	Sealing clips	Ikea	Netherlands	Plastic	2
Tube	SB501095	Slangenboer	Netherlands	Silicon and Rubber, inner diameter 8 mm and outer diameter 12 mm	
Stopwatch	CG-501	CatigaElectronics	Hong Kong	-	1
Accelerometer	GY-61 DXL 335	Analog Devices	-	X and Z acceleration	1
Stop button	Red Sign	Heschen	China	660 V, 10 A	1
Custom-made controller	Custom-made in-house	-	-	Appendix C	1

Appendix E

Arduino script for Stepper motor

```
// Includes
// Define pins variables
int pinStep = 6; // PUL pin to stepper motor controller
int pinDir = 5; // DIR pin to stepper motor controller
/*int pinOnOff = 7; // pin to stepper motor on/off port. 0 = off, 1 = on
int pinPotSpeed = A0; // pin from potentiometer
int pinButRunA = 8; // pin from button for starting motor sequence in auto mode
int pinSwitchAM = 4; // pin from auto/manual selector switch
int pinLED_g = 13; // pin to green LED -> motor speed should be zero
int pinLED_y = 12; // pin to yellow LED -> ramp-up or ramp-down speed is active
int pinLED_r = 11; // pin to red LED -> high speed plateau is active
int pinLED_o = 7; // pin to orange LED -> Auto mode is activated
int pinLED_b = 10; // pin to blue LED -> Manual mode is activated


// Define process control flags
int flagAuto = 0; // 1 = use pdTarget for speed and ignore potmeter;, 0 = use potmeter for
speed;
int flagRunA = 0; // 1 = pinButRUN was pressed, run ramp-up -- platform -- ramp-down sequence
int flagRunM = 0; // In manual mode, 0 = motor off, 1 = motor enabled, speed controlled with
potmeter

// Define target speed and direction variables for stepper motor control
int dirStep =  0; // direction in which the motor must turn via input on pinDir 0 = Right
float tStep_Slowest = 1000; // Max steptime in us for stepper (min speed)
float tStep_Fastest = 20; // Min steptime for steppr (max speed) -- UNUSED

// Define stepper motor control variables
unsigned long tLoopStart_ms = 0; // loop start time in milliseconds
unsigned long tCurrent_ms = 0; // current time in milliseconds

float tStep_P = tStep_Slowest; // step time (=half step period) taken from pot meter. Default
is put at slowest for safety.
float tStep_A = tStep_Slowest; // auto set step time, default slowest, to send to motor
float tStep_M = tStep_Slowest; // manually set step time, default slowest, to send to motor

float tStep_A_target = 150; // step time for auto target target (and maximum) speed
float tStep_M_target = 20; // step time for manual (and pot meter) target (and maximum) speed

float tRampUp = 5*1000; // ramp-up time in milliseconds
float tFlat = 5*1000; // plateau time in milliseconds
float tRampDown = 5*1000; // ramp-down time in milliseconds

void setup() {
  // put your setup code here, to run once:
  pinMode(pinStep, OUTPUT);
  pinMode(pinDir, OUTPUT);
```

```
  /*pinMode(pinOnOff, OUTPUT);*/
  pinMode(pinLED_g, OUTPUT);
  pinMode(pinLED_y, OUTPUT);
  pinMode(pinLED_r, OUTPUT);
  pinMode(pinLED_o, OUTPUT);
  pinMode(pinLED_b, OUTPUT);
  pinMode(pinButRunA, INPUT);
  /*pinMode(pinButRunM, INPUT);*/
  pinMode(pinSwitchAM, INPUT);
  // Make sure motor is off at start of program
 /* digitalWrite(pinOnOff, 0);// turn off motor*/

}

void loop() {
  // Main code, to run repeatedly:
  // ================== LOOP INITIALIZATION SECTION)
  /*digitalWrite(pinOnOff, 0);// turn off motor*/

  // Get initialization parameters for this loop
  tLoopStart_ms = millis();
  flagAuto = digitalRead(pinSwitchAM); // make sure it's HIGH when switch is in auto mode
  flagRunA = digitalRead(pinButRunA); //
 tStep_P  =  map((analogRead(pinPotSpeed)),0,1023,tStep_M_target,  tStep_Slowest);  //  Get
potmeter value and map to range between slowest and target tStep

  // Switch LEDs ON; G
  switch_LEDs(1,0,0); // Set LEDs green, yellow, red to 0=off or 1=on

  // ==========================================
  // ============ AUTO MODE SECTION ============
  // If in auto mode, run sequence if ButRunA is pressed
  if ((flagAuto == 1) && (flagRunA == 1)){
    // Initiate motor (turn on and set direction
    digitalWrite(pinDir, dirStep); // set direction
    /*digitalWrite(pinOnOff, 1); // turn on motor*/

    // ------------------------------------
    // ---------- RAMP-UP -----------------
    // Perform ramp-up sequence
    // Switch LEDs ON; G, Y
    switch_LEDs(1,1,0); // Set LEDs green, yellow, red to 0=off or 1=on

    // RAMPUP CODE
    tCurrent_ms = millis();
    if (tCurrent_ms > tRampUp){
      tStep_A = tStep_A_target;
      digitalWrite(pinStep, LOW);
      delayMicroseconds(tStep_A);
      digitalWrite(pinStep, HIGH);
```

```
  delayMicroseconds(tStep_A);}

else{
  tStep_A= tStep_Slowest - (tStep_Slowest-tStep_A_target)*tCurrent_ms/tRampUp;

  digitalWrite(pinStep, LOW);
  delayMicroseconds(tStep_A);
  digitalWrite(pinStep, HIGH);
  delayMicroseconds(tStep_A);}


switch_LEDs(1,1,1);
// ---------------------------------------
// ---------- FLAT ----------------------
// Plateau period in which the motor runs at a constant speed
// Switch LEDs on; G, Y, R
 // Set LEDs green, yellow, red to 0=off or 1=on
// Keep speed steady for set period (or number of steps)
tCurrent_ms = millis();
tLoopStart_ms = millis();
while (tCurrent_ms - tLoopStart_ms < tFlat){
 // Run at potmeter speed until tFlat has passed
  digitalWrite(pinStep, LOW);
  delayMicroseconds(tStep_A);
  digitalWrite(pinStep, HIGH);
  delayMicroseconds(tStep_A);

}

// ---------------------------------------
// ---------- RAMP-DOWN -----------------
// Switch LEDs ON; G, Y
switch_LEDs(1,1,0); // Set LEDs green, yellow, red to 0=off or 1=on
// Perform ramp-down sequence

// ... RAMPDOWN CODE HERE
if (tCurrent_ms-tLoopStart_ms > tFlat){
  tStep_A= tStep_A_target - (tStep_A_target-tStep_Slowest)*(tLoopStart_ms)/tRampDown;
  digitalWrite(pinStep, LOW);
  delayMicroseconds(tStep_A);
  digitalWrite(pinStep, HIGH);
  delayMicroseconds(tStep_A);}

else {
  tStep_A = tStep_Slowest;

  digitalWrite(pinStep, LOW);
  delayMicroseconds(tStep_A);
  digitalWrite(pinStep, HIGH);
  delayMicroseconds(tStep_A);
```

```
    }

    // Turn off motor
    /*digitalWrite(pinOnOff, 0); // turn off motor */
    // Switch LEDs on; G
    switch_LEDs(1,0,0); // Set LEDs green, yellow, red to 0=off or 1=on
  }

  // ========================================
  // ============ MANUAL MODE SECTION =========
  // If in manual mode, run motor at potmeter speed IF ButRunM is pressed
  if ((flagAuto == 0) && (flagRunA == 1)){
    // If the manual run button is pressed, run at potmeter speed
    // Switch LEDs ON; GREEN, ORANGE, RED because system is armed
    switch_LEDs(1,1,1); // Set LEDs green, yellow, red to 0=off or 1=on ;
    // Initiate motor (turn on and set direction)
    digitalWrite(pinDir, dirStep); // set direction
    /*digitalWrite(pinOnOff, 1); // turn on motor*/
    while (flagRunA == 1){

      tStep_M = map((analogRead(pinPotSpeed)),0,1023,tStep_M_target, tStep_Slowest); // Get potmeter value and map to range between slowest and target tStep

      // Run at potmeter speed
      digitalWrite(pinStep, LOW);
      delayMicroseconds(tStep_M);
      digitalWrite(pinStep, HIGH);
      delayMicroseconds(tStep_M);
      flagRunA = digitalRead(pinButRunA); // this way the motor will run at potmeter speed if SwitchAM is set to manual
    }
    // Once flagRunM becomes 0, end up here and disable the motor
    // Switch LEDs on; GREEN
    switch_LEDs(1,0,0); // Set LEDs green, yellow, red to 0=off or 1=on
  }
} // end of void Loop



void switch_LEDs(int bg, int by, int br) {
      // Switch LEDs, 1 = on 0 = off
      // Only LEDs g, y and r are switched by command.
      // LEDs o and b are set upon call by flags values.
      digitalWrite(pinLED_g,bg);
      digitalWrite(pinLED_y,by);
      digitalWrite(pinLED_r,br);
      digitalWrite(pinLED_o,flagRunA + flagRunM); // on when in auto and sequence activated or when runM active to warn that system is active
       digitalWrite(pinLED_b,1-flagAuto); // off when in auto (flagAuto = 1), on when in manual (flagAuto = 0)
```

Appendix F

Arduino script for pressure sensor

```
#include <Wire.h>
#include <SparkFun_MicroPressure.h>
#include <time.h>

//SparkFun_MicroPressure mpr(EOC_PIN, RST_PIN, MIN_PSI, MAX_PSI);
SparkFun_MicroPressure mpr;  // Use default values with reset and EOC pins unused
SparkFun_MicroPressure mpr2; // Use default values with reset and EOC pins unused
unsigned long tCurrent_ms = 0; // current time in milliseconds
const int xpin = A0;                  // x-axis of the accelerometer
const int zpin = A1;                  // z-axis (only on 3-axis models)
int sensorValue = 0;  // variable to store the value coming from the sensor
unsigned long next_millis;
unsigned long current_millis;
int period_millis = 10;

/*GY61 data sheet for acceleration sensor*/
unsigned long number_data_points = 0;
float total_value = 0.0;
float total_value1 = 0.0;

void setup() {
  // Initalize UART, I2C bus, and connect to the micropressure sensor
  Serial.begin(115200);
  Wire.begin();
  next_millis = period_millis + millis();

;

if (!mpr2.begin(0x28, Wire)) {
    Serial.println("Cannot connect to MicroPressure sensor 2 - address 0x28.");
    while (1)
      ;
  }
  if (!mpr.begin(0x18, Wire)) {
    Serial.println("Cannot connect to MicroPressure sensor 1 - address 0x18.");
    while (2)
      ;
  }
}

void loop() {
  tCurrent_ms = millis();
  int x = analogRead(xpin);  //read from xpin
  int z = analogRead(zpin);  //read from zpin

  float zero_G = 512.0; //ADC is 0~1023  the zero g output equal to Vs/2
```

```
                    //ADXL335 power supply by Vs 3.3V
  float scale = 102.3;  //ADXL335330 Sensitivity is 330mv/g
                     //330 * 1024/3.3/1000

    Serial.print(tCurrent_ms);
    Serial.print(" ");
    Serial.print(mpr.readPressure(KPA), 4);
    Serial.print(" ");/*Serial.println(" kPa from sensor 1");*/
    Serial.print(mpr2.readPressure(KPA), 4);
    Serial.print(" ");
    Serial.print(((float)x - 329)/65/*offset*/*9.8);  //print x value on serial monitor
    Serial.print("\t");
    Serial.print(((float)z - 365)/68/*offset*/ *9.8); //print z value on serial monitor
    Serial.print("\n");


  delay(0);


}
```

Appendix G

Connection on diagram – Data acquisition setup

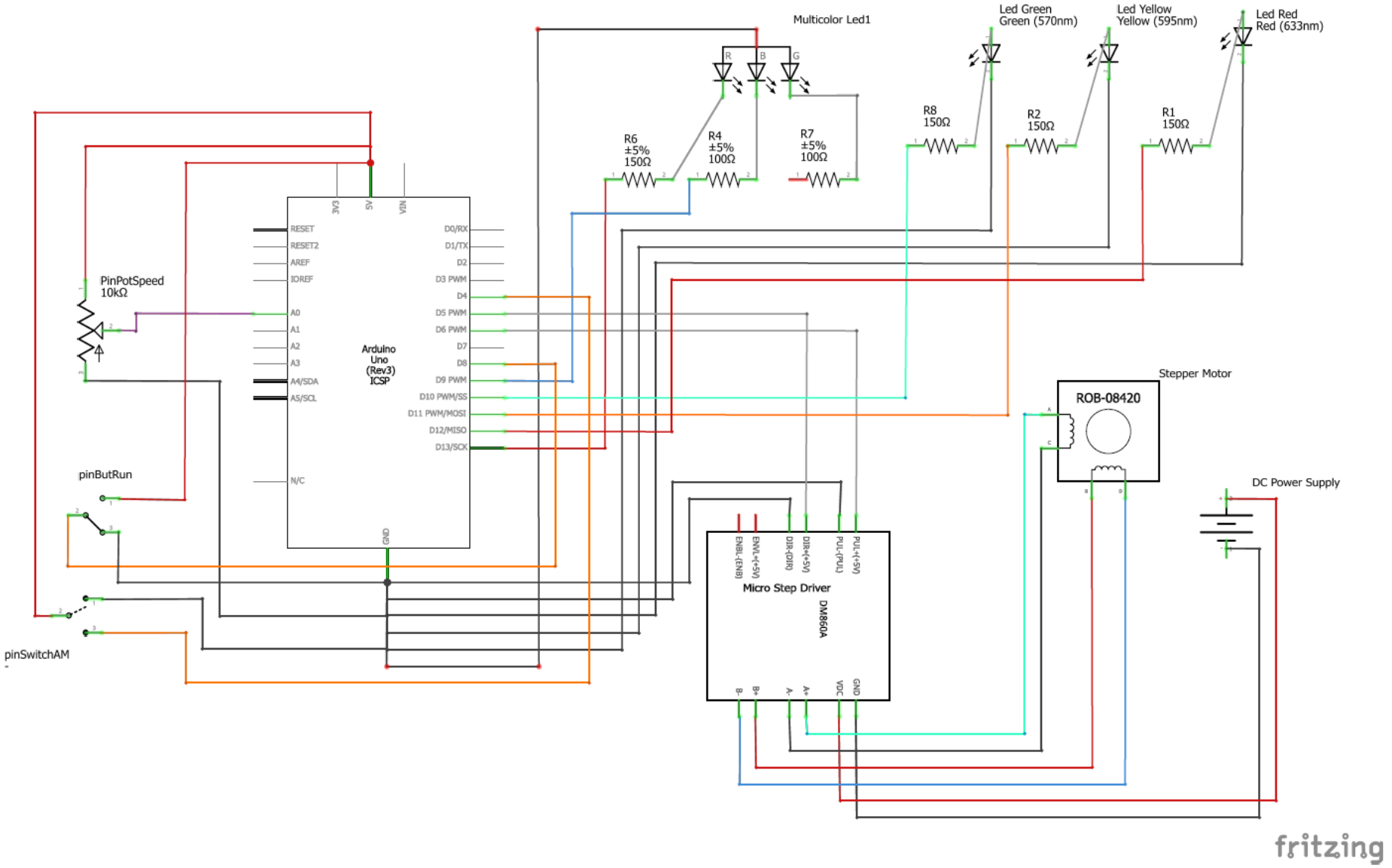

Appendix H

Data processing algorithm – MathWorks MATLAB

```
%    Workbook: D:\Anneloes\BU-Anneloes-20240416-16u56.xlsx
%    Version: July 7, 2024
%
% Auto-generated by MATLAB on 22-Apr-2024 21:48:23
clear all
close all

%% Set up the Import Options and import the data
opts = spreadsheetImportOptions("NumVariables", 25);

% Specify sheet and range
opts.Sheet = "Blad1";
opts.DataRange = "A1:Y2787";

% Specify column names and types
opts.VariableNames = ["Time1", "Sensor1", "Sensor2", "Xas1", "Zas1", "Time2", "Sensor12",
"Sensor22", "Xas2", "Zas2", "Time3", "Sensor13", "Sensor23", "Xas3", "Zas3", "Time4",
"Sensor14", "Sensor24", "Xas4", "Zas4", "Time5", "Sensor15", "Sensor25", "Xas5", "Zas5"];
opts.VariableTypes = ["double", "double", "double", "double", "double", "double", "double",
"double", "double", "double", "double", "double", "double", "double", "double", "double",
"double", "double", "double", "double", "double", "double", "double", "double", "double"];

% Import the data
POIOData = readtable("PO_IO_Data.xlsx", opts, "UseExcel", false);
%Pig open, Infant open
POPCData = readtable("PO_PC_Data.xlsx", opts, "UseExcel", false);
%Pig open, Pig closed
POICData = readtable("PO_IC_Data.xlsx", opts, "UseExcel", false);
%Pig open, Infant closed
IOPOData = readtable("IO_PO_Data.xlsx", opts, "UseExcel", false);
%Infant open, Pig open
IOICData = readtable("IO_IC_Data.xlsx", opts, "UseExcel", false);
%Infatn open, Infant closed
IOPCData = readtable("IO_PC_Data.xlsx", opts, "UseExcel", false);
%Infant open, Pig closed
ICPOData = readtable("IC_PO_Data.xlsx", opts, "UseExcel", false);
%Infant closed, Pig open
ICPCData = readtable("IC_PC_Data.xlsx", opts, "UseExcel", false);
%Infant closed, Pig closed
ICIOData = readtable("IC_IO_Data.xlsx", opts, "UseExcel", false);
%Infant closed, Infant open
PCICData = readtable("PC_IC_Data.xlsx", opts, "UseExcel", false);
%Pig closed, Infant closed
PCIOData = readtable("PC_IO_Data.xlsx", opts, "UseExcel", false);
%Pig closed, Infant open
PCPOData = readtable("PC_PO_Data.xlsx", opts, "UseExcel", false);
%Pic closed, Pig open

%% Selection of the Data
%First part of the measurement without any movement of the shake simulator
%The calibration part
Time_Static = ([POPCData{2:300,1}, POPCData{2:300,6},POPCData{2:300,11}, POPCData{2:300,16},
POPCData{2:300,21} ...
        POIOData{2:300,1}, POIOData{2:300,6},POIOData{2:300,11}, POIOData{2:300,16},
POIOData{2:300,21} ...
        POICData{2:300,1}, POICData{2:300,6},POICData{2:300,11}, POICData{2:300,16},
POICData{2:300,21} ...
        IOPOData{2:300,1}, IOPOData{2:300,6},IOPOData{2:300,11}, IOPOData{2:300,16},
IOPOData{2:300,21} ...
```

```
        IOPCData{2:300,1}, IOPCData{2:300,6},IOPCData{2:300,11}, IOPCData{2:300,16},
IOPCData{2:300,21} ...
        IOICData{2:300,1}, IOICData{2:300,6},IOICData{2:300,11}, IOICData{2:300,16},
IOICData{2:300,21} ...
        PCPOData{2:300,1}, PCPOData{2:300,6},PCPOData{2:300,11}, PCPOData{2:300,16},
PCPOData{2:300,21} ...
        PCIOData{2:300,1}, PCIOData{2:300,6},PCIOData{2:300,11}, PCIOData{2:300,16},
PCIOData{2:300,21} ...
        PCICData{2:300,1}, PCICData{2:300,6},PCICData{2:300,11}, PCICData{2:300,16},
PCICData{2:300,21} ...
        ICIOData{2:300,1}, ICIOData{2:300,6},ICIOData{2:300,11}, ICIOData{2:300,16},
ICIOData{2:300,21} ...
        ICPOData{2:300,1}, ICPOData{2:300,6},ICPOData{2:300,11}, ICPOData{2:300,16},
ICPOData{2:300,21}...
        ICPCData{2:300,1}, ICPCData{2:300,6},ICPCData{2:300,11}, ICPCData{2:300,16},
ICPCData{2:300,21} ...
        ])/1000;

%flat is the actual shake period of 5 seconds
Time_flat = ([POPCData{1625:2000,1}, POPCData{1625:2000,6},POPCData{1625:2000,11},
POPCData{1625:2000,16}, POPCData{1625:2000,21} ...
        POIOData{1625:2000,1}, POIOData{1625:2000,6},POIOData{1625:2000,11},
POIOData{1625:2000,16}, POIOData{1625:2000,21} ...
        POICData{1625:2000,1}, POICData{1625:2000,6},POICData{1625:2000,11},
POICData{1625:2000,16}, POICData{1625:2000,21} ...
        IOPOData{1625:2000,1}, IOPOData{1625:2000,6},IOPOData{1625:2000,11},
IOPOData{1625:2000,16}, IOPOData{1625:2000,21} ...
        IOPCData{1625:2000,1}, IOPCData{1625:2000,6},IOPCData{1625:2000,11},
IOPCData{1625:2000,16}, IOPCData{1625:2000,21} ...
        IOICData{1625:2000,1}, IOICData{1625:2000,6},IOICData{1625:2000,11},
IOICData{1625:2000,16}, IOICData{1625:2000,21} ...
        PCPOData{1625:2000,1}, PCPOData{1625:2000,6},PCPOData{1625:2000,11},
PCPOData{1625:2000,16}, PCPOData{1625:2000,21} ...
        PCIOData{1625:2000,1}, PCIOData{1625:2000,6},PCIOData{1625:2000,11},
PCIOData{1625:2000,16}, PCIOData{1625:2000,21} ...
        PCICData{1625:2000,1}, PCICData{1625:2000,6},PCICData{1625:2000,11},
PCICData{1625:2000,16}, PCICData{1625:2000,21} ...
        ICIOData{1625:2000,1}, ICIOData{1625:2000,6},ICIOData{1625:2000,11},
ICIOData{1625:2000,16}, ICIOData{1625:2000,21} ...
        ICPOData{1625:2000,1}, ICPOData{1625:2000,6},ICPOData{1625:2000,11},
ICPOData{1625:2000,16}, ICPOData{1625:2000,21}...
        ICPCData{1625:2000,1}, ICPCData{1625:2000,6},ICPCData{1625:2000,11},
ICPCData{1625:2000,16}, ICPCData{1625:2000,21} ...
        ])/1000;

%The calibration part of Sensor 1 with address x18
Sensor1_Static = ([POPCData{2:300,2}*10000, POPCData{2:300,7}*10000,POPCData{2:300,12}*10000,
POPCData{2:300,17}*10000, POPCData{2:300,22}*10000 ...
        POIOData{2:300,2}, POIOData{2:300,7},POIOData{2:300,12}, POIOData{2:300,17},
POIOData{2:300,22} ...
        POICData{2:300,2}, POICData{2:300,7},POICData{2:300,12}, POICData{2:300,17},
POICData{2:300,22} ...
        IOPOData{2:300,2}, IOPOData{2:300,7},IOPOData{2:300,12}, IOPOData{2:300,17},
IOPOData{2:300,22} ...
        IOPCData{2:300,2}*10000, IOPCData{2:300,7}*10000,IOPCData{2:300,12}*10000,
IOPCData{2:300,17}*10000, IOPCData{2:300,22}*10000 ...
        IOICData{2:300,2}, IOICData{2:300,7},IOICData{2:300,12}, IOICData{2:300,17},
IOICData{2:300,22} ...
        PCPOData{2:300,2}, PCPOData{2:300,7},PCPOData{2:300,12}, PCPOData{2:300,17},
PCPOData{2:300,22} ...
```

```
        PCIOData{2:300,2}, PCIOData{2:300,7},PCIOData{2:300,12}, PCIOData{2:300,17},
PCIOData{2:300,22} ...
        PCICData{2:300,2}, PCICData{2:300,7},PCICData{2:300,12}, PCICData{2:300,17},
PCICData{2:300,22} ...
        ICIOData{2:300,2}, ICIOData{2:300,7},ICIOData{2:300,12}, ICIOData{2:300,17},
ICIOData{2:300,22} ...
        ICPOData{2:300,2}, ICPOData{2:300,7},ICPOData{2:300,12}, ICPOData{2:300,17},
ICPOData{2:300,22}...
        ICPCData{2:300,2}, ICPCData{2:300,7},ICPCData{2:300,12}, ICPCData{2:300,17},
ICPCData{2:300,22} ...
        ])/10000;

%Calibration part of sensor2 with address x28
Sensor2_Static = ([POPCData{2:300,3}*10000, POPCData{2:300,8}*10000,POPCData{2:300,13}*10000,
POPCData{2:300,18}*10000, POPCData{2:300,23}*10000 ...
        POIOData{2:300,3}, POIOData{2:300,8},POIOData{2:300,13}, POIOData{2:300,18},
POIOData{2:300,23} ...
        POICData{2:300,3}, POICData{2:300,8},POICData{2:300,13}, POICData{2:300,18},
POICData{2:300,23} ...
        IOPOData{2:300,3}, IOPOData{2:300,8},IOPOData{2:300,13}, IOPOData{2:300,18},
IOPOData{2:300,23} ...
        IOPCData{2:300,3}*10000, IOPCData{2:300,8}*10000,IOPCData{2:300,13}*10000,
IOPCData{2:300,18}*10000, IOPCData{2:300,23}*10000 ...
        IOICData{2:300,3}, IOICData{2:300,8},IOICData{2:300,13}, IOICData{2:300,18},
IOICData{2:300,23} ...
        PCPOData{2:300,3}, PCPOData{2:300,8},PCPOData{2:300,13}, PCPOData{2:300,18},
PCPOData{2:300,23} ...
        PCIOData{2:300,3}, PCIOData{2:300,8},PCIOData{2:300,13}, PCIOData{2:300,18},
PCIOData{2:300,23} ...
        PCICData{2:300,3}, PCICData{2:300,8},PCICData{2:300,13}, PCICData{2:300,18},
PCICData{2:300,23} ...
        ICIOData{2:300,3}, ICIOData{2:300,8},ICIOData{2:300,13}, ICIOData{2:300,18},
ICIOData{2:300,23} ...
        ICPOData{2:300,3}, ICPOData{2:300,8},ICPOData{2:300,13}, ICPOData{2:300,18},
ICPOData{2:300,23}...
        ICPCData{2:300,3}, ICPCData{2:300,8},ICPCData{2:300,13}, ICPCData{2:300,18},
ICPCData{2:300,23} ...
        ])/10000;

%Shake period of Sensor 1 of 5 seconds
Sensor1_flat =  ([POPCData{1625:2000,2}*10000,
POPCData{1625:2000,7}*10000,POPCData{1625:2000,12}*10000, POPCData{1625:2000,17}*10000,
POPCData{1625:2000,22}*10000 ...
        POIOData{1625:2000,2}, POIOData{1625:2000,7},POIOData{1625:2000,12},
POIOData{1625:2000,17}, POIOData{1625:2000,22} ...
        POICData{1625:2000,2}, POICData{1625:2000,7},POICData{1625:2000,12},
POICData{1625:2000,17}, POICData{1625:2000,22} ...
        IOPOData{1625:2000,2}, IOPOData{1625:2000,7},IOPOData{1625:2000,12},
IOPOData{1625:2000,17}, IOPOData{1625:2000,22} ...
        IOPCData{1625:2000,2}*10000, IOPCData{1625:2000,7}*10000,IOPCData{1625:2000,12}*10000,
IOPCData{1625:2000,17}*10000, IOPCData{1625:2000,22}*10000 ...
        IOICData{1625:2000,2}, IOICData{1625:2000,7},IOICData{1625:2000,12},
IOICData{1625:2000,17}, IOICData{1625:2000,22} ...
        PCPOData{1625:2000,2}, PCPOData{1625:2000,7},PCPOData{1625:2000,12},
PCPOData{1625:2000,17}, PCPOData{1625:2000,22} ...
        PCIOData{1625:2000,2}, PCIOData{1625:2000,7},PCIOData{1625:2000,12},
PCIOData{1625:2000,17}, PCIOData{1625:2000,22} ...
        PCICData{1625:2000,2}, PCICData{1625:2000,7},PCICData{1625:2000,12},
PCICData{1625:2000,17}, PCICData{1625:2000,22} ...
        ICIOData{1625:2000,2}, ICIOData{1625:2000,7},ICIOData{1625:2000,12},
ICIOData{1625:2000,17}, ICIOData{1625:2000,22} ...
```

```
        ICPODData{1625:2000,2}, ICPODData{1625:2000,7},ICPODData{1625:2000,12},
ICPODData{1625:2000,17}, ICPODData{1625:2000,22}...
        ICPCData{1625:2000,2}, ICPCData{1625:2000,7},ICPCData{1625:2000,12},
ICPCData{1625:2000,17}, ICPCData{1625:2000,22} ...
        ])/10000;

%Shake period of Sensor 2 of 5 seconds
Sensor2_flat = ([POPCData{1625:2000,3}*10000,
POPCData{1625:2000,8}*10000,POPCData{1625:2000,13}*10000, POPCData{1625:2000,18}*10000
POPCData{1625:2000,23}*10000  ...
        POIOData{1625:2000,3}, POIOData{1625:2000,8},POIOData{1625:2000,13},
POIOData{1625:2000,18}, POIOData{1625:2000,23} ...
        POICData{1625:2000,3}, POICData{1625:2000,8},POICData{1625:2000,13},
POICData{1625:2000,18}, POICData{1625:2000,23} ...
        IOPOData{1625:2000,3}, IOPOData{1625:2000,8},IOPOData{1625:2000,13},
IOPOData{1625:2000,18}, IOPOData{1625:2000,23} ...
        IOPCData{1625:2000,3}*10000, IOPCData{1625:2000,8}*10000,IOPCData{1625:2000,13}*10000,
IOPCData{1625:2000,18}*10000, IOPCData{1625:2000,23}*10000 ...
        IOICData{1625:2000,3}, IOICData{1625:2000,8},IOICData{1625:2000,13},
IOICData{1625:2000,18}, IOICData{1625:2000,23} ...
        PCPOData{1625:2000,3}, PCPOData{1625:2000,8},PCPOData{1625:2000,13},
PCPOData{1625:2000,18}, PCPOData{1625:2000,23} ...
        PCIOData{1625:2000,3}, PCIOData{1625:2000,8},PCIOData{1625:2000,13},
PCIOData{1625:2000,18}, PCIOData{1625:2000,23} ...
        PCICData{1625:2000,3}, PCICData{1625:2000,8},PCICData{1625:2000,13},
PCICData{1625:2000,18}, PCICData{1625:2000,23} ...
        ICIOData{1625:2000,3}, ICIOData{1625:2000,8},ICIOData{1625:2000,13},
ICIOData{1625:2000,18}, ICIOData{1625:2000,23} ...
        ICPOData{1625:2000,3}, ICPOData{1625:2000,8},ICPOData{1625:2000,13},
ICPOData{1625:2000,18}, ICPOData{1625:2000,23}...
        ICPCData{1625:2000,3}, ICPCData{1625:2000,8},ICPCData{1625:2000,13},
ICPCData{1625:2000,18}, ICPCData{1625:2000,23} ...
        ])/10000;

%The 40 seconds shake periode of Sensor1
Sensor1_all =  ([POPCData{:,2}*10000, POPCData{:,7}*10000,POPCData{:,12}*10000,
POPCData{:,17}*10000, POPCData{:,22}*10000 ...
        POIOData{:,2}, POIOData{:,7},POIOData{:,12}, POIOData{:,17}, POIOData{:,22} ...
        POICData{:,2}, POICData{:,7},POICData{:,12}, POICData{:,17}, POICData{:,22} ...
        IOPOData{:,2}, IOPOData{:,7},IOPOData{:,12}, IOPOData{:,17}, IOPOData{:,22} ...
        IOPCData{:,2}*10000, IOPCData{:,7}*10000,IOPCData{:,12}*10000, IOPCData{:,17}*10000,
IOPCData{:,22}*10000 ...
        IOICData{:,2}, IOICData{:,7},IOICData{:,12}, IOICData{:,17}, IOICData{:,22} ...
        PCPOData{:,2}, PCPOData{:,7},PCPOData{:,12}, PCPOData{:,17}, PCPOData{:,22} ...
        PCIOData{:,2}, PCIOData{:,7},PCIOData{:,12}, PCIOData{:,17}, PCIOData{:,22} ...
        PCICData{:,2}, PCICData{:,7},PCICData{:,12}, PCICData{:,17}, PCICData{:,22} ...
        ICIOData{:,2}, ICIOData{:,7},ICIOData{:,12}, ICIOData{:,17}, ICIOData{:,22} ...
        ICPOData{:,2}, ICPOData{:,7},ICPOData{:,12}, ICPOData{:,17}, ICPOData{:,22}...
        ICPCData{:,2}, ICPCData{:,7},ICPCData{:,12}, ICPCData{:,17}, ICPCData{:,22} ...
        ])/10000;

%The 40 seconds shake period of Sensor2
Sensor2_all = ([POPCData{:,3}*10000, POPCData{:,8}*10000,POPCData{:,13}*10000,
POPCData{:,18}*10000 POPCData{:,23}*10000  ...
        POIOData{:,3}, POIOData{:,8},POIOData{:,13}, POIOData{:,18}, POIOData{:,23} ...
        POICData{:,3}, POICData{:,8},POICData{:,13}, POICData{:,18}, POICData{:,23} ...
        IOPOData{:,3}, IOPOData{:,8},IOPOData{:,13}, IOPOData{:,18}, IOPOData{:,23} ...
        IOPCData{:,3}*10000, IOPCData{:,8}*10000,IOPCData{:,13}*10000, IOPCData{:,18}*10000,
IOPCData{:,23}*10000 ...
        IOICData{:,3}, IOICData{:,8},IOICData{:,13}, IOICData{:,18}, IOICData{:,23} ...
        PCPOData{:,3}, PCPOData{:,8},PCPOData{:,13}, PCPOData{:,18}, PCPOData{:,23} ...
```

```
        PCIOData{:,3}, PCIOData{:,8},PCIOData{:,13}, PCIOData{:,18}, PCIOData{:,23} ...
        PCICData{:,3}, PCICData{:,8},PCICData{:,13}, PCICData{:,18}, PCICData{:,23} ...
        ICIOData{:,3}, ICIOData{:,8},ICIOData{:,13}, ICIOData{:,18}, ICIOData{:,23} ...
        ICPOData{:,3}, ICPOData{:,8},ICPOData{:,13}, ICPOData{:,18}, ICPOData{:,23}...
        ICPCData{:,3}, ICPCData{:,8},ICPCData{:,13}, ICPCData{:,18}, ICPCData{:,23} ...
        ])/10000;
%The 40 seconds shake period of the time
Time_all = ([POPCData{:,1}, POPCData{:,6},POPCData{:,11}, POPCData{:,16}, POPCData{:,21} ...
        POIOData{:,1}, POIOData{:,6},POIOData{:,11}, POIOData{:,16}, POIOData{:,21} ...
        POICData{:,1}, POICData{:,6},POICData{:,11}, POICData{:,16}, POICData{:,21} ...
        IOPOData{:,1}, IOPOData{:,6},IOPOData{:,11}, IOPOData{:,16}, IOPOData{:,21} ...
        IOPCData{:,1}, IOPCData{:,6},IOPCData{:,11}, IOPCData{:,16}, IOPCData{:,21} ...
        IOICData{:,1}, IOICData{:,6},IOICData{:,11}, IOICData{:,16}, IOICData{:,21} ...
        PCPOData{:,1}, PCPOData{:,6},PCPOData{:,11}, PCPOData{:,16}, PCPOData{:,21} ...
        PCIOData{:,1}, PCIOData{:,6},PCIOData{:,11}, PCIOData{:,16}, PCIOData{:,21} ...
        PCICData{:,1}, PCICData{:,6},PCICData{:,11}, PCICData{:,16}, PCICData{:,21} ...
        ICIOData{:,1}, ICIOData{:,6},ICIOData{:,11}, ICIOData{:,16}, ICIOData{:,21} ...
        ICPOData{:,1}, ICPOData{:,6},ICPOData{:,11}, ICPOData{:,16}, ICPOData{:,21}...
        ICPCData{:,1}, ICPCData{:,6},ICPCData{:,11}, ICPCData{:,16}, ICPCData{:,21} ...
        ])/1000;


%Shake period of 5 seconds Accelation of X-direction
Xa = ([POPCData{1625:2000,4}, POPCData{1625:2000,9},POPCData{1625:2000,14},
POPCData{1625:2000,19}, POPCData{1625:2000,24} ...
        POIOData{1625:2000,4}, POIOData{1625:2000,9},POIOData{1625:2000,14},
POIOData{1625:2000,19}, POIOData{1625:2000,24} ...
        POICData{1625:2000,4}, POICData{1625:2000,9},POICData{1625:2000,14},
POICData{1625:2000,19}, POICData{1625:2000,24} ...
        IOPOData{1625:2000,4}, IOPOData{1625:2000,9},IOPOData{1625:2000,14},
IOPOData{1625:2000,19}, IOPOData{1625:2000,24} ...
        IOPCData{1625:2000,4}, IOPCData{1625:2000,9},IOPCData{1625:2000,14},
IOPCData{1625:2000,19}, IOPCData{1625:2000,24} ...
        IOICData{1625:2000,4}, IOICData{1625:2000,9},IOICData{1625:2000,14},
IOICData{1625:2000,19}, IOICData{1625:2000,24} ...
        PCPOData{1625:2000,4}, PCPOData{1625:2000,9},PCPOData{1625:2000,14},
PCPOData{1625:2000,19}, PCPOData{1625:2000,24} ...
        PCIOData{1625:2000,4}, PCIOData{1625:2000,9},PCIOData{1625:2000,14},
PCIOData{1625:2000,19}, PCIOData{1625:2000,24} ...
        PCICData{1625:2000,4}, PCICData{1625:2000,9},PCICData{1625:2000,14},
PCICData{1625:2000,19}, PCICData{1625:2000,24} ...
        ICIOData{1625:2000,4}, ICIOData{1625:2000,9},ICIOData{1625:2000,14},
ICIOData{1625:2000,19}, ICIOData{1625:2000,24} ...
        ICPOData{1625:2000,4}, ICPOData{1625:2000,9},ICPOData{1625:2000,14},
ICPOData{1625:2000,19}, ICPOData{1625:2000,24}...
        ICPCData{1625:2000,4}, ICPCData{1625:2000,9},ICPCData{1625:2000,14},
ICPCData{1625:2000,19}, ICPCData{1625:2000,24} ...
        ])*10;

%Shake period of 5 seconds Acceleration of Z-direction
Za =  ([POPCData{1625:2000,5}, POPCData{1625:2000,10},POPCData{1625:2000,15},
POPCData{1625:2000,20}, POPCData{1625:2000,25} ...
        POIOData{1625:2000,5}, POIOData{1625:2000,10},POIOData{1625:2000,15},
POIOData{1625:2000,20}, POIOData{1625:2000,25} ...
        POICData{1625:2000,5}, POICData{1625:2000,10},POICData{1625:2000,15},
POICData{1625:2000,20}, POICData{1625:2000,25} ...
        IOPOData{1625:2000,5}, IOPOData{1625:2000,10},IOPOData{1625:2000,15},
IOPOData{1625:2000,20}, IOPOData{1625:2000,25} ...
        IOPCData{1625:2000,5}, IOPCData{1625:2000,10},IOPCData{1625:2000,15},
IOPCData{1625:2000,20}, IOPCData{1625:2000,25} ...
```

```
        IOICData{1625:2000,5}, IOICData{1625:2000,10},IOICData{1625:2000,15},
IOICData{1625:2000,20}, IOICData{1625:2000,25} ...
        PCPOData{1625:2000,5}, PCPOData{1625:2000,10},PCPOData{1625:2000,15},
PCPOData{1625:2000,20}, PCPOData{1625:2000,25} ...
        PCIOData{1625:2000,5}, PCIOData{1625:2000,10},PCIOData{1625:2000,15},
PCIOData{1625:2000,20}, PCIOData{1625:2000,25} ...
        PCICData{1625:2000,5}, PCICData{1625:2000,10},PCICData{1625:2000,15},
PCICData{1625:2000,20}, PCICData{1625:2000,25} ...
        ICIOData{1625:2000,5}, ICIOData{1625:2000,10},ICIOData{1625:2000,15},
ICIOData{1625:2000,20}, ICIOData{1625:2000,25} ...
        ICPOData{1625:2000,5}, ICPOData{1625:2000,10},ICPOData{1625:2000,15},
ICPOData{1625:2000,20}, ICPOData{1625:2000,25} ...
        ICPCData{1625:2000,5}, ICPCData{1625:2000,10},ICPCData{1625:2000,15},
ICPCData{1625:2000,20}, ICPCData{1625:2000,25} ...
        ])*10;

%%Calculating calibration
Time = Caldata{1:600,1}/1000;
Sensor1 =Caldata{1:600,2}/10000;
Sensor2 = Caldata{1:600,3}/10000;

MeanS1 = mean(Sensor1)
MeanS2 = mean(Sensor2)
DMS1S2 = abs(MeanS1-MeanS2)

%% Administration before filtering data

fs = 90; % fs from datasheet
%
Onderzoeken welke frequencies aanwezig zijn om hiermee te filteren
%Power spectral density estimate
[h,g] = pwelch(Sensor1_flat - mean(Sensor1_flat), [],[],[],fs);
[t,p] = pwelch(Sensor2_flat - mean(Sensor2_flat), [],[],[],fs);
[h1,g1] = pwelch(Sensor1_Static - mean(Sensor1_Static), [],[],[],fs);
[t1,p1] = pwelch(Sensor2_Static - mean(Sensor2_Static), [],[],[],fs);

N = 2;
fc1 = 3; %Cutoff frequency forflat Period
fc2 = 6; %Cutoff frequency for Static period

%filtering sensor 1 and sensor 2 signals in both flat and static part; Apply low-pass filter on
accelerometer signals
%a second order butterworth filter is conducted.
Wn_1 = fc1/(fs/2);
Wn_2 = fc2/(fs/2);
[B,A] = butter(N,Wn_1, "low");
[C,D] = butter(N,Wn_2, "low");
Filtsig1 = filtfilt(B,A, Sensor1_flat);
Filtsig2 = filtfilt(B,A, Sensor2_flat);
Filtsig1static = filtfilt(C,D, Sensor1_Static);
Filtsig2static = filtfilt(C,D, Sensor2_Static);

%%
%Calculating the mean signal for the first 10 seconds
%calibrate

GemSensor1static = mean(Filtsig1static(:,1:5),"all");
GemSensor2static = mean(Filtsig2static(:,1:5),"all");
```

```
%Calculating the mean time signal for the first 10 seconds
GemTimeflat = mean(Time_flat,"all");
GemTimeStatic = mean(Time_Static,"all");

c = polyfit(Time_Static, Filtsig1static,1);
d = polyfit(Time_Static, Filtsig2static,1);
Sensor1startfit = polyval(c, Time_Static);
Sensor2startfit = polyval(d, Time_Static);

%% Filtering X-direction and Z-direciotn

%Missing values; The removal of missing values
Xanew = fillmissing(Xa,'constant',0);
Zanew = fillmissing(Za,'constant',0);

%PSD Z and  X accelerations
fs = 100;
[O,E]= pwelch(Zanew - mean(Zanew), [],[],[],fs);
[G,F]= pwelch(Xanew  - mean(Xanew ), [],[],[],fs);

N = 2; % Order
fc_xz = 6;  % de cut-off freqency in Hz van X and Z

%Filter Z and X accelerations
Wnas = fc_xz/(fs/2);
[B,A] = butter(N,Wnas, 'low');
[D,C]= butter(N,Wnas, "low");
Zafilt = filtfilt(D,C,Zanew);
Xafilt = filtfilt(B,A,Xanew);

%% max peak en min peak van alle combinaties
Calculating the mean of the baseline per session in position left; orbit 1. Also called as the
ambient pressure (Ps).

MPOPC1_static = mean(Filtsig1static(:,1:5),"all");
MPOIO1_static = mean(Filtsig1static(:,6:10),"all");
MPOIC1_static = mean(Filtsig1static(:,11:15),"all");
MIOPO1_static = mean(Filtsig1static(:,16:20),"all");
MIOPC1_static = mean(Filtsig1static(:,21:25),"all");
MIOIC1_static = mean(Filtsig1static(:,26:30),"all");
MPCPO1_static = mean(Filtsig1static(:,31:35),"all");
MPCIO1_static = mean(Filtsig1static(:,36:40),"all");
MPCIC1_static = mean(Filtsig1static(:,41:45),"all");
MICIO1_static = mean(Filtsig1static(:,46:50),"all");
MICPO1_static = mean(Filtsig1static(:,51:55),"all");
MICPC1_static = mean(Filtsig1static(:,56:60),"all");


% Calculating the mean of the baseline per session in position left; orbit 2; Also called as
the ambient pressure (Ps).
MPOPC2_static = mean(Filtsig2static(:,1:5),"all");
MPOIO2_static = mean(Filtsig2static(:,6:10),"all");
MPOIC2_static = mean(Filtsig2static(:,11:15),"all");
MIOPO2_static = mean(Filtsig2static(:,16:20),"all");
MIOPC2_static = mean(Filtsig2static(:,21:25),"all");
MIOIC2_static = mean(Filtsig2static(:,26:30),"all");
MPCPO2_static = mean(Filtsig2static(:,31:35),"all");
MPCIO2_static = mean(Filtsig2static(:,36:40),"all");
MPCIC2_static = mean(Filtsig2static(:,41:45),"all");
MICIO2_static = mean(Filtsig2static(:,46:50),"all");
MICPO2_static = mean(Filtsig2static(:,51:55),"all");
```

```
MICPC2_static = mean(Filtsig2static(:,56:60),"all");

%Calculating the mean of the signal for sensor 1 per orbit combiation.
%trails dus per combinatie minus the ambient pressure (Ps).


MPO1_PC = mean((Filtsig1(:,1:5) - MPOPC1_static),2);
MPO1_IO = mean((Filtsig1(:,6:10)-MPOIO1_static),2);
MPO1_IC = mean((Filtsig1(:,11:15)-MPOIC1_static),2);
MIO1_PO = mean((Filtsig1(:,16:20)-MIOPO1_static),2);
MIO1_PC = mean((Filtsig1(:,21:25)-MIOPC1_static),2);
MIO1_IC = mean((Filtsig1(:,26:30)-MIOIC1_static),2);
MPC1_PO = mean((Filtsig1(:,31:35)-MPCPO1_static),2);
MPC1_IO = mean((Filtsig1(:,36:40)-MPCIO1_static),2);
MPC1_IC = mean((Filtsig1(:,41:45)-MPCIC1_static),2);
MIC1_IO = mean((Filtsig1(:,46:50)-MICIO1_static),2);
MIC1_PO = mean((Filtsig1(:,51:55)-MICPO1_static),2);
MIC1_PC = mean((Filtsig1(:,56:60)-MPOPC1_static),2);



% Calculating the mean of the signal for sensor 2 per orbit combiation.
%trails dus per combinatie minus the ambient pressure (Ps).

MPO2_PC = mean((Filtsig2(:,1:5)-MPOPC2_static),2);
MPO2_IO = mean((Filtsig2(:,6:10)-MPOIO2_static),2);
MPO2_IC = mean((Filtsig2(:,11:15)-MPOIC2_static),2);
MIO2_PO = mean((Filtsig2(:,16:20)-MIOPO2_static),2);
MIO2_PC = mean((Filtsig2(:,21:25)-MIOPC2_static),2);
MIO2_IC = mean((Filtsig2(:,26:30)-MIOIC2_static),2);
MPC2_PO = mean((Filtsig2(:,31:35)-MPCPO2_static),2);
MPC2_IO = mean((Filtsig2(:,36:40)-MPCIO2_static),2);
MPC2_IC = mean((Filtsig2(:,41:45)-MPCIC2_static),2);
MIC2_IO = mean((Filtsig2(:,46:50)-MICIO2_static),2);
MIC2_PO = mean((Filtsig2(:,51:55)-MICPO2_static),2);
MIC2_PC = mean((Filtsig2(:,56:60)-MICPC2_static),2);

%The max and min peak of the mean signals for sensor 1.
maxpeakPOPC1 = findpeaks(MPO1_PC);
minpeakPOPC1 = -(findpeaks(-MPO1_PC));
maxpeakPOIO1 = findpeaks(MPO1_IO);
minpeakPOIO1 = -(findpeaks(-MPO1_IO));
maxpeakPOIC1 = findpeaks(MPO1_IC);
minpeakPOIC1 = -(findpeaks(-MPO1_IC));
maxpeakIOPO1 = findpeaks(MIO1_PO);
minpeakIOPO1 = -(findpeaks(-MIO1_PO));
maxpeakIOPC1 = findpeaks(MIO1_PC);
minpeakIOPC1 = -(findpeaks(-MIO1_PC));
maxpeakIOIC1 = findpeaks(MIO1_IC);
minpeakIOIC1 = -(findpeaks(-MIO1_IC));
maxpeakPCPO1 = findpeaks(MPC1_PO);
minpeakPCPO1 = -(findpeaks(-MPC1_PO));
maxpeakPCIO1 = findpeaks(MPC1_IO);
minpeakPCIO1 = -(findpeaks(-MPC1_IO));
maxpeakPCIC1 = findpeaks(MPC1_IC);
minpeakPCIC1 = -(findpeaks(-MPC1_IC));
maxpeakICIO1 = findpeaks(MIC1_IO);
minpeakICIO1 = -(findpeaks(-MIC1_IO));
maxpeakICPC1 = findpeaks(MIC1_PC);
minpeakICPC1 = -(findpeaks(-MIC1_PC));
maxpeakICPO1 = findpeaks(MIC1_PO);
```

```
minpeakICPO1 = -(findpeaks(-MIC1_PO));

% The max and min peak of the mean signals for sensor 1.
maxpeakPOPC2 =   findpeaks(MPO2_PC);
minpeakPOPC2 = -(findpeaks(-MPO2_PC));
maxpeakPOIO2 = findpeaks(MPO2_IO);
minpeakPOIO2 = -(findpeaks(-MPO2_IO));
maxpeakPOIC2 = findpeaks(MPO2_IC);
minpeakPOIC2 = -(findpeaks(-MPO2_IC));
maxpeakIOPO2 = findpeaks(MIO2_PO);
minpeakIOPO2 = -(findpeaks(-MIO2_PO));
maxpeakIOPC2 = findpeaks(MIO2_PC);
minpeakIOPC2 = -(findpeaks(-MIO2_PC));
maxpeakIOIC2 = findpeaks(MIO2_IC);
minpeakIOIC2 = -(findpeaks(-MIO2_IC));
maxpeakPCPO2 = findpeaks(MPC2_PO);
minpeakPCPO2 = -(findpeaks(-MPC2_PO));
maxpeakPCIO2 = findpeaks(MPC2_IO);
minpeakPCIO2 = -(findpeaks(-MPC2_IO));
maxpeakPCIC2 = findpeaks(MPC2_IC);
minpeakPCIC2 = -(findpeaks(-MPC2_IC));
maxpeakICIO2 = findpeaks(MIC2_IO);
minpeakICIO2 = -(findpeaks(-MIC2_IO));
maxpeakICPC2 = findpeaks(MIC2_PC);
minpeakICPC2 = -(findpeaks(-MIC2_PC));
maxpeakICPO2 = findpeaks(MIC2_PO);
minpeakICPO2 = -(findpeaks(-MIC2_PO));


%Calculating the median per shake period for every orbit.
PsPOPC1 = (abs(maxpeakPOPC1(1:10,:)) + abs(minpeakPOPC1(1:10,:)))/2;
PsPOIO1 = (abs(maxpeakPOIO1(1:10,:)) + abs(minpeakPOIO1(1:10,:)))/2;
PsPOIC1 = (abs(maxpeakPOIC1(1:10,:)) + abs(minpeakPOIC1(1:10,:)))/2;
PsIOPC1 = (abs(maxpeakIOPC1(1:10,:)) + abs(minpeakIOPC1(1:10,:)))/2;
PsIOPO1 = (abs(maxpeakIOPO1(1:10,:)) + abs(minpeakIOPO1(1:10,:)))/2;
PsIOIC1 = (abs(maxpeakIOIC1(1:10,:)) + abs(minpeakIOIC1(1:10,:)))/2;
PsPCPO1 = (abs(maxpeakPCPO1(1:10,:)) + abs(minpeakPCPO1(1:10,:)))/2;
PsPCIC1 = (abs(maxpeakPCIC1(1:10,:)) + abs(minpeakPCIC1(1:10,:)))/2;
PsPCIO1 = (abs(maxpeakPCIO1(1:10,:)) + abs(minpeakPCIO1(1:10,:)))/2;
PsICIO1 = (abs(maxpeakICIO1(1:10,:)) + abs(minpeakICIO1(1:10,:)))/2;
PsICPC1 = (abs(maxpeakICPC1(1:8,:)) + abs(minpeakICPC1(1:8,:)))/2;
PsICPO1 = (abs(maxpeakICPO1(1:8,:)) + abs(minpeakICPO1(1:8,:)))/2;

PsPOPC2 = (abs(maxpeakPOPC2(1:10,:)) + abs(minpeakPOPC2(1:10,:)))/2;
PsPOIO2 = (abs(maxpeakPOIO2(1:10,:)) + abs(minpeakPOIO2(1:10,:)))/2;
PsPOIC2 = (abs(maxpeakPOIC2(1:10,:)) + abs(minpeakPOIC2(1:10,:)))/2;
PsIOPC2 = (abs(maxpeakIOPC2(1:10,:)) + abs(minpeakIOPC2(1:10,:)))/2;
PsIOPO2 = (abs(maxpeakIOPO2(1:10,:)) + abs(minpeakIOPO2(1:10,:)))/2;
PsIOIC2 = (abs(maxpeakIOIC2(1:10,:)) + abs(minpeakIOIC2(1:10,:)))/2;
PsPCPO2 = (abs(maxpeakPCPO2(1:10,:)) + abs(minpeakPCPO2(1:10,:)))/2;
PsPCIC2 = (abs(maxpeakPCIC2(1:10,:)) + abs(minpeakPCIC2(1:10,:)))/2;
PsPCIO2 = (abs(maxpeakPCIO2(1:10,:)) + abs(minpeakPCIO2(1:10,:)))/2;
PsICIO2 = (abs(maxpeakICIO2(1:10,:)) + abs(minpeakICIO2(1:10,:)))/2;
PsICPC2 = (abs(maxpeakICPC2(1:8,:)) + abs(minpeakICPC2(1:8,:)))/2;
PsICPO2 = (abs(maxpeakICPO2(1:8,:)) + abs(minpeakICPO2(1:8,:)))/2;


%Calculating the difference per session between the average of the starting period and the
%maximum and minimum
PasrelPOPC1 = [abs(maxpeakPOPC1(1:10,:)) abs(minpeakPOPC1(1:10,:))];
PasrelPOIO1 = [abs(maxpeakPOIO1(1:10,:)) abs(minpeakPOIO1(1:10,:))];
```

```
PasrelPOIC1 = [abs(maxpeakPOIC1(1:10,:)) abs(minpeakPOIC1(1:10,:))];
PasrelIOPC1 = [abs(maxpeakIOPC1(1:10,:)) abs(minpeakIOPC1(1:10,:))];
PasrelIOPO1 = [abs(maxpeakIOPO1(1:10,:)) abs(minpeakIOPO1(1:10,:))];
PasrelIOIC1 = [abs(maxpeakIOIC1(1:10,:)) abs(minpeakIOIC1(1:10,:))];
PasrelPCPO1 = [abs(maxpeakPCPO1(1:10,:)) abs(minpeakPCPO1(1:10,:))];
PasrelPCIC1 = [abs(maxpeakPCIC1(1:10,:)) abs(minpeakPCIC1(1:10,:))];
PasrelPCIO1 = [abs(maxpeakPCIO1(1:10,:)) abs(minpeakPCIO1(1:10,:))];
PasrelICIO1 = [abs(maxpeakICIO1(1:10,:)) abs(minpeakICIO1(1:10,:))];
PasrelICPC1 = [abs(maxpeakICPC1(1:8,:)) abs(minpeakICPC1(1:8,:))];
PasrelICPO1 = [abs(maxpeakICPO1(1:8,:)) abs(minpeakICPO1(1:8,:))];

PasrelPOPC2 = [abs(maxpeakPOPC2(1:10,:)) abs(minpeakPOPC2(1:10,:))];
PasrelPOIO2 = [abs(maxpeakPOIO2(1:10,:)) abs(minpeakPOIO2(1:10,:))];
PasrelPOIC2 = [abs(maxpeakPOIC2(1:10,:)) abs(minpeakPOIC2(1:10,:))];
PasrelIOPC2 = [abs(maxpeakIOPC2(1:10,:)) abs(minpeakIOPC2(1:10,:))];
PasrelIOPO2 = [abs(maxpeakIOPO2(1:10,:)) abs(minpeakIOPO2(1:10,:))];
PasrelIOIC2 = [abs(maxpeakIOIC2(1:10,:)) abs(minpeakIOIC2(1:10,:))];
PasrelPCPO2 = [abs(maxpeakPCPO2(1:10,:)) abs(minpeakPCPO2(1:10,:))];
PasrelPCIC2 = [abs(maxpeakPCIC2(1:10,:)) abs(minpeakPCIC2(1:10,:))];
PasrelPCIO2 = [abs(maxpeakPCIO2(1:10,:)) abs(minpeakPCIO2(1:10,:))];
PasrelICIO2 = [abs(maxpeakICIO2(1:10,:)) abs(minpeakICIO2(1:10,:))];
PasrelICPC2 = [abs(maxpeakICPC2(1:8,:)) abs(minpeakICPC2(1:8,:))];
PasrelICPO2 = [abs(maxpeakICPO2(1:8,:)) abs(minpeakICPO2(1:8,:))];


%% Calculating the average of all maximum and minimum differences per orbit option
% Thus, the average difference of PO, PC, IO, IC from sensor 1 or 2

GemDifPOPC1 = mean(PasrelPOPC1, 'all');
GemDifPOIO1 = mean(PasrelPOIO1, 'all');
GemDifPOIC1 = mean(PasrelPOIC1, 'all');
%mean difference of PO 1
GemDifPO1 = mean([GemDifPOPC1 GemDifPOIO1 GemDifPOIC1]);

GemDifIOPC1 = mean(PasrelIOPC1, 'all');
GemDifIOPO1 = mean(PasrelIOPO1, 'all');
GemDifIOIC1 = mean(PasrelIOIC1,'all');
% mean difference of IO 1
GemDifIO1 = mean([GemDifIOPC1 GemDifIOPO1 GemDifIOIC1]);

GemDifPCPO1 = mean(PasrelPCPO1,'all');
GemDifPCIC1 = mean(PasrelPCIC1,'all');
GemDifPCIO1 = mean(PasrelPCIO1,'all');
% mean difference of PC 1
GemDifPC1 = mean([GemDifPCPO1 GemDifPCIC1 GemDifPCIO1]);

GemDifICIO1 = mean(PasrelICIO1,'all');
GemDifICPC1 = mean(PasrelICPC1,'all');
GemDifICPO1 = mean(PasrelICPO1,'all');
% mean difference of IC 1
GemDifIC1 = mean([GemDifICIO1 GemDifICPC1 GemDifICPO1]);

GemDifPOPC2 = mean(PasrelPOPC2, 'all');
GemDifIOPC2 = mean(PasrelIOPC2,'all');
GemDifICPC2 = mean(PasrelICPC2,'all');
% mean difference of PC 2
GemDifPC2 = mean([GemDifPOPC2 GemDifIOPC2 GemDifICPC2]);

GemDifPOIO2 = mean(PasrelPOIO2,'all');
GemDifPCIO2 = mean(PasrelPCIO2,'all');
GemDifICIO2 = mean(PasrelICIO2,'all');
```

```
% mean difference of IO 2
GemDifIO2 = mean([GemDifPOIO2 GemDifPCIO2 GemDifICIO2]);


GemDifPOIC2 = mean(PasrelPOIC2,'all');
GemDifIOIC2 = mean(PasrelIOIC2,'all');
GemDifPCIC2 = mean(PasrelPCIC2, 'all');
% mean difference of IC 2
GemDifIC2 = mean([GemDifPOIC2 GemDifIOIC2 GemDifPCIC2]);


GemDifIOPO2 = mean(PasrelIOPO2,'all');
GemDifPCPO2 = mean(PasrelPCPO2,'all');
GemDifICPO2 = mean(PasrelICPO2,'all');
% mean difference of PO 2
GemDifPO2 = mean([GemDifIOPO2 GemDifPCPO2 GemDifICPO2]);

%% find max accelerations of X and Z direction
calculating the resultant between the x and z directions
MXa_POPC = Xafilt(:,1:5);
MXa_POIO = Xafilt(:,6:10);
MXa_POIC = Xafilt(:,11:15);
MXa_IOPC = Xafilt(:,16:20);
MXa_IOPO = Xafilt(:,21:25);
MXa_IOIC = Xafilt(:,26:30);
MXa_PCPO = Xafilt(:,31:35);
MXa_PCIC = Xafilt(:,36:40);
MXa_PCIO = Xafilt(:,41:45);
MXa_ICIO = Xafilt(:,46:50);
MXa_ICPC = Xafilt(:,51:55);
MXa_ICPO = Xafilt(:,56:60);

MZa_POPC = Zafilt(:,1:5);
MZa_POIO = Zafilt(:,6:10);
MZa_POIC = Zafilt(:,11:15);
MZa_IOPC = Zafilt(:,16:20);
MZa_IOPO = Zafilt(:,21:25);
MZa_IOIC = Zafilt(:,26:30);
MZa_PCPO = Zafilt(:,31:35);
MZa_PCIC = Zafilt(:,36:40);
MZa_PCIO = Zafilt(:,41:45);
MZa_ICIO = Zafilt(:,46:50);
MZa_ICPC = Zafilt(:,51:55);
MZa_ICPO = Zafilt(:,56:60);

%calculating the resultant between the x and z directions
MFa_POPC = mean(sqrt((MXa_POPC).^2+(MZa_POPC).^2), 'all');
MFa_POIO = mean(sqrt((MXa_POIO).^2+(MZa_POIO).^2), 'all');
MFa_POIC = mean(sqrt((MXa_POIC).^2+(MZa_POIC).^2), 'all');
MFa_IOPC = mean(sqrt((MXa_IOPC).^2+(MZa_IOPC).^2), 'all');
MFa_IOPO = mean(sqrt((MXa_IOPO).^2+(MZa_IOPO).^2), 'all');
MFa_IOIC = mean(sqrt((MXa_IOIC).^2+(MZa_IOIC).^2), 'all');
MFa_PCPO = mean(sqrt((MXa_PCPO).^2+(MZa_PCPO).^2), 'all');
MFa_PCIC = mean(sqrt((MXa_PCIC).^2+(MZa_PCIC).^2), 'all');
MFa_PCIO = mean(sqrt((MXa_PCIO).^2+(MZa_PCIO).^2), 'all');
MFa_ICIO = mean(sqrt((MXa_ICIO).^2+(MZa_ICIO).^2), 'all');
MFa_ICPC = mean(sqrt((MXa_ICPC).^2+(MZa_ICPC).^2), 'all');
MFa_ICPO = mean(sqrt((MXa_ICPO).^2+(MZa_ICPO).^2), 'all');


%% Using acceleration as a scaling factor
```

```
% Thus, divide the relative pressure measurement by the resultant vector of the accelerations
PsbF_POPC1 = PasrelPOPC1/MFa_POPC;
PsbF_POPC2 = PasrelPOPC2/MFa_POPC;
PsbF_POIO1 = PasrelPOIO1/MFa_POIO;
PsbF_POIO2 = PasrelPOIO2/MFa_POIO;
PsbF_POIC1 = PasrelPOIC1/MFa_POIC;
PsbF_POIC2 = PasrelPOIC2/MFa_POIC;
PsbF_IOPC1 = PasrelIOPC1/MFa_IOPC;
PsbF_IOPC2 = PasrelIOPC2/MFa_IOPC;
PsbF_IOPO1 = PasrelIOPO1/MFa_IOPO;
PsbF_IOPO2 = PasrelIOPO2/MFa_IOPO;
PsbF_IOIC1 = PasrelIOIC1/MFa_IOIC;
PsbF_IOIC2 = PasrelIOIC2/MFa_IOIC;
PsbF_PCPO1 = PasrelPCPO1/MFa_PCPO;
PsbF_PCPO2 = PasrelPCPO2/MFa_PCPO;
PsbF_PCIC1 = PasrelPCIC1/MFa_PCIC;
PsbF_PCIC2 = PasrelPCIC2/MFa_PCIC;
PsbF_PCIO1 = PasrelPCIO1/MFa_PCIO;
PsbF_PCIO2 = PasrelPCIO2/MFa_PCIO;
PsbF_ICIO1 = PasrelICIO1/MFa_ICIO;
PsbF_ICIO2 = PasrelICIO2/MFa_ICIO;
PsbF_ICPC1 = PasrelICPC1/MFa_ICPC;
PsbF_ICPC2 = PasrelICPC2/MFa_ICPC;
PsbF_ICPO1 = PasrelICPO1/MFa_ICPO;
PsbF_ICPO2 = PasrelICPO2/MFa_ICPO;


% Putting all values in a table per orbit, varying by sensor
PsbF_PO1 = mean([mean(PsbF_POPC1, "all")
             mean(PsbF_POIO1, "all")
             mean(PsbF_POIC1, "all")]);

PsbF_PO2 = mean([mean(PsbF_POPC2, "all")
             mean(PsbF_POIO2, "all")
             mean(PsbF_POIC2, "all")]);

PsbF_IO1 = mean([mean(PsbF_IOPC1, "all")
             mean(PsbF_IOPO1, "all")
             mean(PsbF_IOIC1, "all")]);

PsbF_IO2 = mean([mean(PsbF_IOPC2, "all")
             mean(PsbF_IOPO2, "all")
             mean(PsbF_IOIC2, "all")]);


PsbF_PC1 = mean([mean(PsbF_PCPO1, "all")
             mean(PsbF_PCIC1, "all")
             mean(PsbF_PCIO1, "all")]);

PsbF_PC2 = mean([mean(PsbF_PCPO2, "all")
             mean(PsbF_PCIC2, "all")
             mean(PsbF_PCIO2, "all")]);

PsbF_IC1 = mean([mean(PsbF_ICIO1, "all")
             mean(PsbF_ICPC1, "all")
             mean(PsbF_ICPO1, "all")]);

PsbF_IC2 =mean([mean(PsbF_ICIO2, "all")
            mean(PsbF_ICPC2, "all")
            mean(PsbF_ICPO2, "all")])
```

Appendix I

Statistics

A Friedman's test with a Wilcoxon signed-rank Post hoc was conducted to test whether differences in eye pressure during violent shaking were present between the four orbits. Additionally, the difference between the two sensors was also examined

The following assumptions must be met:

Assumptions for taking the Friedman's test:

- One group that is measured on three or more separate occasions.
- Samples do NOT need to be normally distributed.
- The dependent variable is a continuous variable.

Assumptions for Wilcoxon signed-rank test:

- The dependent variable is a continuous variable.
- The independent variable should consist of two categorical variables; each combination of the shaking movements was performed separately and separately for each sensor.

Testing the assumptions

Normal distribution

According to the Shapiro-Wilk test (Table 7), all shaking variables were not normally distributed in both sensors ($p<0.05$). This can also be found in the histograms in Figure 27 for sensor 1 and Figure 28 for sensor 2Figure 28.

Table 7: Tests of Normality.

Tests of Normality

	Kolmogorov-Smirnov[a]			Shapiro-Wilk		
	Statistic	df	Sig.	Statistic	df	Sig.
PO1	,106	52	,200*	,937	52	,009
IO1	,122	52	,051	,927	52	,003
PC1	,120	52	,061	,878	52	<,001
IC1	,368	52	<,001	,747	52	<,001
PO2	,348	52	<,001	,761	52	<,001
IO2	,153	52	,004	,924	52	,003
PC2	,097	52	,200*	,960	52	,081
IC2	,171	52	<,001	,926	52	,003

*. This is a lower bound of the true significance.

a. Lilliefors Significance Correction

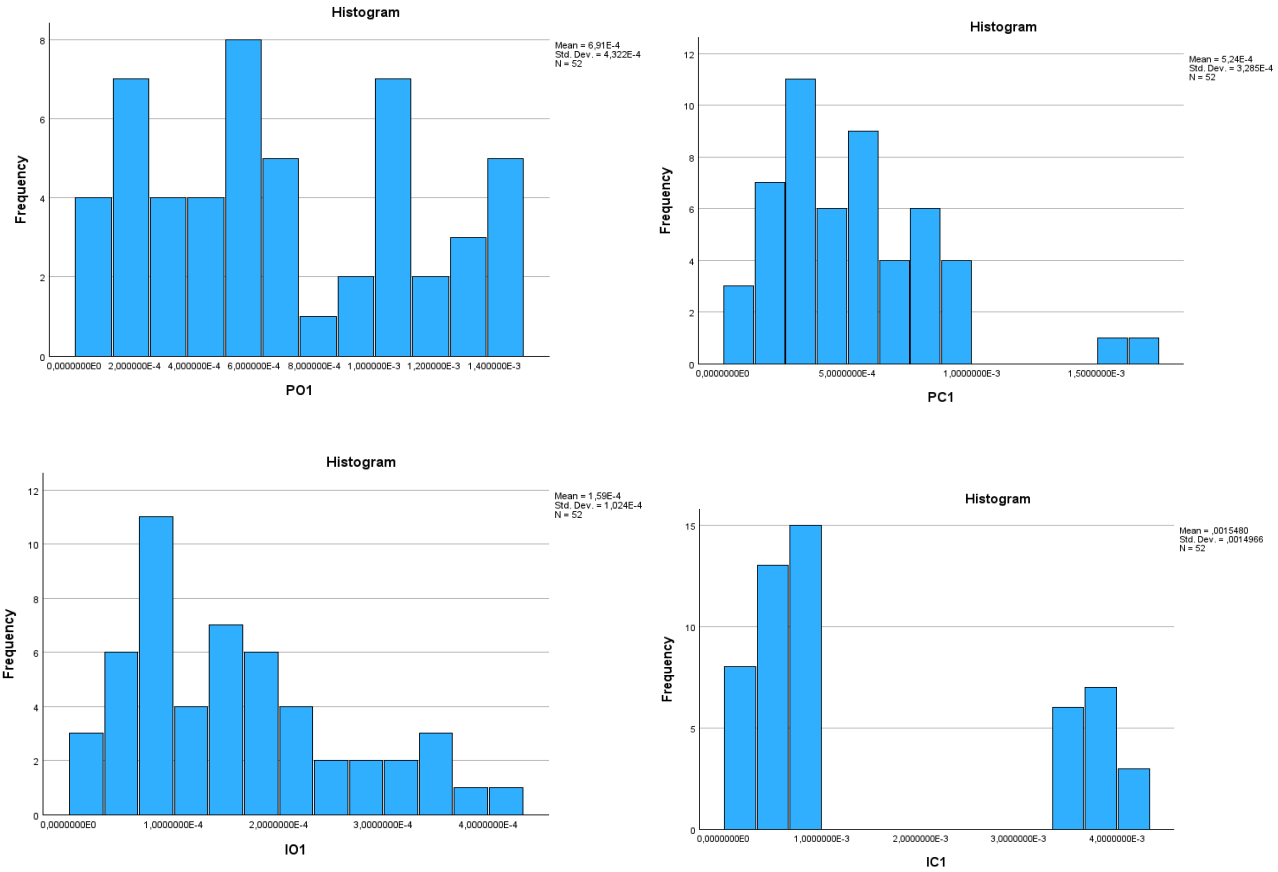

Figure 27: The Stem-and-Leaf Plot of all orbits for sensor 1.

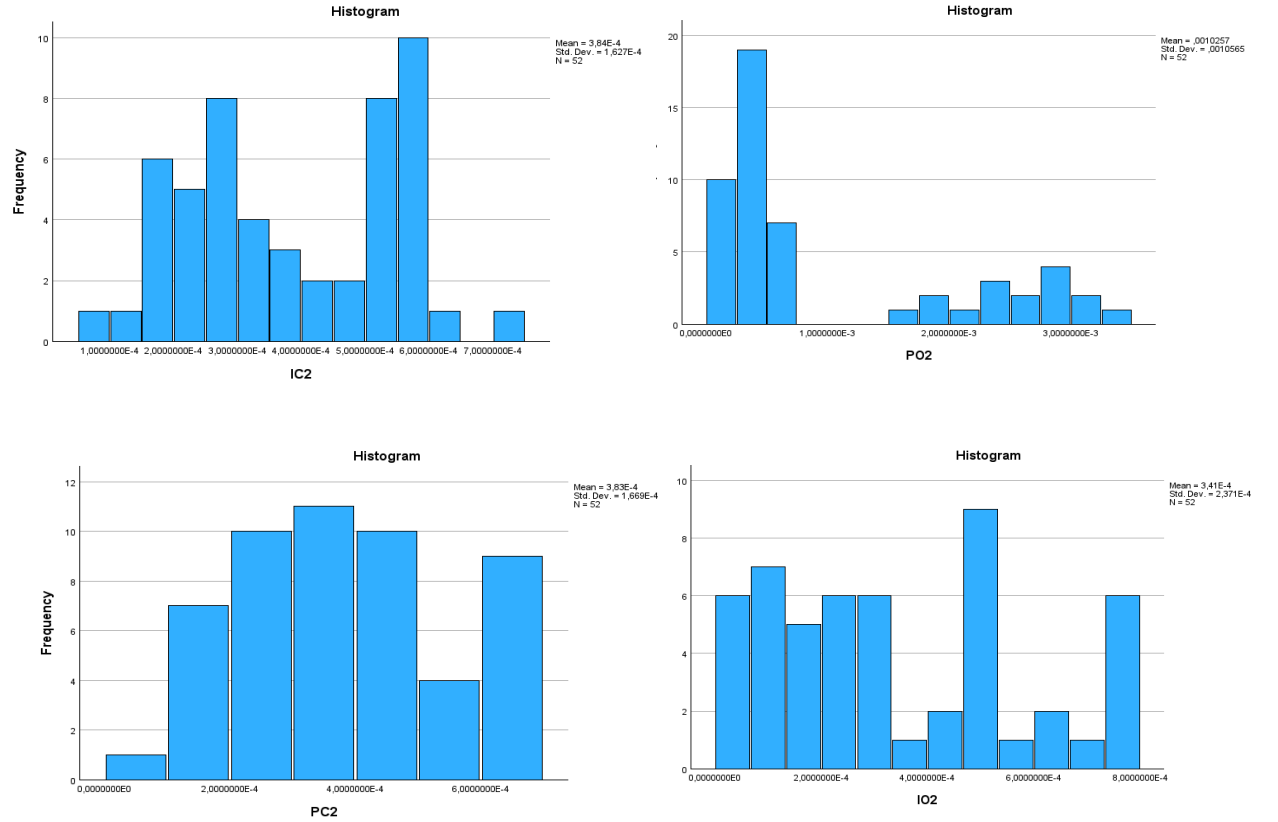

Figure 28: The Stem-and-Leaf Plot of all orbits for sensor 1.

Friedman test results

See Table 8 for the descriptives of the data of the current study. The Friedman's test results showed that there was a statistically significant difference between Ø.O, Ø.C, 35.O, 35.C in both sensors, $\chi 2(52) = 117.801$, $p < .001$ (Table 9 and Table 10). The Post hoc analysis with Wilcoxon signed-rank test results showed that er was a significant difference between the orbit combinations Ø.O - Ø.C ($p < 0.001$), Ø.O - 35.C ($p < 0.001$), Ø.O - 35.O ($p < 0.001$), Ø.C - 35.C ($p = 0.002$), Ø.C - 35.O ($p < 0.001$) for sensor 1 and between the orbit combinations Ø.O - Ø.C ($p = 0.002$), Ø.O - 35.O ($p < 0.001$), Ø.C - 35.O ($p < 0.001$), 35.O - 35.C ($p < 0.001$) for sensor 2 (Table 11 and Table 12).

Table 8: Descriptive statistics

	N	Mean	Std. Deviation	Minimum	Maximum	Percentiles 25th	50th (Median)	75th
PO1	52	,000691037	,0004322161	,0000443	,0014516	,000279151	,000604312	,001073440
IO1	52	,000158990	,0001024139	,0000119	,0004104	,000076000	,000138241	,000222958
PC1	52	,000523554	,0003285113	,0000832	,0016892	,000292491	,000432529	,000711014
IC1	52	,001548024	,0014966426	,0000149	,0043267	,000605901	,000814860	,003577904
PO2	52	,001025721	,0010565413	,0000145	,0032584	,000346472	,000476854	,002124465
IO2	52	,000341043	,0002370772	,0000124	,0007809	,000134903	,000281159	,000502285
PC2	52	,000383148	,0001669393	,0000154	,0006682	,000236978	,000391135	,000500467
IC2	52	,000383607	,0001627438	,0000861	,0007012	,000236301	,000368761	,000544125

Table 9: Friedman test; Ranks

	Mean Rank
PO1	5,25
IO1	1,75
PC1	4,87
IC1	6,56
PO2	5,15
IO2	3,90
PC2	3,94
IC2	4,58

Table 10: Friedman test; Test statistics

N	52
Chi-Square	117,801
df	7
Asymp. Sig.	<,001

a. Friedman Test

Table 11: Wilcoxon Signed Ranks test.

		N	Mean Rank	Sum of Ranks
IO1 - PO1	Negative Ranks	56[a]	32,18	1802,00
	Positive Ranks	4[b]	7,00	28,00
	Ties	0[c]		
	Total	60		
PC1 - PO1	Negative Ranks	33[d]	27,94	922,00
	Positive Ranks	27[e]	33,63	908,00
	Ties	0[f]		
	Total	60		
IC1 - PO1	Negative Ranks	10[g]	17,30	173,00
	Positive Ranks	42[h]	28,69	1205,00
	Ties	0[i]		
	Total	52		
PC1 - IO1	Negative Ranks	3[j]	3,00	9,00
	Positive Ranks	57[k]	31,95	1821,00
	Ties	0[l]		
	Total	60		
IC1 - IO1	Negative Ranks	7[m]	4,29	30,00
	Positive Ranks	45[n]	29,96	1348,00
	Ties	0[o]		
	Total	52		
IC1 - PC1	Negative Ranks	16[p]	21,75	348,00
	Positive Ranks	36[q]	28,61	1030,00
	Ties	0[r]		
	Total	52		
IO2 - PO2	Negative Ranks	35[s]	35,37	1238,00
	Positive Ranks	21[t]	17,05	358,00
	Ties	0[u]		
	Total	56		
PC2 - PO2	Negative Ranks	43[v]	29,30	1260,00
	Positive Ranks	13[w]	25,85	336,00
	Ties	0[x]		
	Total	56		
IC2 - PO2	Negative Ranks	33[y]	37,35	1232,50
	Positive Ranks	23[z]	15,80	363,50
	Ties	0[aa]		
	Total	56		
PC2 - IO2	Negative Ranks	19[ab]	33,21	631,00
	Positive Ranks	37[ac]	26,08	965,00
	Ties	0[ad]		

	Total	56		
IC2 - IO2	Negative Ranks	15[ae]	32,47	487,00
	Positive Ranks	45[af]	29,84	1343,00
	Ties	0[ag]		
	Total	60		
IC2 - PC2	Negative Ranks	22[ah]	31,27	688,00
	Positive Ranks	34[ai]	26,71	908,00
	Ties	0[aj]		
	Total	56		

a. IO1 < PO1

b. IO1 > PO1

c. IO1 = PO1

d. PC1 < PO1

e. PC1 > PO1

f. PC1 = PO1

g. IC1 < PO1

h. IC1 > PO1

i. IC1 = PO1

j. PC1 < IO1

k. PC1 > IO1

l. PC1 = IO1

m. IC1 < IO1

n. IC1 > IO1

o. IC1 = IO1

p. IC1 < PC1

q. IC1 > PC1

r. IC1 = PC1

s. IO2 < PO2

t. IO2 > PO2

u. IO2 = PO2

v. PC2 < PO2

w. PC2 > PO2

x. PC2 = PO2

y. IC2 < PO2

z. IC2 > PO2

aa. IC2 = PO2

ab. PC2 < IO2

ac. PC2 > IO2

ad. PC2 = IO2

ae. IC2 < IO2

af. IC2 > IO2

ag. IC2 = IO2

ah. IC2 < PC2

ai. IC2 > PC2

aj. IC2 = PC2

Table 12: Wilcoxon Signed Ranks Test; Statistics

	IO1 - PO1	PC1 - PO1	IC1 - PO1	PC1 - IO1	IC1 - IO1	IC1 - PC1	IO2 - PO2	PC2 - PO2	IC2 - PO2	PC2 - IO2	IC2 - IO2	IC2 - PC2
Z	-6,530[b]	-,052[b]	-4,699[c]	-6,670[c]	-6,001[c]	-3,105[c]	-3,589[b]	-3,769[b]	-3,544[b]	-1,362[c]	-3,151[c]	-,897[c]
Asymp. Sig. (2-tailed)	<,001	,959	<,001	<,001	<,001	,002	<,001	<,001	<,001	,173	,002	,370

a. Wilcoxon Signed Ranks Test

b. Based on positive ranks.

c. Based on negative ranks.

Appendix J

Technical drawings orbits

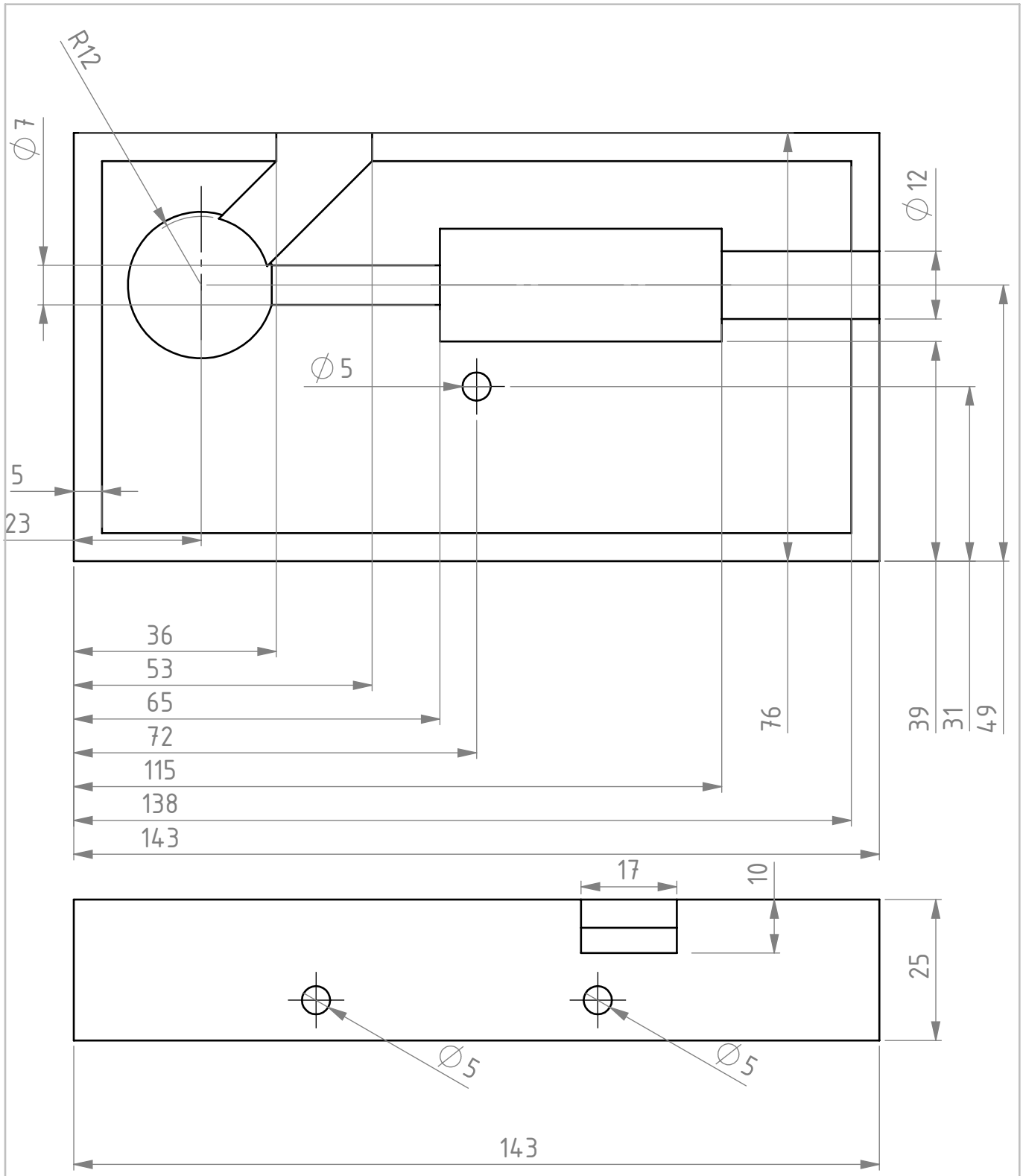

	units mm	scale 1:2	quantity <<nr>>	date 5-4-2024	remark <<remarks>>
material				mass gr	
author <<names & student numbers>>				group <<group>>	TU Delft Delft University of Technology
name Msc_Orbit_Infant_LowerPart_Closed_202				format A4	drawing no. <<drawing no.>>

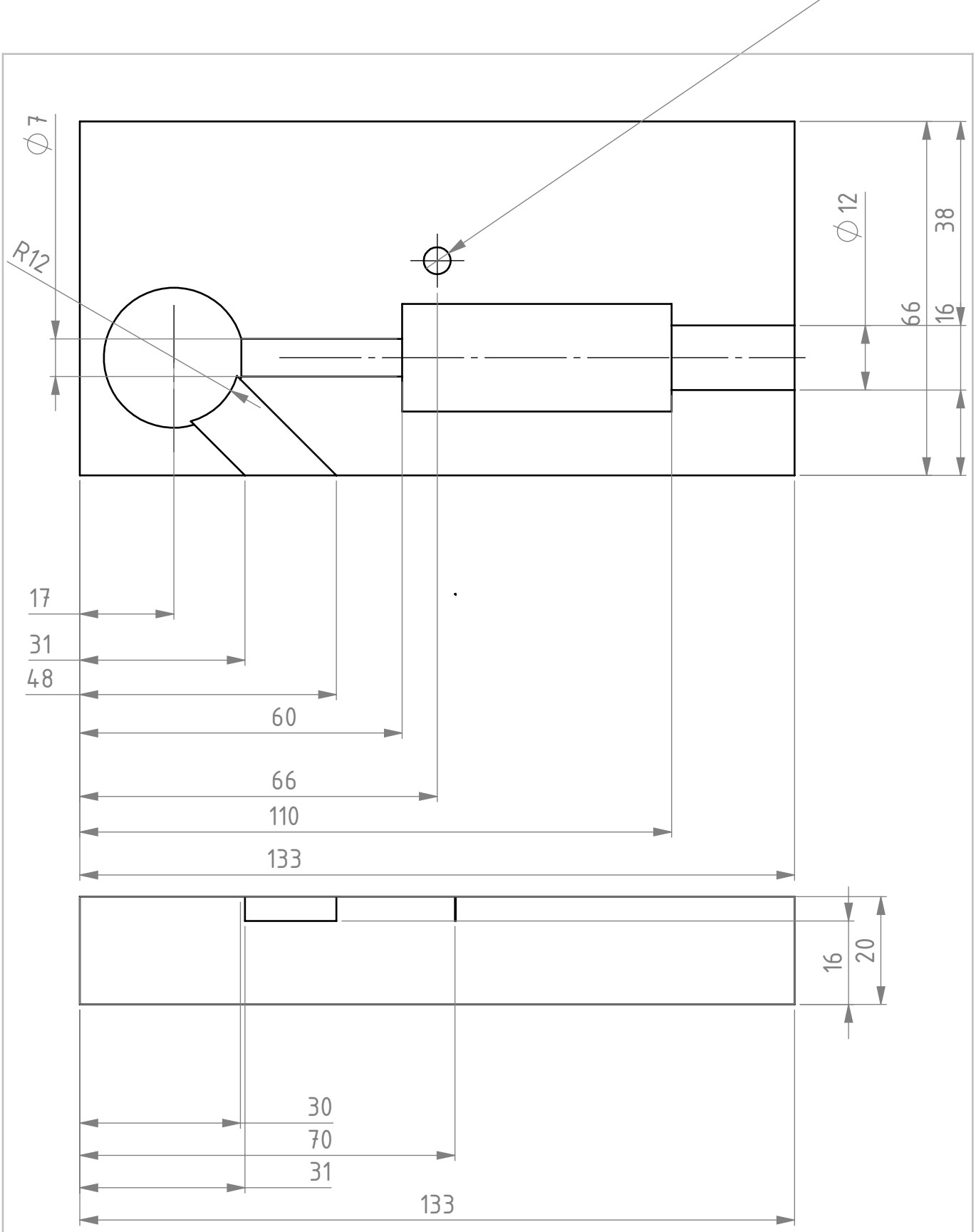

	units mm	scale 1:2	quantity -	date 5-4-2024	remark -
material				mass gr	
author Anneloes van den Berg				group -	TU Delft Delft University of Technology
name Msc_Orbit_Infant_UpperPart_Closed_202				format A4	drawing no. -

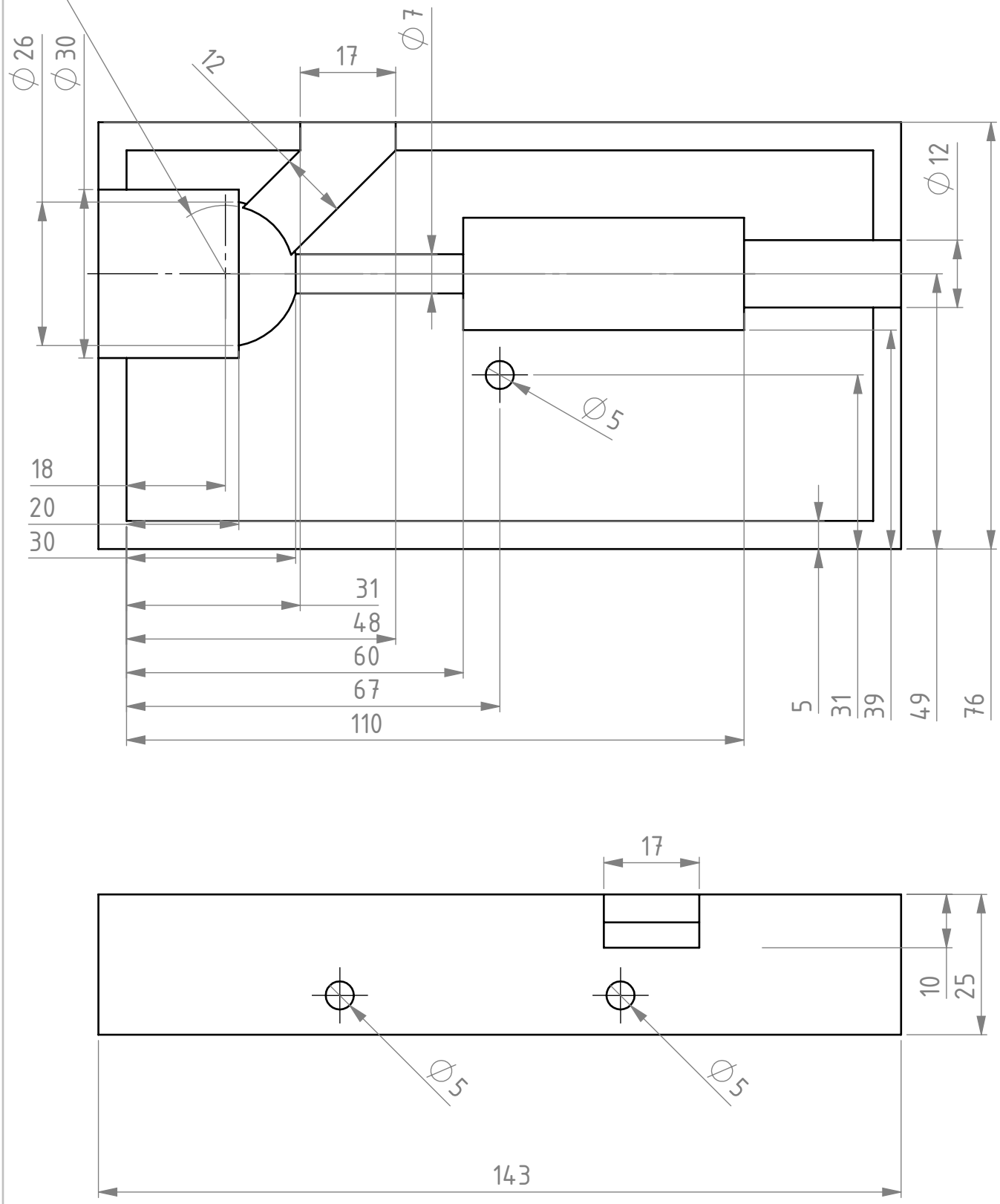

	units mm	scale 1:2	quantity -	date 5-4-2024	remark -
material				mass gr	
author Anneloes van den Berg				group -	TU Delft Delft University of Technology
name Msc_Orbit_Infant_LowerPart_Open_2024				format A4	drawing no. -

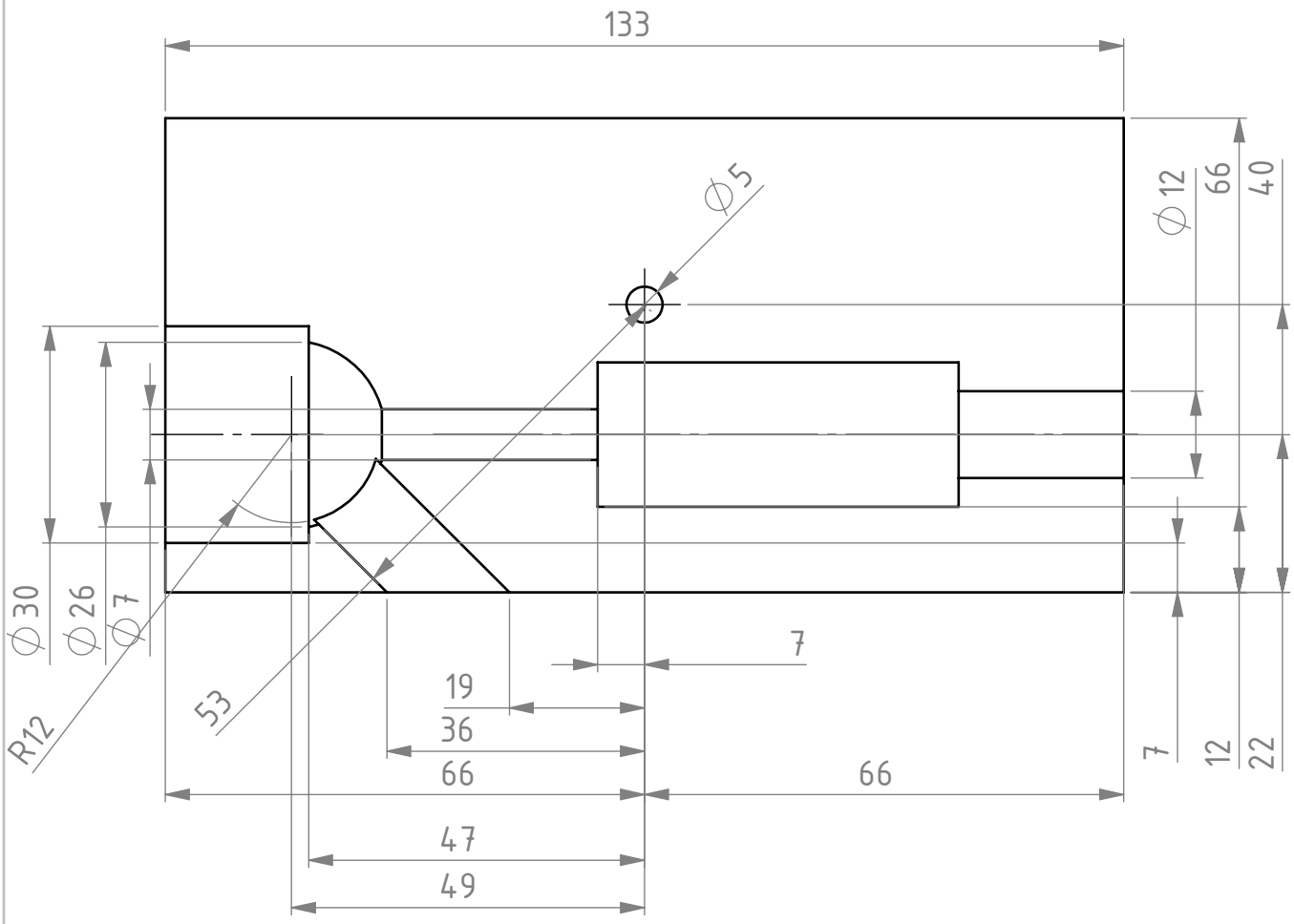

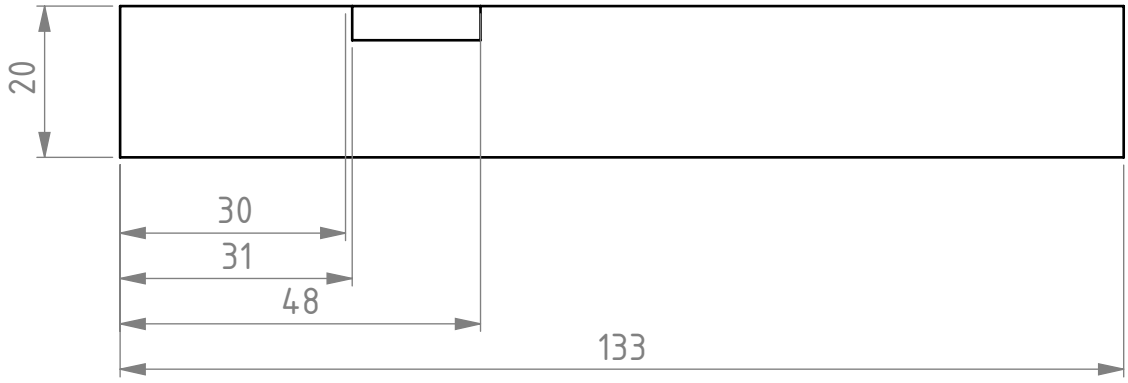

	units mm	scale 1:2	quantity <<nr>>	date 5-4-2024	remark <<remarks>>
material				mass gr	
author <<names & student numbers>>				group <<group>>	TU Delft Delft University of Technology
name Msc_Orbit_Infant_UpperPart_Open_2024				format A4	drawing no. <<drawing no.>>

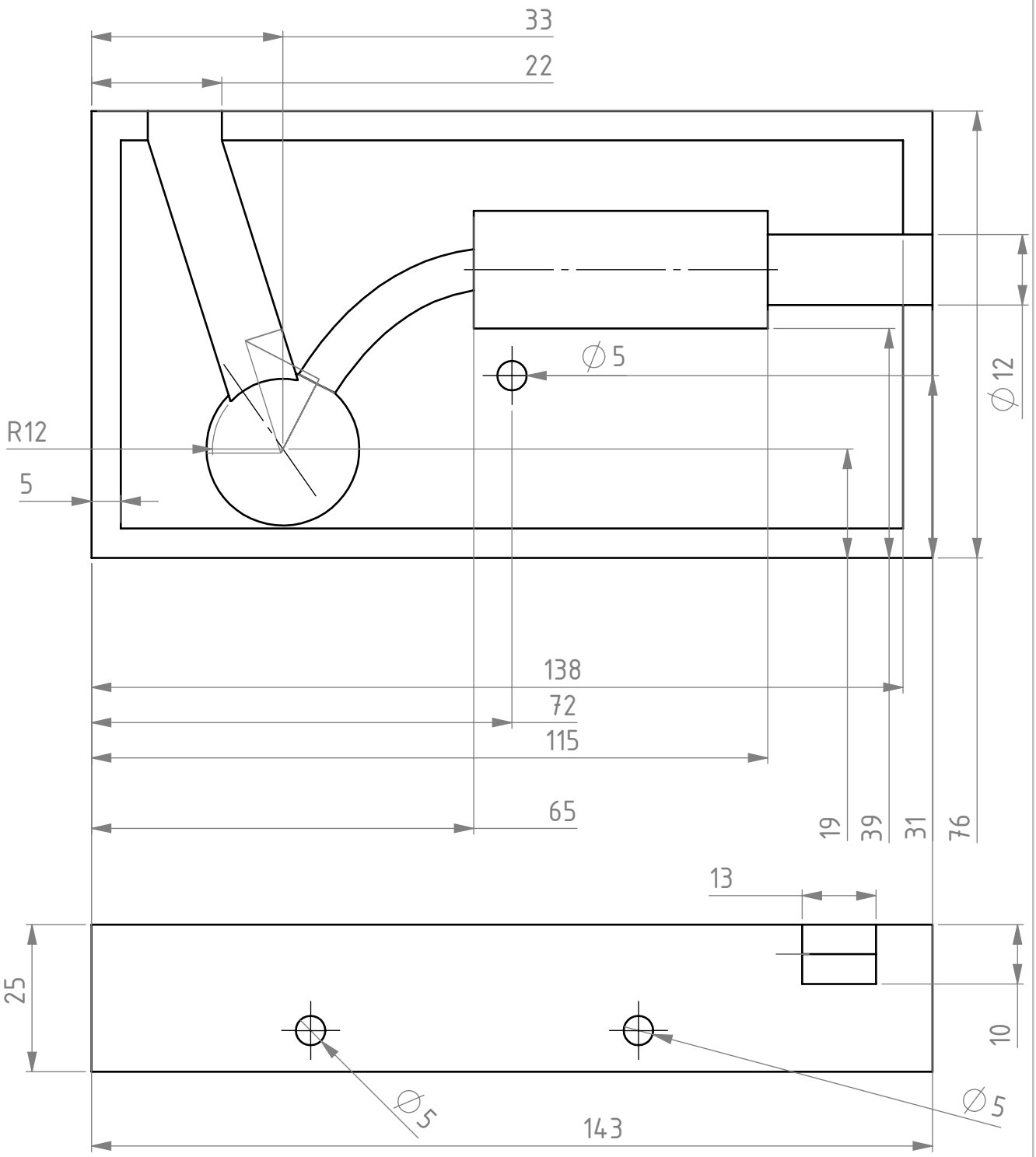

	units mm	scale 1:2	quantity -	date 5-4-2024	remark -
material				mass gr	
author Anneloes van den Berg				group -	TU Delft Delft University of Technology
name Msc_Orbit_Pig_LowerPart_Closed_20240				format A4	drawing no. -

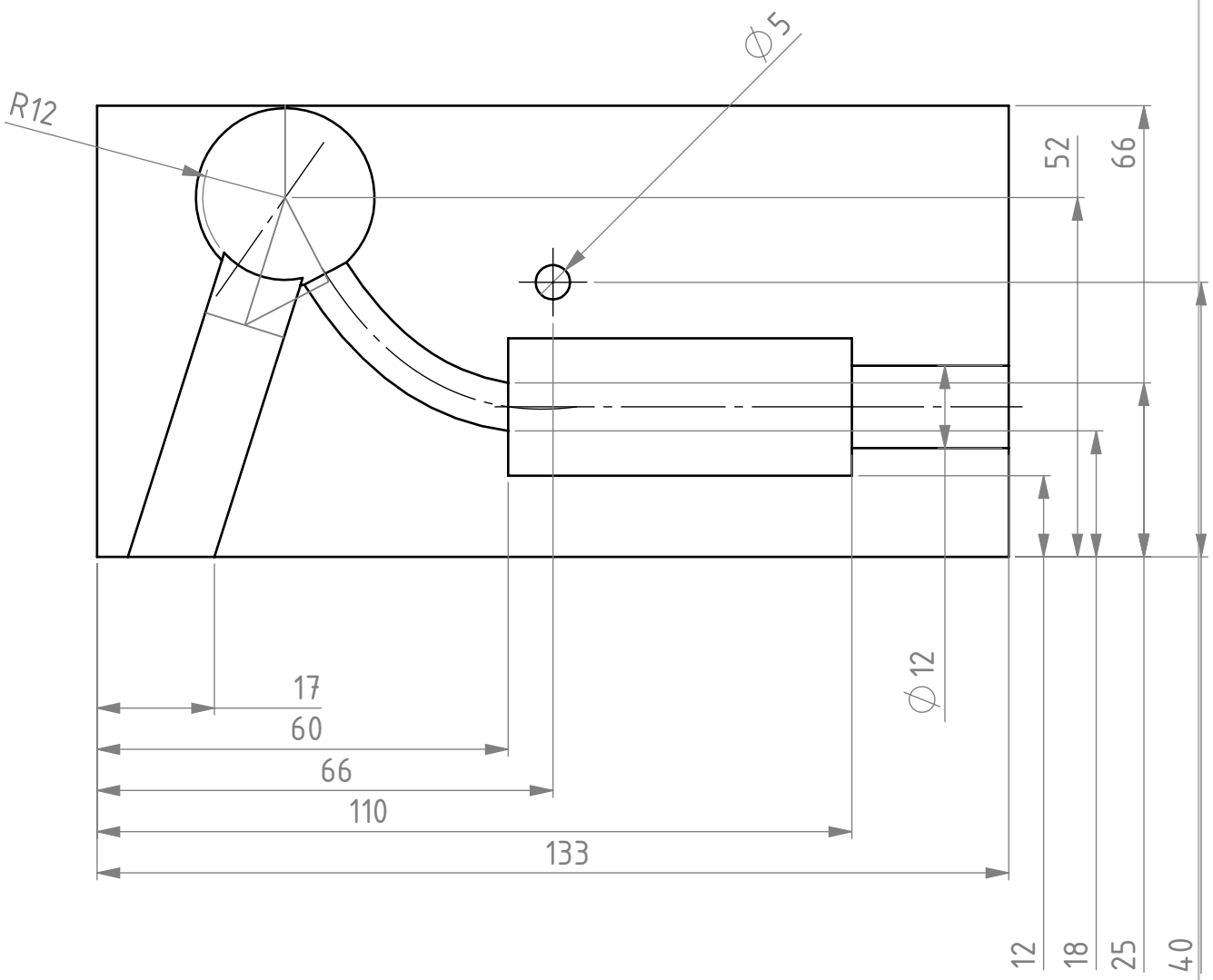

	units mm	scale 1:2	quantity -	date 5-4-2024	remark -
material				mass gr	
author Anneloes van den Berg				group -	TU Delft Delft University of Technology
name Msc_Orbit_Pig_UpperPart_Closed_2024				format A4	drawing no. -

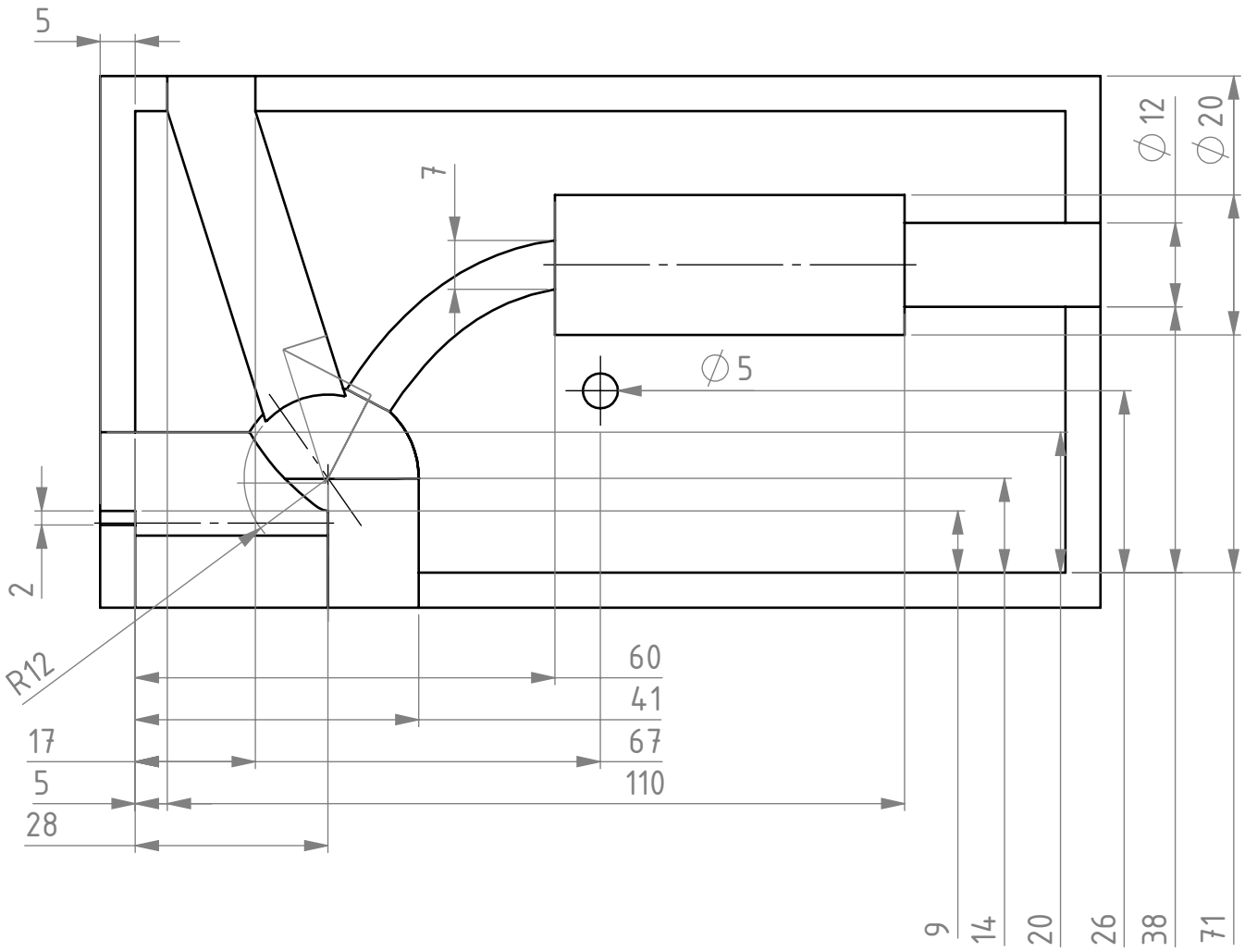

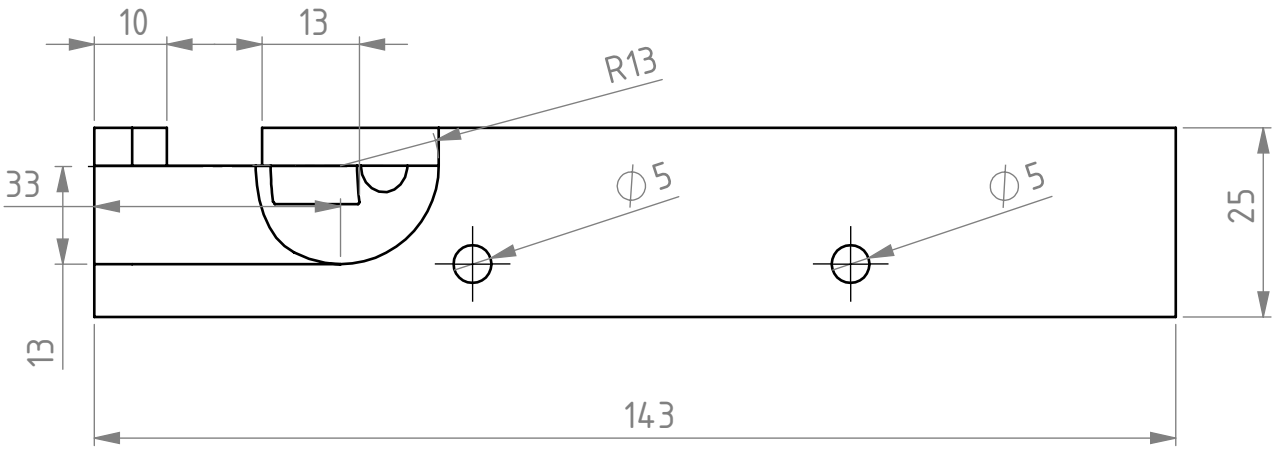

	units mm	scale 1:2	quantity -	date 5-4-2024	remark -
material				mass gr	
author Anneloes van den Berg				group -	TU Delft Delft University of Technology
name Msc_Orbit_Pig_LowerPart_Open_20240				format A4	drawing no. -

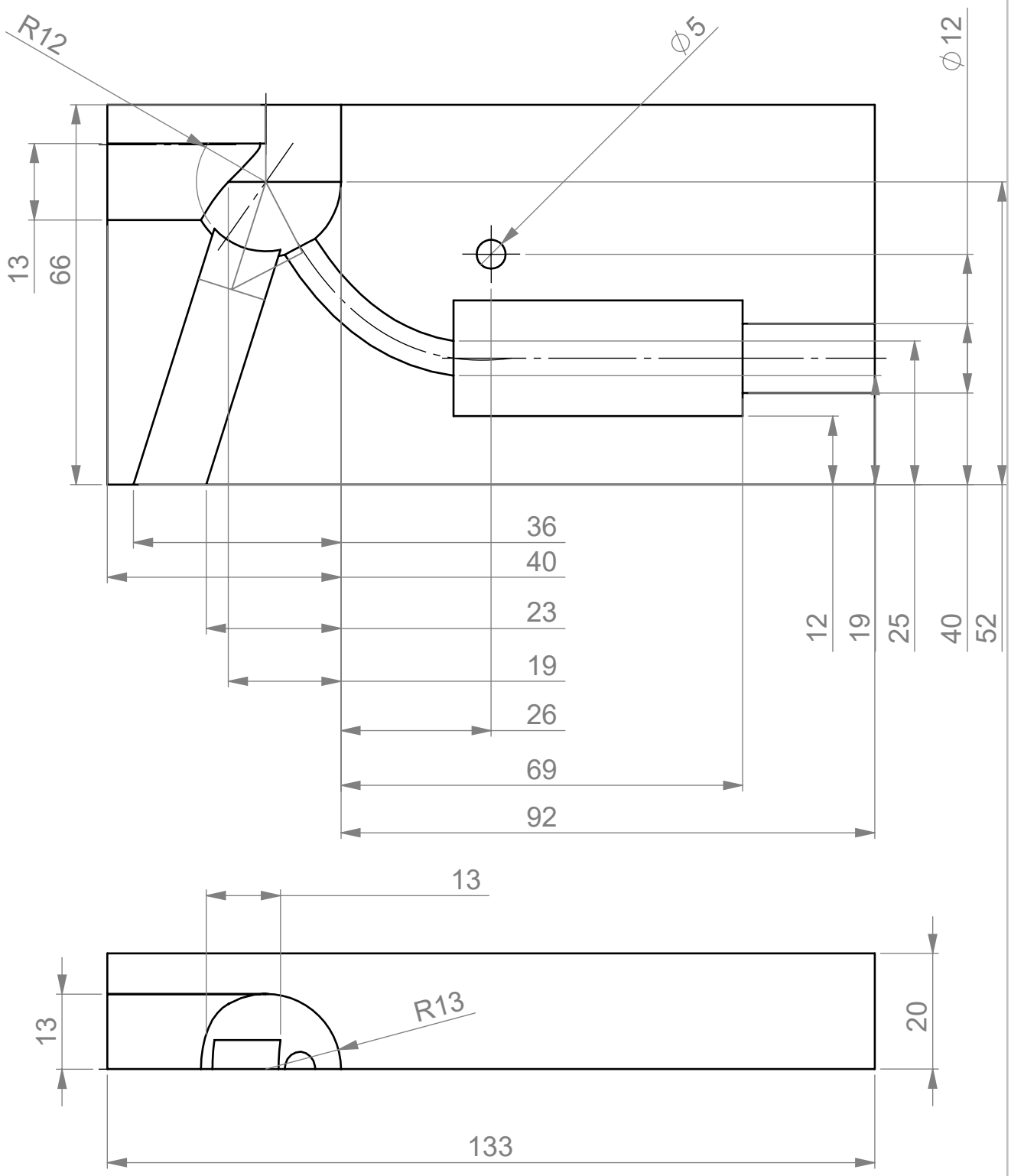

	units mm	scale 1:2	quantity -	date 11-8-2024	remark -
material				mass gr	
author Anneloes van den Berg				group -	TU Delft Delft University of Technology
name Msc_Orbit_Pig_UpperPart_Open_20240				format A4	drawing no. -

D:\Anneloes\BU-Anneloes-20240416-16u56\Solidworks\Msc_Oogkas_Eind\

Appendix K

Technical drawings mould of the eye model

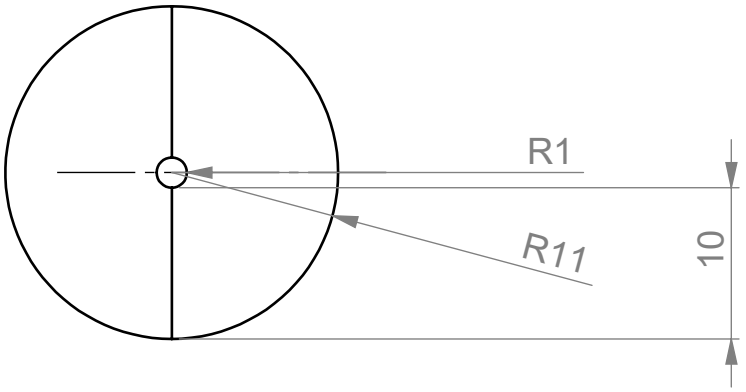

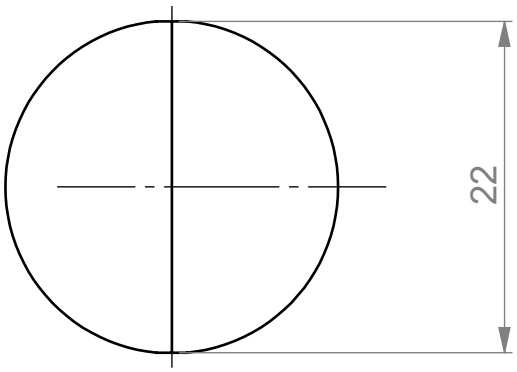

	units mm	scale 2:1	quantity -	date 7-8-2024	remark -
material				mass gr	
author Anneloes van den Berg				group -	TU Delft Delft University of Technology
name Mould-EyeBall-Ball-20230817				format A4	drawing no. -
D:\Anneloes\GraduationProject_AnneloesVanDenBerg_20240729\Solidworks\Mould-EyeBall\					

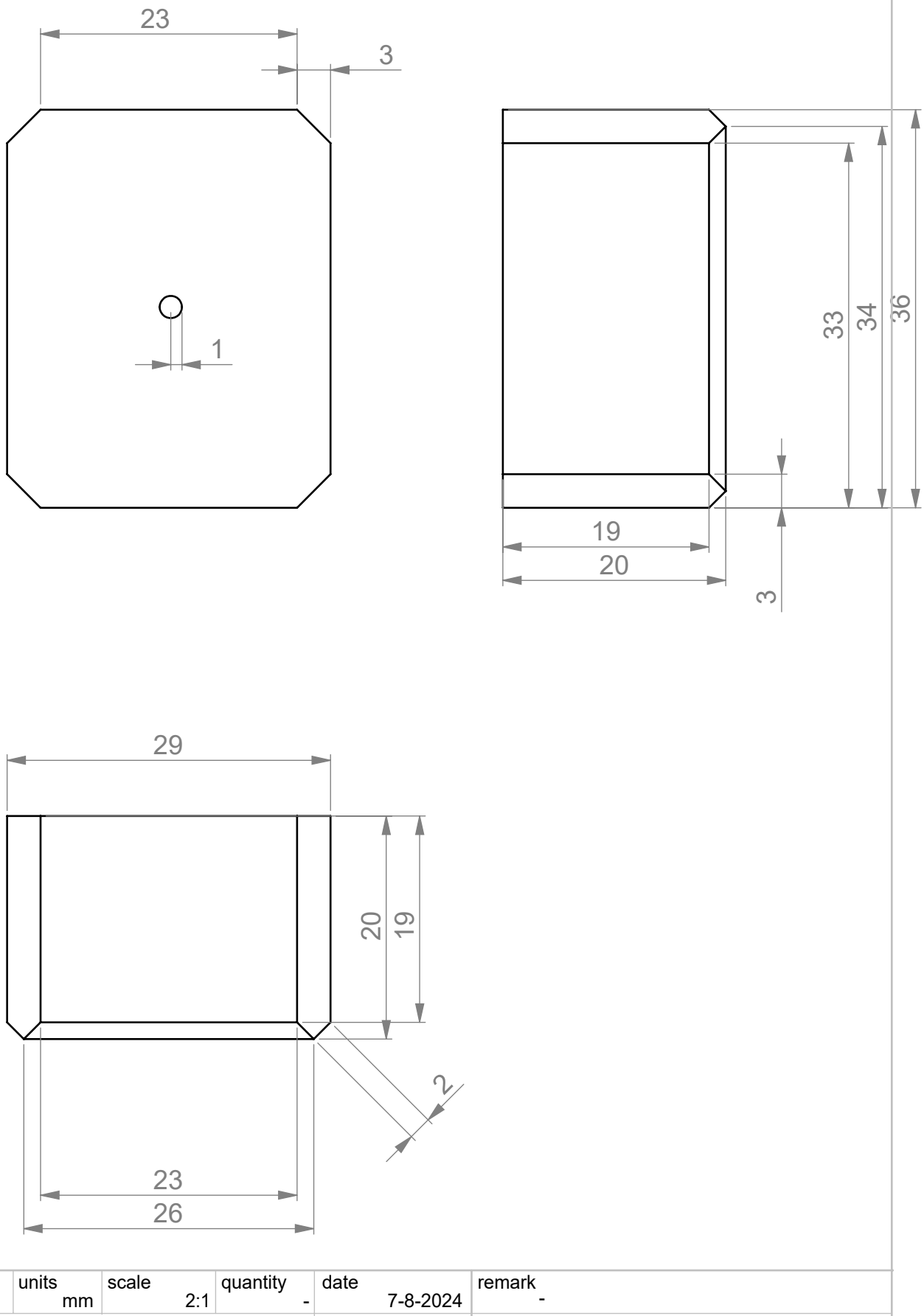

	units mm	scale 2:1	quantity -	date 7-8-2024	remark -
material				mass gr	
author Anneloes van dne Berg				group -	TU Delft Delft University of Technology
name Mould-EyeBall-Stabilize-20230817				format A4	drawing no -

D:\Anneloes\GraduationProject_AnneloesVanDenBerg_20240729\Solidworks\Mould-EyeBall\

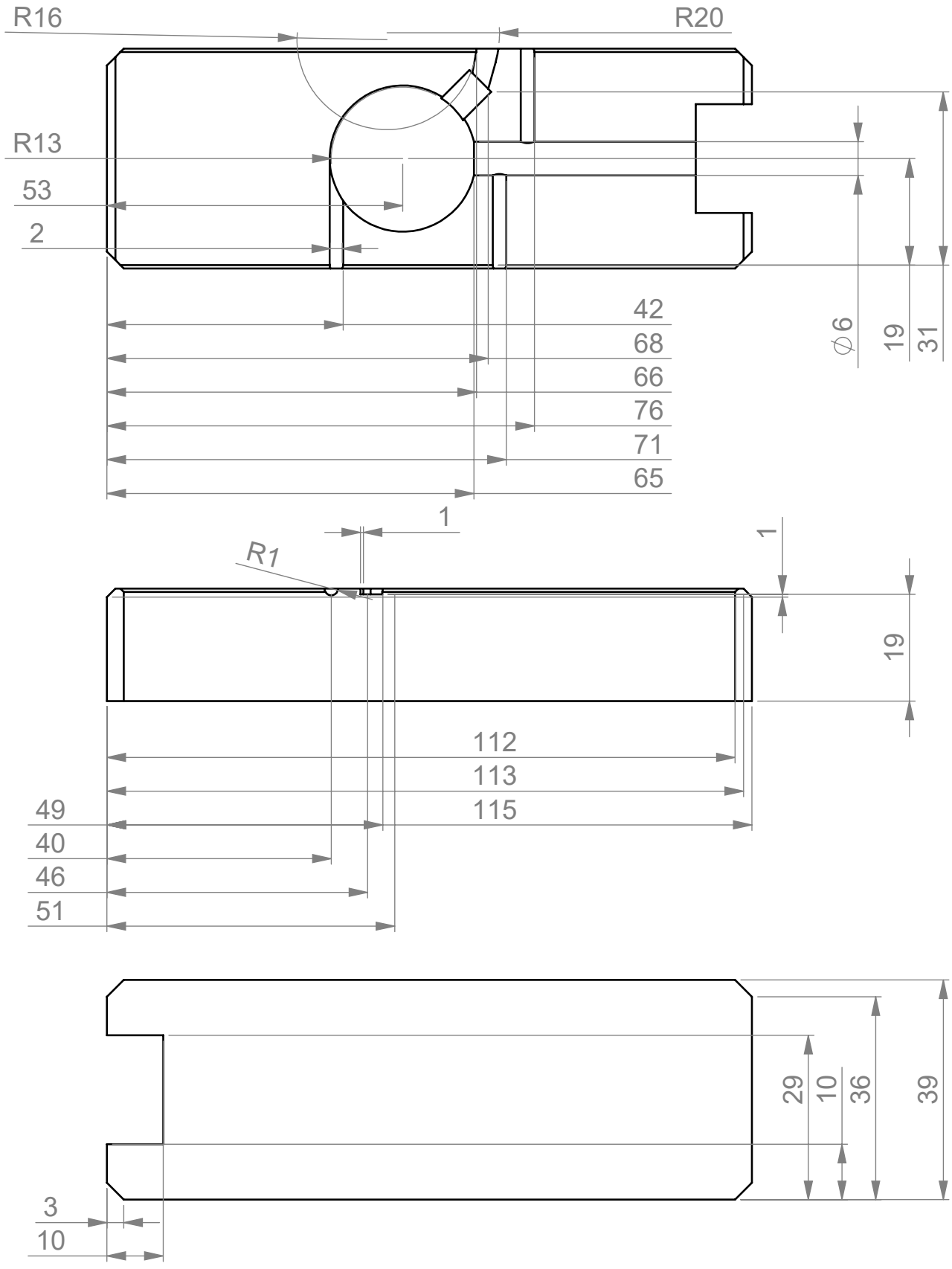

	units mm	scale 1:2	quantity -	date 7-8-2024	remark -
material				mass gr	
author Anneloes van den Berg				group -	TU Delft Delft University of Technology
name Mould-EyeBall-UpperPart-20230817				format A4	drawing no. -
D:\Anneloes\GraduationProject_AnneloesVanDenBerg_20240729\Solidworks\Mould-EyeBall\					

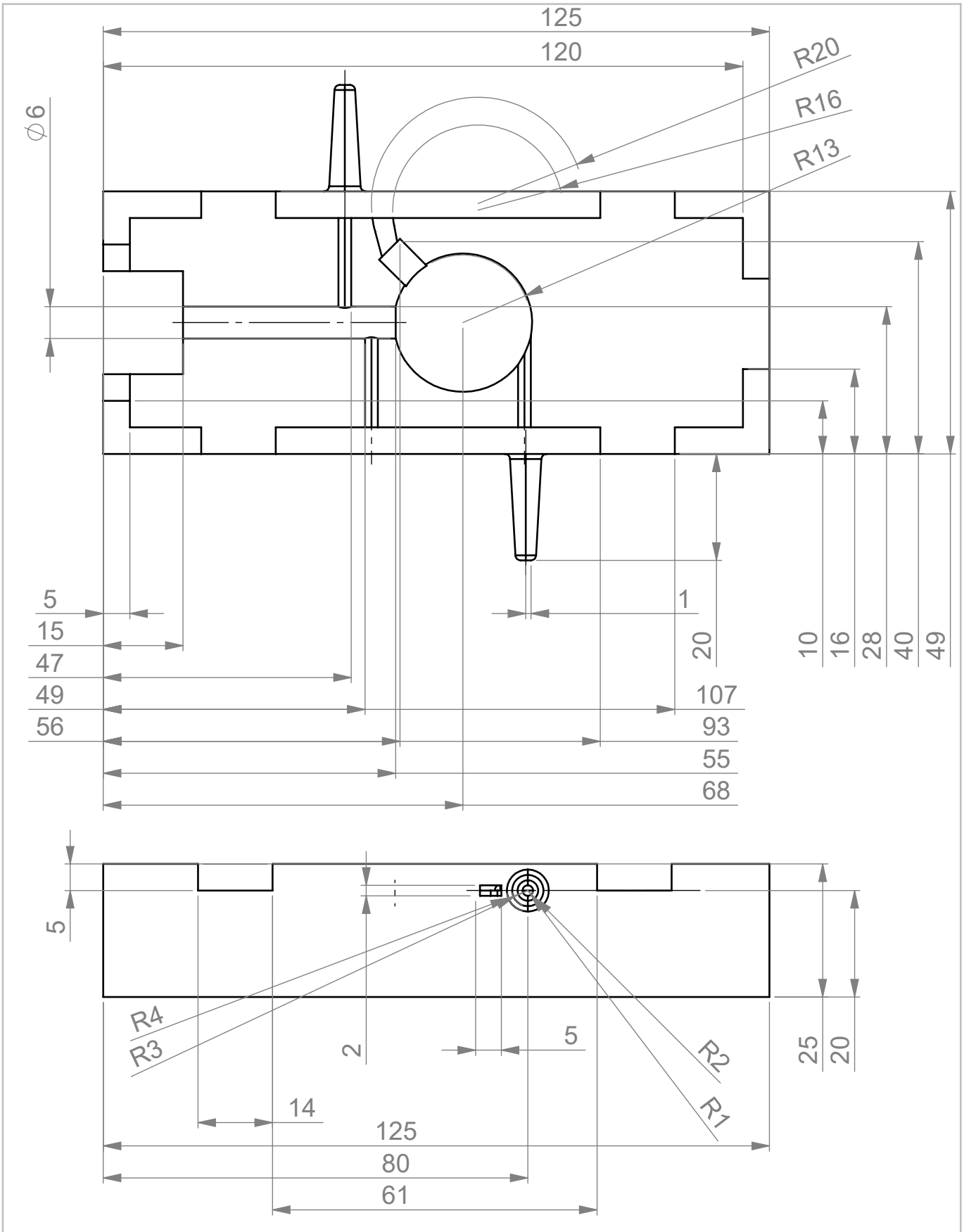

	units mm	scale 1:2	quantity -	date 7-8-2024	remark -
material				mass gr	
author Anneloes van den Berg				group -	TU Delft Delft University of Technology
name Mould-EyeBall-LowerPart-20230817				format A4	drawing no. -

D:\Anneloes\GraduationProject_AnneloesVanDenBerg_20240729\Solidworks\Mould-EyeBall\

Appendix L

Technical drawings Shake Simulator

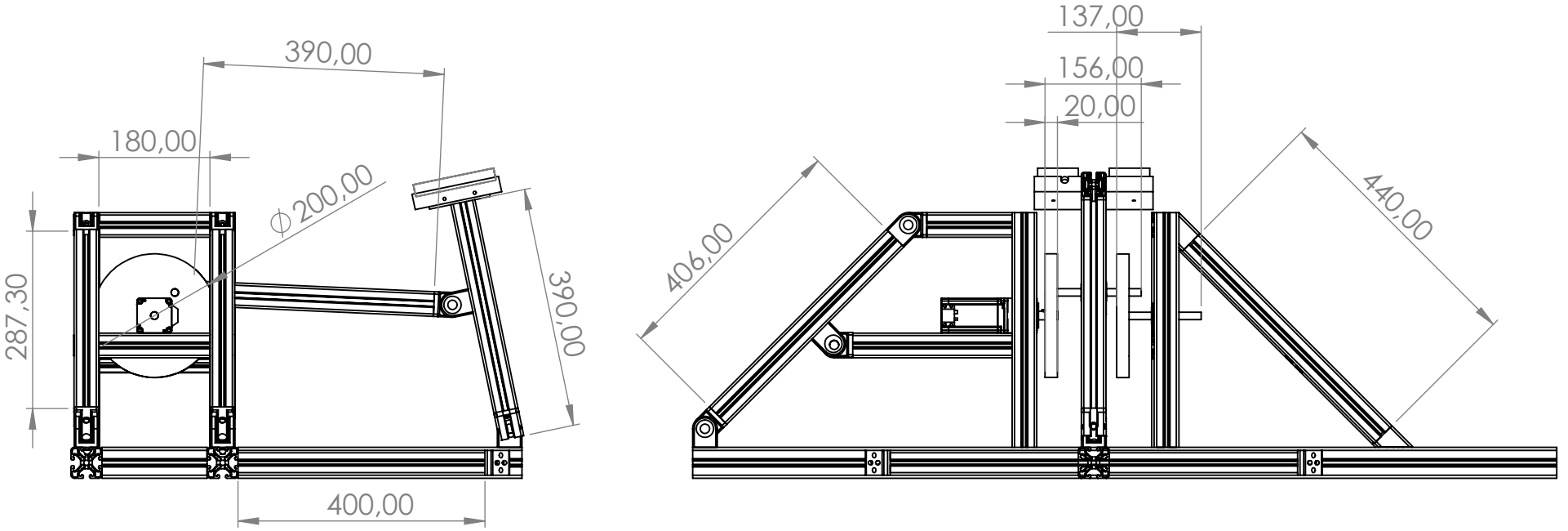

UNLESS OTHERWISE SPECIFIED: DIMENSIONS ARE IN MILLIMETERS SURFACE FINISH: TOLERANCES: LINEAR: ANGULAR:		FINISH:			DEBURR AND BREAK SHARP EDGES	DO NOT SCALE DRAWING	REVISION
	NAME	SIGNATURE	DATE			TITLE:	
DRAWN						PART--DESC	
CHK'D							
APPV'D							
MFG							
Q.A				MATERIAL:		DWG NO.	A4
						Experimental-SetUp-20240413	
				WEIGHT:		SCALE:1:20	SHEET 1 OF 1

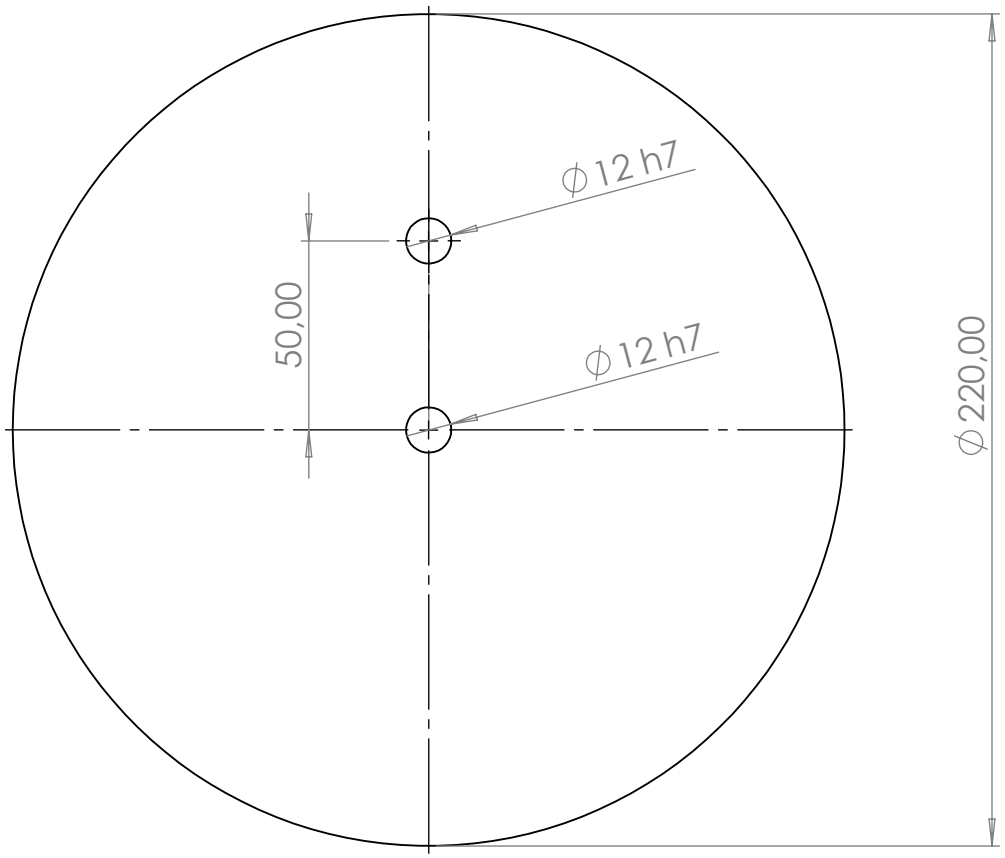

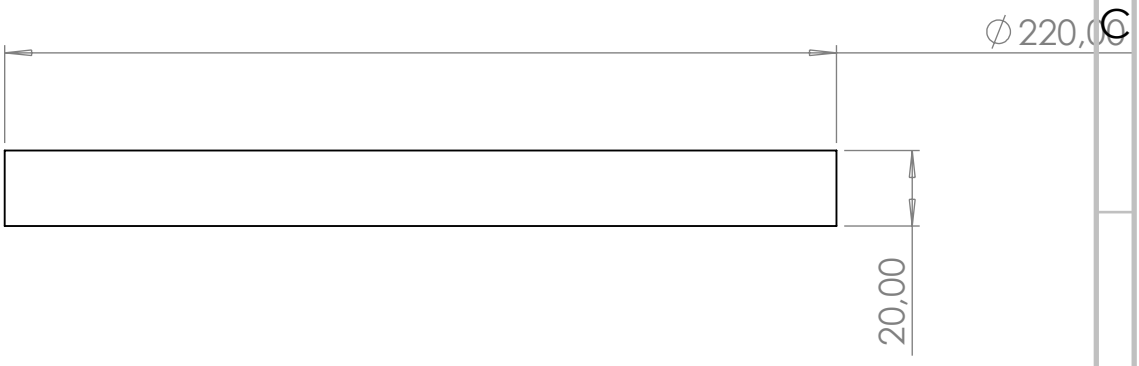

UNLESS OTHERWISE SPECIFIED: DIMENSIONS ARE IN MILLIMETERS SURFACE FINISH: TOLERANCES: LINEAR: ANGULAR:		FINISH:		DEBURR AND BREAK SHARP EDGES		DO NOT SCALE DRAWING	REVISION
	NAME	SIGNATURE	DATE			TITLE:	
DRAWN							
CHK'D							
APPV'D							
MFG							
Q.A				MATERIAL:		DWG NO.	A4
						Vliegwiel_Balans_20240314	
				WEIGHT:		SCALE:1:2	SHEET 1 OF 1

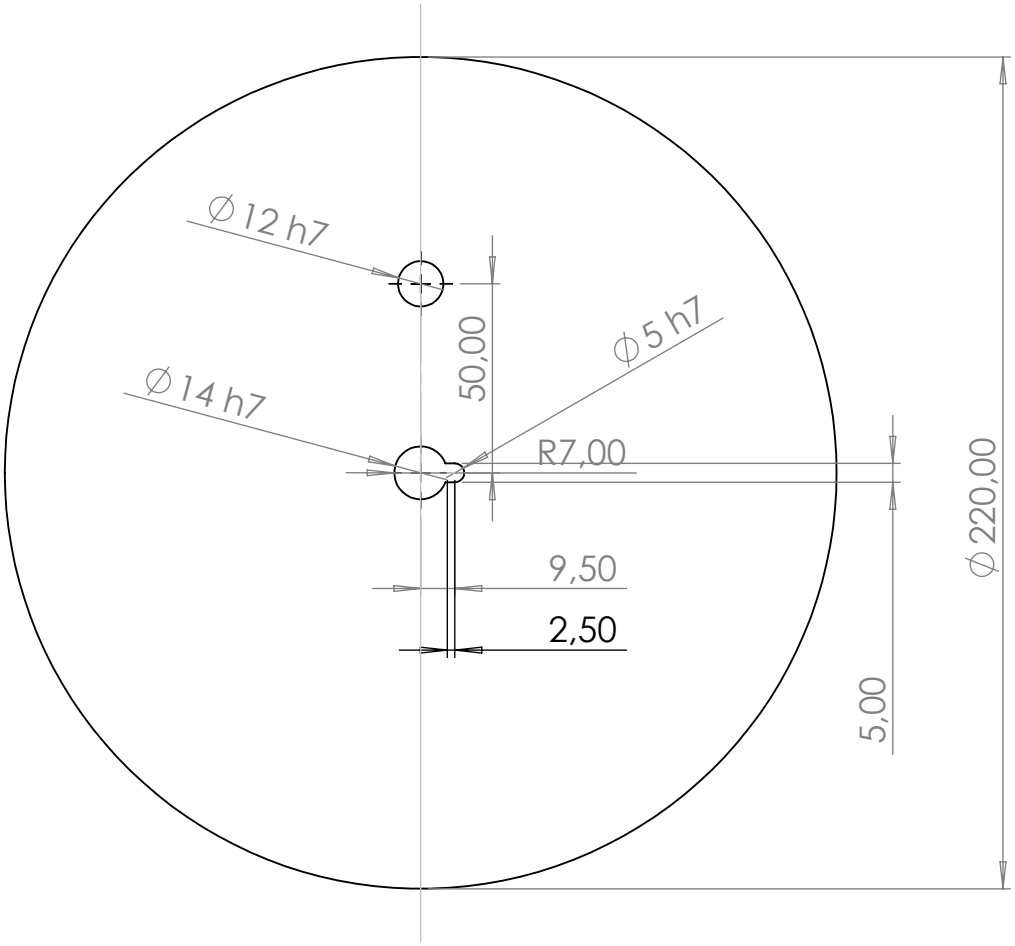

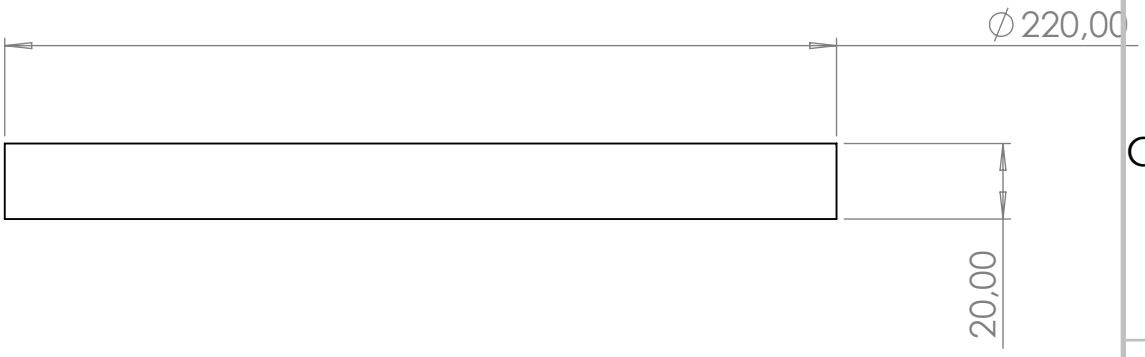

UNLESS OTHERWISE SPECIFIED: DIMENSIONS ARE IN MILLIMETERS SURFACE FINISH: TOLERANCES: LINEAR: ANGULAR:		FINISH:		DEBURR AND BREAK SHARP EDGES		DO NOT SCALE DRAWING	REVISION
	NAME	SIGNATURE	DATE			TITLE:	
DRAWN							
CHK'D							
APPV'D							
MFG							
Q.A				MATERIAL:		DWG NO.	A4
						Vliegwiel_Motor_20240312	
				WEIGHT:		SCALE:1:2	SHEET 1 OF 1